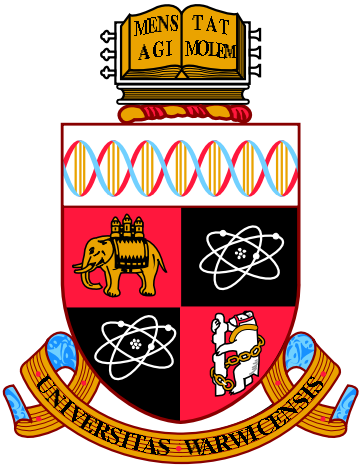

Search for heavy neutral MSSM Higgs bosons in the di-tau final state with the ATLAS detector

by

Adomas Jelinskas

Thesis

Submitted to the University of Warwick

for the degree of

Doctor of Philosophy

Department of Physics

January 2019

THE UNIVERSITY OF WARWICK

Contents

List of Tables

List of Figures

Acknowledgments

I would like to thank the ATLAS group at the University of Warwick for giving me the opportunity to do this research. In particular, I want to thank my supervisor, Professor William Murray, for his support and guidance. Many thanks to Professor Paul Harrison and Professor Sinead Farrington for making the work environment so welcoming. Thank you to my office friends, Dr. Tim Martin, Dr. Martin Spangenberg, Chris McNicol and Vangelis Vladimirov for making the workplace interesting.

I would also like to thank the HBSM subgroup of the ATLAS experiment for the given opportunity to explore such an interesting topic. Thanks to Dr. Lei Zhang for valuable advice and discussions during the years, which helped me a lot in reaching my goal. Thank you to the entire ATLAS collaboration for pursuing this difficult quest for knowledge.

I am very grateful to my parents whose support allowed me to accomplish this crazy goal. Thank you to my sister and grandmother for being with me. A special thanks goes to my friends Simona Lukševičiūtė, Eimantas Šimulis and Cedric Conboy for emotional support during the most difficult times. An exceptional thank you goes to my friend Giedrė Juknevičiūtė for teaching me happiness. Last but not least, I want to thank all my friends and family members for being there for me.

Declarations

This thesis is submitted to the University of Warwick in support of my application for the degree of Doctor of Philosophy. It has been composed by myself and has not been submitted in any previous application for any degree.

All figures and tables taken from various sources and used in this thesis have been properly referenced. Figures that use ATLAS data and are produced by myself are labeled "ATLAS Thesis only". Other figures are produced by myself.

As a member of the ATLAS collaboration I contributed to the experiment with my work on the tau lepton trigger software. Moreover, the work on the analysis software, which I used for obtaining the results presented in this thesis, is continuing to be developed and built upon by the members of the ATLAS HBSM subgroup.

The work I performed during the four years enrollment at the University of Warwick was included in two papers with $3.2\,\mathrm{fb}^{-1}$ [1] and $36.1\,\mathrm{fb}^{-1}$ [2] data sets.

Abstract

A search for heavy neutral Minimal Supersymmetric Standard Model Higgs bosons, $\mathcal{CP}$-even H and $\mathcal{CP}$-odd A, is presented. The analysis uses $36.1\,\text{fb}^{-1}$ data set collected in 2015 and 2016 with the ATLAS detector during Run 2 of the LHC at $\sqrt{s} = 13\,\text{TeV}$. Higgs bosons were searched for in the decay channel to a pair of tau leptons where one tau decays leptonically and another tau decays hadronically. No significant excess of events above the expected background from Standard Model processes was observed. Upper limits on cross section times branching ratio is set at a 95% Confidence Level for two production modes of the Higgs bosons: gluon-gluon fusion and b-associated production. The results are also interpreted in $m_{\text{h}}^{\text{mod}-}$ and hMSSM benchmark scenarios of the MSSM. The analysis takes advantage of Higgs boson to down-type fermion coupling enhancement at high values of the $\tan\beta$ parameter of the MSSM and therefore is capable of excluding high $\tan\beta$ region in the $M_A - \tan\beta$ parameter space.

Chapter 1

Theoretical Description of Particle Physics

"in truth, only atoms and the void"
- Sean Carroll

Modern particle physics is a rather young subject which had its best current theoretical description completed in the 1960s within the Standard Model (SM) of particle physics. The SM describes the constituents of matter and three of the four forces of nature: electromagnetic, weak and strong forces. The electromagnetic and weak interactions are unified in a single framework, the Glashow-Weinberg-Salam (GWS) [3, 4, 5] theory, also called the electroweak theory. The electromagnetic part of the GWS theory was first developed in the theory of quantum electrodynamics (QED), which also served as a prototype for the weak and strong interactions. An important part of the GWS theory is the Brout-Englert-Higgs (BEH) mechanism [6, 7], which was incorporated in order to explain the origin of mass of the weak force carriers, the $W^{\pm}$ and Z bosons, and, moreover, led to the explanation of the origin of mass of quarks and charged leptons. The mass origin of neutrinos and the Higgs boson itself are not explained in the SM. The strong force, which acts on hadrons and their constituents, is explained in the theory of quantum chromodynamics (QCD). The force carriers in QCD, the gluons, act on quarks and thus generate the strong interaction. On the other hand, the strong interaction between composite hadrons is believed to be a residual force that has its origin in the fundamental interactions of the constituent quarks and gluons described by QCD. One of the main successes of QCD was the explanation why quarks are not

observed in isolation but are always confined within hadrons.

The Standard Model of particle physics is a remarkably successful theory that has been shown to describe nature accurately at energy scales of up to around 1 TeV. One of its predictions, the anomalous magnetic moment of the electron, has been calculated to the fifth order in perturbation theory [8], which used 12,672 Feynman diagrams of tenth order. This prediction is in agreement with the most precise experiment so far, conducted at Harvard University [9], and is consistent in ten significant digits. Therefore one has certainly a good evidence to believe that the SM describes the nature accurately within its domain of validity.

1.1 Standard Model Particles

All particles and forces in the SM are described in terms of quantum fields which have as many degrees of freedom as there are different types and states of particles. Fundamentally there exist only quantum fields that span all space-time and they appear as particles only when observed. This property explains why particles of the same type are indistinguishable: they are excitations of the same underlying field.

The particle content of the SM comprises quarks, leptons, gauge bosons and the Higgs boson. Particles are categorized by the representations of the Lorentz group and of the internal symmetry groups of the SM. The Lorentz group of special relativity has two Casimir invariants: the four-momentum squared and the Pauli-Lubansky pseudovector squared, which means that they have the same values in all inertial frames of reference. The square (or, more precisely, the Minkowski inner product) of the four-momentum results in the rest mass squared of the particle and therefore particles can be classified by the value of their masses. Moreover, the Pauli-Lubanski pseudovector operator commutes with the four-momentum operator and therefore is used to label particles by their spin quantum number. On the other hand, the internal gauge groups of the SM have various representations which describe interactions of particles. Particles are said to have charges which can be a color, weak isospin, electromagnetic charges, and hypercharge. The diversity of the known elementary particles arise due to the variety of combinations of the different representations, as shown in Fig. 1.1.

The rest mass of a particle is the same for all observers in different frames of reference. Particles with zero mass always travel with the speed of light in vacuum. The SM contains only one truly massless particle, the photon, and for this reason

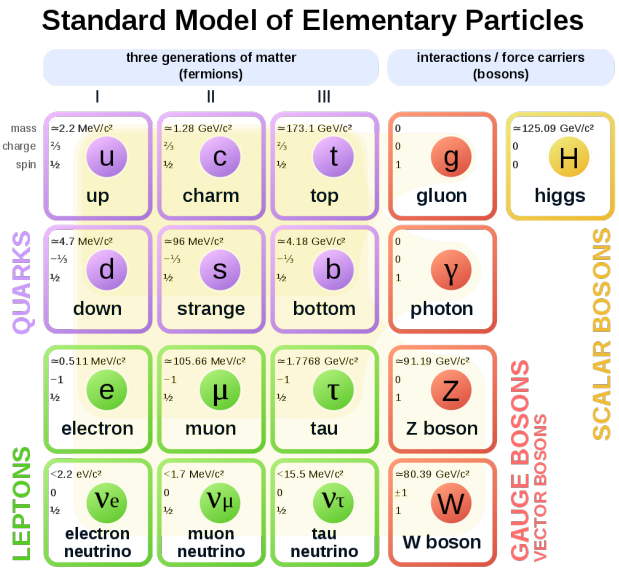

Figure 1.1: Particles of the Standard Model arranged by spin, mass, generation and electric charge [10].

the electromagnetic force is infinite-ranged. (The hypothesized elementary particle, the graviton, should also be massless due to the infinite-ranged gravitational force.) However, gluons also have no mass but their dynamical properties are very different from those of photons; gluons are confined and consequently the strong force is very short ranged. The neutrinos are also considered to be massless in the SM although in reality they have small masses of less than 2 eV[1] [11]. Other particles in the SM have masses ranging from 0.511 MeV [11] of the electron to the heaviest mass of 173 GeV [11] of the top-quark. Such a diversity of masses is unexplained by the SM and constitutes a part of the hierarchy problem.

Particles have an internal angular momentum, spin, which characterizes particle statistics. In terms of the reduced Plank constant, $\hbar$, particles can have either integer or half-integer spin. Particles having integer spin are called bosons because an ensemble of bosons obey Bose-Einstein statistics. Particles having half-integer spin are called fermions because an ensemble of fermions obey Fermi-Dirac statistics. Fermions have a notable property that they obey the Pauli exclusion principle.

Fermions in the SM, all having a spin equal to 1/2, are categorized into

[1]Natural units are used throughout the thesis.

quarks and leptons according to their quantum charges and hence the interactions they can undergo. Quarks are further categorized into up-type and down-type quarks, while leptons are further categorized into charged and neutral leptons. Quarks undergo all three types of interactions: strong, weak and electromagnetic. Charged leptons can participate in electromagnetic and weak interactions, while neutral leptons interact only weakly. All quarks and leptons are arranged into three generations which differ in the masses of the particles; the nature of the three generations is not explained by the SM.

There are six flavors of quarks: the up-type quarks are up (u), charm (c) and top (t); the down-type quarks are down (d), strange (s) and bottom (or beauty, b). The three charged leptons are the electron (e), muon (μ) and tau (or tauon, τ). The three neutral leptons are the neutrinos, named accordingly to the charged leptons: electron neutrino (ν_e), muon neutrino (ν_μ) and tau neutrino (ν_τ). Neutrinos have a property of neutrino oscillation which means that the neutrinos can change their flavor while propagating freely. Neutrino oscillation is not explained by the SM.

Different types of interactions between the elementary particles arise in two ways known so far: gauge and Yukawa interactions. The gauge interactions are those which constitute three forces of nature: electromagnetic, weak and strong. These interactions emerge from the principle of local gauge invariance and consequently are highly restrictive. On the other hand, Yukawa interactions do not seem to possess a kind of principle which could explain or constrain the strengths of interactions between different particles. This type of interaction appear between the Higgs boson and massive fermions.

Bosons in the SM comprise gauge bosons, which are spin 1 particles, and the Higgs boson, a spin 0 particle. The gauge bosons are the force carriers of the strong, weak and electromagnetic forces. Fermions with electric charges act as sources of the electromagnetic force carrier, the photon (γ). Quarks, which carry color charges, also act as sources of the strong force carrier, the gluon (g). Since all fermions participate in the weak interaction, they are all sources of the weak force carriers, the $W^\pm$ and Z bosons. The gluons themselves carry the color charge and therefore can interact with each other. Similarly, the $W^\pm$ and Z bosons carry the weak charge and can interact among themselves. The electrically charged weak force carriers, the $W^\pm$ bosons, also interact with the photon.

The Higgs boson (H) is the quanta of the Higgs field which generates masses for quarks, charged leptons, $W^\pm$ and Z bosons through interactions with them. While it is necessary to generate masses of the gauge bosons through the BEH

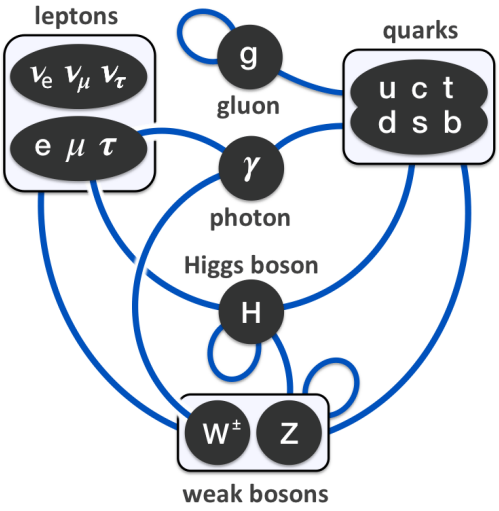

Figure 1.2: Interactions between particles in the SM [10].

mechanism in order to preserve gauge invariance, there is no a priori reason why fermion masses have to be generated in this way.

The interactions between all SM particles are schematically depicted in Fig. 1.2.

Quarks And Gluons

The six flavors of quarks have very different properties when it comes to mass, lifetime, decay channels and quantum charges. The up-type quarks have the electric charge equal to +2/3 in terms of the electron charge, while down-type quarks have it equal to -1/3. The masses range from a few MeV of the u and d quarks to the 173 GeV of the t quark. The large range of masses allow for decays of heavier quarks into lighter quarks but only through the weak force which can change the flavor of the quarks. The top quark decays almost exclusively into a bottom quark and W boson. Its lifetime is so short that a pair of top quarks can not form a bound state. All other quarks decay through a virtual W boson into one of the quarks which is lighter than the decaying one. The fact that the weak force can mix quark flavors from different generations is a consequence of non-matching flavor and mass eigenstates.

Quarks have a quantum number called color charge which is in some sense similar to the electric charge. The color charge can be of three distinct types and

each type have a positive or negative polarity, while the electric charge can only be of one type with different polarity. Hence, anti-quarks have an opposite color charge polarity than quarks, the anti-color. On the other hand, gluons have one color and one anti-color charges. For this reason gluons are sources for gluons themselves and therefore gluons and quarks can not exist in isolation. The self-interaction of gluons would build up a gluon field over the entire space in order to neutralize the color-charge but that would require an infinite amount of energy. Only color-neutral states can exist in a form of composite hadrons and, possibly, in a form of glueballs.

The color-neutral hadrons are composed of quarks which propagate in a field of gluons. The arrangement of quarks in hadrons is dictated by two effects. In terms of the color-charge, the most energetically feasible arrangement is to localize quarks in a single space point and consequently neutralize the color-charges. However, Heisenberg's uncertainty principle states that a precisely localized system would require a large amount of energy and therefore energetically it is more feasible for a system to be spread in space. These two opposing effects define the size and mass of hadrons. Since quarks in hadrons are not localized, a field of gluons is always present in hadrons and it constitutes some fraction of the total hadron's mass. In fact, hadrons composed of light quarks have the major fraction of their mass arising due to the gluon field. For example, the proton is composed of three light quarks, uud, which masses are estimated to be of a few MeV. However, the mass of the proton is $\approx 1\,\mathrm{GeV}$ and therefore the quarks constitute only a tiny fraction of that mass - most of the mass is generated by the gluon field.

All hadrons are categorized into baryons or mesons based on their baryon number. Quarks have a baryon number equal to $+1/3$ and anti-quarks have it equal to -1/3. A composite quark states with a baryon number equal to 1 is called a baryon and with a baryon number equal to 0 is called a meson. Almost all known baryons are composed of three quarks and almost all known mesons are composed of one quark and one anti-quark. Exotic baryon and meson states with more quarks are theoretically possible and a few of them have been discovered recently. An exotic baryon state with four quarks and an anti-quark, a pentaquark composed of $uucd\bar{c}$ quarks, has been recently observed by the LHCb collaboration in a decay of Λ_b^0 baryon [12]. Additionally, an exotic meson state with two quarks and two anti-quarks, a tetraquark composed of $c\bar{c}d\bar{u}$, was discovered in 2007 by the Belle collaboration [13] and later confirmed by LHCb [14]. It should be noted that a tetraquark and a pentaquark are different from a meson-meson and baryon-

meson molecules, respectively, although the quark content in the corresponding pairs is the same. A baryon-meson and meson-meson molecules are more similar to the deuterium, which is composed of a proton and a neutron rather than being a sextaquark.

Leptons

In this section the values of masses, lifetimes, branchig fractions and decay modes of the particles are taken from [11].

The electron was the first elementary particle to be discovered in the end of the 19th century. It is a stable particle with a mass of 0.511 MeV and therefore very common in everyday-world as it is a constituent of atoms.

The muon is an elementary particle with very similar properties to those of the electron but with a higher mass of 106 MeV. Muons on earth are naturally produced in cosmic rays. Protons arriving from the Sun interact with atomic nuclei in the earth's atmosphere and produce pions which subsequently decay into muons. Muons are unstable particles with a mean lifetime of 2.2 μs and the dominant decay channel $\mu \to \nu_\mu \bar{\nu}_e e$. This decay channel includes final states with additional photons and, moreover, a very small fraction of decays have additional $e^- e^+$ pairs. However, these decay modes are very rare and their branching fractions depend on the definition of energy values of the decay products.

The tau lepton was discovered in 1975 at Stanford Linear Accelerator Center (SLAC) [15] and earned the Nobel Prize in 1995 for its discoverer Martin Lewis Perl. Tau has a mass of 1.777 GeV making it the only lepton with both leptonic and hadronic decay modes. Leptonic decay products comprise either an electron or a muon with accompanying neutrinos, $\tau^- \to \nu_\tau \bar{\nu}_l l^-$, $l = e, \mu$, with charge-conjugate modes implied. Tau leptons decay leptonically 37% of the time approximately equally into e or μ. On the other hand, hadronic decay modes are very rich in variety, but most frequent decays comprise final states with one or three charged hadrons and zero or a few neutral hadrons. Tau lepton decay modes with one charged particle (1-prong) are $\tau^- \to \nu_\tau \pi^-$, which makes 11% of all decays, $\tau^- \to \nu_\tau \pi^- \pi^0$ (25%), $\tau^- \to \nu_\tau \pi^- \pi^0 \pi^0$ (9%), $\tau^- \to \nu_\tau \pi^- \pi^0 \pi^0 \pi^0$ (1%). Most frequent decay modes with three charged particles (3-prong) in the final state are $\tau^- \to \nu_\tau \pi^- \pi^- \pi^+$ (10%) and $\tau^- \to \nu_\tau \pi^- \pi^- \pi^+ \pi^0$ (5%). The decay modes listed above can have variations with a K^- or K^0 instead of π^- or π^0, respectively, but these decay modes make just a small fraction of the corresponding decay modes with

pions only. Decay modes with five charged particles make less than 1% of all decay modes.

Neutral leptons, the neutrinos, are stable particles with masses below 2 eV. In the weak interactions with a W boson, a neutrino of a specific flavor is always accompanied by a charged lepton of the corresponding flavor due to the lepton number conservation. For example, in a β decay, $n^0 \to p^+ + e^- + \bar{\nu}_e$, the electron number is conserved. In a similar but inverse process of neutrino interaction with matter, $\bar{\nu}_\mu + p^+ \to n^0 + \mu^+$, the muon number is conserved; similarly, the tau number is conserved. Although in the weak interactions the lepton number is conserved, neutrinos can change their flavor while propagating. This phenomenon, known as neutrino oscillation, happens because neutrino flavor and mass eigenstates do not coincide (it was the first evidence that neutrinos have mass). A neutrino produced in a flavor eigenstate is a superposition of three mass eigenstates which quantum mechanical phases evolve at slightly different rates. The phase differences change the superposition of the mass eigenstates and corresponds to a different superposition of flavor eigenstates. Depending on the energy and the distance the neutrino travels, it has some probability to interact as having one of the three flavors.

1.2 Standard Model Structure

The Standard Model is a gauge theory with the $SU(3)_c \times SU(2)_L \times U(1)_Y$ underlying local gauge symmetry which is spontaneously broken by the Higgs field and having the remaining $SU(3)_c \times U(1)_{EM}$ symmetry. The SM Lagrangian is invariant under the local gauge symmetry group transformations.

The $SU(3)_c$ symmetry group is the symmetry of quantum chromodynamics, hence the subscript c referring to the color charge. In QCD, quarks are represented by quantized Dirac fields in the fundamental representation, **3**, of the $SU(3)$ group. Gluons are represented by quantized Maxwell fields in the adjoint representation, **8**, of the symmetry group. The $SU(3)_c$ symmetry is not broken by the presence of the Higgs field. The part of the SM Lagrangian including only quark and gluon fields is invariant under the $SU(3)$ local gauge transformations.

The $SU(2)_L \times U(1)_Y$ symmetry group is the underlying symmetry of the electroweak theory. Left-chiral projections of the quark and lepton fields are arranged into doublets belonging to the fundamental representation, **2**, of the $SU(2)$ symmetry group, hence the subscript L; right-chiral projections belong to the singlet representation, **1**. Particles that belong to the fundamental representation of

Table 1.1: Representations of fermions under the SM gauge symmetry groups.

Fermions \ Symmetry group	$SU(3)_c$, $SU(2)_L$, $U(1)_Y$
Quarks	
$\begin{pmatrix} u_L \\ d_L \end{pmatrix}$	(**3**, **2**, 1/3)
u_R	(**3**, **1**, 4/3)
d_R	(**3**, **1**, -2/3)
Leptons	
$\begin{pmatrix} \nu_{eL} \\ e_L \end{pmatrix}$	(**1**, **2**, -1)
e_R	(**1**, **1**, -2)

the aforementioned group have a quantum number called weak isospin. The 3rd component of the weak isospin, T_3, is equal to $\pm 1/2$, similarly to the representation of angular momentum. Particles that belong to the singlet representation have the weak isospin equal to 0. Similarly, the $U(1)_Y$ symmetry group refers to a quantum number called hypercharge, Y. Quarks and leptons have values of the hypercharge according to the Gell-Mann–Nishijima formula

$$Q = T_3 + \frac{Y}{2}, \tag{1.2.1}$$

where Q is the electric charge. The $SU(2)_L$ symmetry group has three generators which belong to the adjoint representation, and the $U(1)_Y$ have one symmetry generator. These generators are represented by massless spin-1 quantum fields which, after the spontaneous symmetry breaking, become the $W^{\pm}$, Z bosons and the photon. The fundamental symmetry $SU(2)_L \times U(1)_Y$ is spontaneously broken by the presence of the Higgs field and only the symmetry of QED, $U(1)_{EM}$, remains.

Table 1.1 lists the representations of the first generation fermions under the SM symmetry group. Fermions of the remaining two generations are in the same representations as the corresponding fermions of the first generation. Only left-chiral neutrinos have interactions in the SM.

1.2.1 Local Gauge Symmetry

The principle of local gauge invariance is best explained in the theory of classical electrodynamics which has the $U(1)$ local gauge symmetry. A $U(1)$ symmetry group is an abelian Lie group meaning that the elements of the group commute with each other as opposed to non-abelian Lie groups which elements do not commute. The Lagrangian of electrodynamics is

$$\mathcal{L}_{EM} = -\frac{1}{4}F_{\mu\nu}F^{\mu\nu} + i\bar{\psi}(\gamma_\mu\partial^\mu - m)\psi - e\bar{\psi}\gamma_\mu\psi A^\mu, \tag{1.2.2}$$

where $F^{\mu\nu} = \partial^\mu A^\nu - \partial^\nu A^\mu$ is the electromagnetic field strength tensor, A^μ is the vector field, ψ is a fermion field, m is the mass of the fermion field, e is the electric charge and γ^μ are the Dirac matrices. The Lagrangian is invariant under the local gauge transformation

$$A_\mu(x) \to A_\mu^{'}(x) = A_\mu(x) - \frac{1}{e}\partial_\mu\alpha(x), \tag{1.2.3}$$

$$\psi(x) \to \psi^{'}(x) = e^{i\alpha(x)}\psi(x). \tag{1.2.4}$$

The transformation parameter $\alpha(x)$ is a function of space-time coordinates, hence the transformation is local. The partial derivative in the Dirac part[2] of the Lagrangian results in a $\partial_\mu\alpha(x)$ term when the transformation in Eq. 1.2.4 is applied. However, the interaction term in the Lagrangian provides an equal term but with opposite sign when the transformation in Eq. 1.2.3 is applied and therefore the $\partial_\mu\alpha(x)$ terms cancel. The requirement of local gauge invariance generates the interaction term and defines the structure of the interaction. This requirement also forbids the mass term of the vector field which has the form $m^2A_\mu A^\mu$. The Lagrangian can be neatly rewritten with a covariant derivative, defined as $D_\mu = \partial_\mu + ieA_\mu$, which makes the Lagrangian manifestly covariant:

$$\mathcal{L}_{EM} = -\frac{1}{4}F_{\mu\nu}F^{\mu\nu} + i\bar{\psi}(\gamma_\mu D^\mu - m)\psi. \tag{1.2.5}$$

The non-abelian symmetry groups of the SM are described with gauge theories which are also called Yang-Mills theories. As in the case of QED, the local gauge invariance fixes the interaction terms in QCD and electroweak theories. The

[2]The Lagrangian that describes a free massive fermion field and gives rise to the Dirac equation.

generators of the $SU(3)$ Lie group satisfy the commutation relation

$$\left[\lambda^a, \lambda^b\right] = 2if^{abc}\lambda^c, \tag{1.2.6}$$

where in the fundamental representation λ^a are the eight Gell-Mann matrices and f^{abc} are the structure constants of the group. The QCD Lagrangian is

$$\mathcal{L}_{QCD} = -\frac{1}{4}G^a_{\mu\nu}G^{a\,\mu\nu} + i\bar{q}_i(\gamma_\mu D^\mu_{ij} - m\delta_{ij})q_j, \tag{1.2.7}$$

where $G^a_{\mu\nu}$ are eight gluon field strength tensors, q_i are quark spinor fields and D^μ_{ij} is the $SU(3)$ covariant derivative. Index a labels color states in the **8** representation, and indices i, j label color states in the **3** representation of the $SU(3)$. For this Lagrangian to be covariant under a local $SU(3)$ transformation, the covariant derivative must have the form

$$D^\mu_{ij} = \partial^\mu\delta_{ij} + ig_s\frac{\lambda^a_{ij}}{2}A^{a\,\mu}. \tag{1.2.8}$$

Moreover, the field strength tensor happens to be of the form

$$G^a_{\mu\nu} = \partial_\mu A^a_\nu - \partial_\nu A^a_\mu - g_s f^{abc}A^b_\mu A^c_\nu. \tag{1.2.9}$$

The non-linear term in the field strength tensor, which is present in all Yang-Mills theories, makes the gauge fields self-interacting and therefore gluons, $W^\pm$ and Z bosons interact with themselves. Moreover, the coupling constants are fixed by the local gauge invariance and are universal. Hence, the strong coupling constant of QCD, g_s, is the same in the gluon-gluon and gluon-quark interactions, as seen from the equations above.

The structure of the $SU(2)$ Yang-Mills theory is similar to that of the $SU(3)$, but in the SM it becomes more complicated because of the BEH mechanism, which will be described below. In the case of the $SU(2)$ Lie group, the generators satisfy the commutation relation

$$\left[\sigma^i, \sigma^j\right] = 2i\epsilon^{ijk}\sigma^k, \tag{1.2.10}$$

where in the fundamental representation σ^i are the Pauli matrices and ϵ^{ijk} are the structure constants of the group, which also coincide with the totally anti-symmetric Levi-Civita symbol in three dimensions.

Without the Higgs field, the Standard Model is manifestly $SU(3)_c \times SU(2)_L \times U(1)_Y$ covariant. From what was written above, it is clear that this gauge group invokes the existence of an octet of $SU(3)$ fields, a triplet of $SU(2)$ fields and a $U(1)$ singlet. The kinetic terms of the gauge fields in the Lagrangian are

$$\mathcal{L}_{gauge} = -\frac{1}{4} G^a_{\mu\nu} G^{a\,\mu\nu} - \frac{1}{4} W^i_{\mu\nu} W^{i\,\mu\nu} - \frac{1}{4} B_{\mu\nu} B^{\mu\nu}, \tag{1.2.11}$$

where the field strength tensors are

$$W^i_{\mu\nu} = \partial_\mu W^i_\nu - \partial_\nu W^i_\mu - g\epsilon^{ijk} W^j_\mu W^k_\nu, \tag{1.2.12}$$

$$B_{\mu\nu} = \partial_\mu B_\nu - \partial_\nu B_\mu, \tag{1.2.13}$$

$$G^a_{\mu\nu} = \partial_\mu G^a_\nu - \partial_\nu G^a_\mu - g_s f^{abc} G^b_\mu G^c_\nu. \tag{1.2.14}$$

The covariant derivative involving all the gauge fields has the form

$$D_\mu = \partial_\mu + ig\frac{\sigma^i}{2} W^i_\mu + ig'\frac{Y}{2} B_\mu + ig_s \frac{\lambda^a}{2} G^a_\mu. \tag{1.2.15}$$

The coupling constants g and g' arise from the $SU(2)_L$ and $U(1)_Y$ gauge groups, respectively. Appropriate terms in the covariant derivative have to be picked up for each fermion depending on its representation (Table 1.1). The $SU(2)$ part involving σ^i applies only to fermions under the **2** representation of the group. For the **1** representation of the $SU(2)$ group (right-chiral fermions), the σ^i have to be replaced with a zero. The $SU(3)$ part involving λ^a applies only to quarks; for leptons the λ^a have to be replaced with a zero.

Combining together fermion multiplets with covariant derivatives, the fermion part of the Lagrangian for one generation is

$$\mathcal{L}_{fermion} = i\overline{\psi}_L \not{D} \psi_L + i\overline{\psi}_Q \not{D} \psi_Q + i\overline{\psi}_{e_R} \not{D} \psi_{e_R} + i\overline{\psi}_{u_R} \not{D} \psi_{u_R} + i\overline{\psi}_{d_R} \not{D} \psi_{d_R}. \tag{1.2.16}$$

Here ψ_L stands for the $SU(2)_L$ lepton doublet, ψ_Q is the quark doublet, ψ_{e_R} is the right-chiral $SU(2)$ singlet electron field, and similarly for the right-chiral quark fields. All quark fields are also $SU(3)$ triplets. All interactions are contained in the covariant derivatives. The different character of the $SU(2)$ transformations for the left- and right-chiral fields prevents the existence of Dirac mass terms in the Lagrangian. The masses for the quarks and charged leptons are generated by their interactions with the Higgs field.

1.2.2 Asymptotic Freedom

Coupling constants, such as the fine structure constant of QED and the strong coupling of QCD, are not constants whatsoever but their physical values depend on the energy scale. This phenomenon happens due to virtual particles in the vacuum which have only an indirect effect to the interactions and this effect results in the change of the coupling constants. At large distance or small energy scales the fine structure constant, α, appears weaker because the electric charge is screened by virtual electron-positron pairs in the vacuum. Conversely, at small distance or large energy scales α appears stronger because the interacting probe can penetrate the shield of virtual pairs around the charge. The physical value of α is around $1/137$ at $Q^2 = 0$ and around $1/129$ at $Q^2 = m_Z^2$.

Generally, the running behavior of a coupling constant depends on the gauge group and the number of fermion flavors participating in the interactions. The $SU(3)$ gauge group of QCD and six quark flavors is a very different setup from the QED case and therefore the running of the strong coupling constant, α_s, behaves oppositely to the running of the fine structure constant. In QCD, gluons can interact with themselves and this creates an anti-screening effect of the color-charge which is opposite to the screening effect in QED. The running of the strong coupling constant can be expressed with the equation

$$\alpha_s(Q^2) = \frac{\alpha_s(\mu^2)}{1 + b\alpha_s(\mu^2) \ln \frac{|Q^2|}{\mu^2}}. \tag{1.2.17}$$

This equation shows how interaction strength changes with the interaction energy scale, Q^2, given the interaction strength at a renormalization scale, μ^2. The coefficient

$$b = \frac{33 - 2N_f}{12\pi}, \tag{1.2.18}$$

where N_f is the number of quark flavors, dictates the character of this change. For the quark content in the SM, the coefficient b is positive and therefore α_s decreases with the energy scale. This very important property is called the asymptotic freedom and it explains the existence of free-like particles inside hadrons. Asymptotic freedom allows the application of perturbation theory in high energy regime where the series expansion in α_s converges. Conversely, at the low end of the energy spectrum, or at large distance scales, QCD becomes very strongly interacting and

for this reason quarks are confined within hadrons.

1.3 Brout-Englert-Higgs Mechanism

Local gauge invariance prevents gauge bosons from having mass because the mass term is not gauge invariant. This is in contradiction with the observed masses of the $W^{\pm}$ and Z bosons. The principle of local gauge invariance is fundamental to QCD and QED and therefore it is desirable to retain it in the electroweak theory. Generally, gauge invariant theories are preferred because they are renormalizable. The Brout-Englert-Higgs mechanism contains a brilliant way of explaining the observed masses of the gauge bosons. With this particular mechanism the underlying gauge symmetry of the electroweak theory is preserved and the $W^{\pm}$ and Z bosons acquire masses. The BEH mechanism predicted the existence of a scalar neutral particle called the Higgs boson which discovery at the LHC in 2012 [16, 17] finally completed the SM. Peter Higgs and Francois Englert were awarded the Nobel prize in the subsequent year (Robert Brout died in 2011).

In addition to the gauge fields in the electroweak sector that arise from the requirement of local gauge invariance, there is a complex $SU(2)$ doublet Higgs field of hypercharge $Y = 1$:

$$\Phi = \begin{pmatrix} \Phi^{+} \\ \\ \Phi^{0} \end{pmatrix} \tag{1.3.1}$$

The $T_3 = 1/2$ component has one unit of electric charge and the $T_3 = -1/2$ is electrically neutral, according to Gell-Mann–Nishijima formula 1.2.1. The scalar Higgs field in the Lagrangian has a Klein-Gordon kinetic term which involves covariant derivatives 1.2.15 and therefore the Higgs field couples to the gauge fields. The part of the SM Lagrangian involving only the Higgs and electroweak gauge fields is manifestly $SU(2)_L \times U(1)_Y$ covariant:

$$\mathcal{L}_{\Phi,G} = (D_\mu \Phi)^\dagger (D^\mu \Phi) + \mu^2 \Phi^\dagger \Phi - \frac{\lambda}{4}(\Phi^\dagger \Phi)^2 - \frac{1}{4} W^i_{\mu\nu} W^{i\,\mu\nu} - \frac{1}{4} B_{\mu\nu} B^{\mu\nu}. \tag{1.3.2}$$

The form of Higgs potential is restricted by the gauge symmetry and renormalizability and therefore it can only depend on $\Phi^\dagger\Phi$ and contain dimension-four operators. The sign in front of the Higgs mass term is reversed compared to the usual form of Lagrangians and this shifts the classical Higgs potential minimum away from the

origin. The value of the potential is minimal at the Higgs field value Φ_0, where

$$\Phi_0^\dagger \Phi_0 = \frac{v^2}{2}, \quad v = 2\sqrt{\frac{\mu^2}{\lambda}}. \tag{1.3.3}$$

The non-zero vacuum expectation value (vev) should be assigned to the lower component of this doublet, because it is electrically neutral, and so is the vacuum:

$$\langle 0|\Phi|0\rangle = \begin{pmatrix} 0 \\ v/\sqrt{2} \end{pmatrix} = \Phi_0. \tag{1.3.4}$$

Then, quantum fluctuations about the ground state Φ_0 can be parametrized in the unitary gauge as

$$\Phi_{U-gauge} = \begin{pmatrix} 0 \\ \frac{1}{\sqrt{2}}(v+H) \end{pmatrix}, \tag{1.3.5}$$

where the physical Higgs field, H, has zero vev. This is a very simple parametrization where the missing three components of the doublet can be gauged away due to the symmetry being local [18]. After rewriting the Lagrangian in Eq. 1.3.2 in terms of this particular Higgs parametrization and using explicit expressions of the covariant derivatives one finds (keeping only quadratic terms):

$$\begin{aligned}
\mathcal{L}_{\Phi,G;quad} =& \frac{1}{2}\partial_\mu H \partial^\mu H - \mu^2 H^2 \\
&- \frac{1}{4}(\partial_\mu W^1_\nu - \partial_\nu W^1_\mu)(\partial^\mu W^{1\,\nu} - \partial^\nu W^{1\,\mu}) + \frac{1}{8}v^2 g^2 W^1_\mu W^{1\,\mu} \\
&- \frac{1}{4}(\partial_\mu W^2_\nu - \partial_\nu W^2_\mu)(\partial^\mu W^{2\,\nu} - \partial^\nu W^{2\,\mu}) + \frac{1}{8}v^2 g^2 W^2_\mu W^{2\,\mu} \\
&- \frac{1}{4}(\partial_\mu W^3_\nu - \partial_\nu W^3_\mu)(\partial^\mu W^{3\,\nu} - \partial^\nu W^{3\,\mu}) - \frac{1}{4}B_{\mu\nu}B^{\mu\nu} \\
&+ \frac{v^2}{8}(gW^3_\mu - g'B_\mu)(gW^{3\,\mu} - g'B^\mu).
\end{aligned} \tag{1.3.6}$$

A combination of the gauge fields W^3_μ and B_μ appear in the equation which imply

mixing and therefore is parametrized as

$$\begin{pmatrix} Z_\mu \\ A_\mu \end{pmatrix} = \begin{pmatrix} \cos\theta_W & -\sin\theta_W \\ \sin\theta_W & \cos\theta_W \end{pmatrix} \begin{pmatrix} W_\mu^3 \\ B_\mu \end{pmatrix}, \tag{1.3.7}$$

where θ_W is called the weak mixing angle and

$$\sin\theta_W = \frac{g'}{\sqrt{g^2 + g'^2}}. \tag{1.3.8}$$

Using this parametrization in the covariant derivative 1.2.15, it becomes

$$D_\mu = \partial_\mu + i\frac{g}{\sqrt{2}}(\sigma^+ W_\mu^+ + \sigma^- W_\mu^-) + i\frac{g}{\cos\theta_W} Z_\mu (\frac{\sigma^3}{2} - \sin^2\theta_W Q) + ieQA_\mu \tag{1.3.9}$$

where

$$W_\mu^\pm = \frac{1}{\sqrt{2}}(W_\mu^1 \mp iW_\mu^2), \tag{1.3.10}$$

$$\sigma^\pm = \frac{1}{2}(\sigma^1 \pm i\sigma^2). \tag{1.3.11}$$

Many parameters can be identified in equations 1.3.6 and 1.3.9. Mass terms of some gauge fields appear in the Lagrangian. They arise from the interaction terms between the gauge fields and the Higgs doublet and depend on the vacuum expectation value v. The masses of the $W^\pm$ and Z bosons are

$$m_W^2 = \frac{v^2}{4} g^2, \tag{1.3.12}$$

$$m_Z^2 = \frac{v^2}{4}\sqrt{g^2 + g'^2}. \tag{1.3.13}$$

The electric charge, e, in this model is expressed in terms of coupling constants g and g':

$$e = \frac{gg'}{\sqrt{g^2 + g'^2}}. \tag{1.3.14}$$

Fermion couplings to the Z boson depend on the weak isospin, electric charge and the weak mixing angle. Moreover, the vacuum Φ_0 is invariant under the transfor-

mation

$$\Phi_0 \to e^{i\alpha(\frac{1}{2}+\frac{\sigma_3}{2})}\Phi_0 = \Phi_0. \tag{1.3.15}$$

This unbroken symmetry corresponds to the remaining gauge field which stays massless after the electroweak symmetry breaking, i.e. the photon.

The Higgs boson itself has a mass $m_0 = v\sqrt{\lambda/2}$, but since λ is a free parameter, this mass can not be predicted in the SM. Moreover, radiative corrections of this mass at one loop order involves the four-point interaction with the coupling λ, which produces quadratic divergences proportional to Λ, the cut-off scale. Hence, the physical mass is related to the Lagrangian parameter by $m_{ph}^2 = m_0^2 - \Lambda^2$. The difference between the measured value of the physical mass, $m_{ph} \approx 125\,\mathrm{GeV}$, and the cut-off scale, Λ, which should be of order $10^{16}\,\mathrm{GeV}$, impose the fine tuning problem. It is unclear how the difference of two huge numbers of order $10^{16}\,\mathrm{GeV}$ turn out to be this small physical Higgs mass.

1.4 Fermion masses and the CKM matrix

The principle of local gauge invariance and the fact that the nature treats left- and right-chiral fermion fields differently prevents explicit Dirac mass terms in the Lagrangian. In fact, all fermions do have masses and therefore a more complicated mechanism must exist if the gauge invariance ought to be preserved. It is possible to write down $SU(2)_L$ invariant interaction terms between ciral components of the fermion fields and the Higgs field, which would result in fermion mass terms after spontaneous symmetry breaking.

The $SU(2)_L \times U(1)_Y$ manifestly invariant fermion-Higgs interaction terms are

$$\mathcal{L}_{Yukawa} = y_l^{ij}\overline{\Psi}_L^i \Phi \Psi_{l_R}^j + y_d^{ij}\overline{\Psi}_Q^i \Phi \Psi_{d_R}^j + y_u^{ij}\overline{\Psi}_Q^i \Phi^C \Psi_{u_R}^j + h.c., \tag{1.4.1}$$

where Φ^C is the charge-conjugate of the Higgs doublet. Yukawa couplings y^{ij} are 3×3 matrices (diagonal in this basis) for the 3 generations of particles and they allow mixing across the generations. There is no term with right-chiral neutrinos since they do not exist (at least in the SM) and therefore mass terms for the neutrinos are not generated by the Higgs field. After electroweak symmetry breaking and

rotation into mass diagonal basis, the Yukawa terms simplify to

$$\mathcal{L}_{Yukawa} = -\sum_{fermions} m_f \left(\overline{\Psi'}_{f_L}\Psi'_{f_R} + \overline{\Psi'}_{f_R}\Psi'_{f_L}\right)\left(1+\frac{H}{v}\right). \tag{1.4.2}$$

where the prime denotes fields in the mass basis and the sum goes over massive fermions. Here, the masses are functions of the vev and Yukawa couplings, but they can not be predicted from this model and are simply set by hand to give the observed masses. This also generates interaction terms between fermions and the Higgs boson with coupling strengths proportional to fermion masses. Measurements of Higgs boson decay rates to fermions are important tests of the electroweak symmetry breaking.

Gauge interaction terms between quarks and charged gauge fields will involve flavor mixing terms, due to non-diagonal σ^i matrices, of the form

$$\overline{\Psi}^i_{u_L} \not{W}^+ \Psi^j_{d_L} \tag{1.4.3}$$

After the rotation to the mass basis using

$$\Psi'^a_{d_L} = U^{aj}_{d_L}\Psi^j_{d_L}, \quad \Psi'^b_{u_L} = U^{bj}_{u_L}\Psi^j_{u_L}, \tag{1.4.4}$$

the product of mixing matrices will appear:

$$V^{CKM} = U_{u_L}U^\dagger_{d_L}. \tag{1.4.5}$$

Matrix V^{CKM} is called Cabibbo-Kobayashi-Maskawa matrix [19][20] and it shows relative strengths of weak charged currents of quarks coupling to $W^\pm$ and this explains why hadrons composed of second and third generation quarks can decay weakly into hadrons containing lower generation quarks. The flavor mixing is quite weak and the diagonal elements of the CKM matrix are close to unity. Since V^{CKM} is a 3×3 unitary matrix, it can be parametrized with four parameters. Three parameters are quark mixing angles and the fourth parameter is a phase which can not be absorbed into the definition of quark fields and causes violation of the $\mathcal{CP}$ symmetry. $\mathcal{CP}$ violation has been observed in kaon [21], as well as D [22] and B [23] meson, systems.

Physical processes causing $\mathcal{CP}$ violation are necessary in order to explain matter–anti-matter asymmetry in the Universe, according to Sakharov conditions [24]. However, the amount of violation arising from the CKM matrix is insufficient

to account for the matter dominance in our Universe, and therefore other sources of $\mathcal{CP}$ violation must be present. One of such sources might be found in the lepton sector where lepton mixing occurs, as is the case of neutrino oscillations. The lepton mixing matrix, analogous to the CKM matrix, is called the Pontecorvo-Maki-Nakagawa-Sakata matrix [25][26], which contains a complex phase. To this day the measured value of this phase is consistent with $\mathcal{CP}$ conservation [27].

1.5 Proton-Proton Collisions

In hadron colliders, and in the LHC particularly, the colliding particles are protons which are not elementary but composite states consisting of quarks and gluons, collectively called partons. This makes the initial state rather complicated and all of the pp collision events are collective interactions of multiple partons mostly interacting at relatively low energies. But every now and then there is a hard scattering event in which two initial partons, carrying relatively high fraction of proton's energy and momentum, interact with each other. During such hard collisions the partons undergo high momentum transfer which means that the interaction time is rather short and therefore the initial state partons are behaving as if they are free particles. The interaction strength at high momentum transfer is relatively small due to asymptotic freedom, and cross sections of such collisions can be calculated in perturbative QCD. It is impossible to know which partons have undergone the interaction and with what initial energy thus only a probabilistic description of partons inside the proton can be obtained. The probability to find a parton of a certain flavor and energy is described with parton distribution functions (PDF). It is not strictly a distribution of probability but rather a distribution of an average number of each type of parton that carries a fraction of the proton's total four-momentum. The reason why the number of partons in a proton is not constant is because the proton is a very active and dynamical place where virtual gluons, quarks and anti-quarks are perpetually popping in the existence and subsequently disappearing. The virtual quarks inside a proton are also called sea-quarks, in contrast to the three valence quarks which make up the proton and are always present. A high energy probe (a parton from another proton) can resolve the short distance structure of the proton and can interact with virtual partons. This suggests that what is seen by the probe depends on the energy of the probe, or, rather, on the interaction scale. The evolution of parton distribution functions with the energy scale is calculated in QCD and results in DGLAP equations named after Dokshitzer,

Gribov, Lipatov, Altarelli, Parisi, who were the first to derive them [28].

A typical example of the PDFs is shown in Fig. 1.3 from the MSTW collaboration. Generally, there is a small number of partons with a significant fraction of proton's total momentum and vastly increasing number of those partons which carry only a small fraction of the total momentum. The u and d quarks have higher probabilities to have a significant fraction because there are always three valence quarks in a proton. On the other hand, sea-quarks of heavier flavor tend to have lower momenta. Gluons also have a significant part of the protons momentum and, as mentioned before, a considerable amount of energy is contained in the gluon field which makes almost all of the proton's rest mass. The evolution of PDFs with the interaction scale is clearly visible in the plots. The probability for a probe to interact with a low energy parton increases with the interaction scale because the probe can resolve finer structures of the virtual pairs inside the proton.

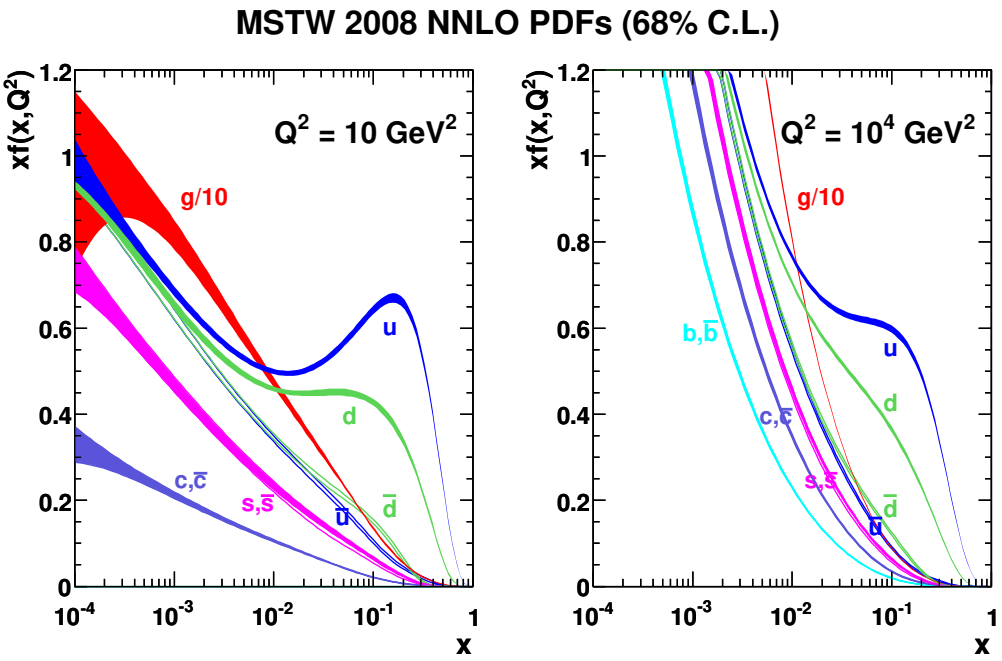

Figure 1.3: Parton distribution functions from the MSTW group [29]. The plots show the distributions for valence quarks, sea-quarks, and gluons, and the evolution of distributions from the interaction scale of (left) $Q^2 = 10\,\mathrm{GeV}^2$ to (right) $Q^2 = 10^4\,\mathrm{GeV}^2$.

Given the parton distribution functions and the parton level cross sections calculated in perturbative QCD, the proton level differential cross section of a

particular final state can be calculated with the formula

$$d\sigma_{pp\to X} = \sum_{q_1,q_2} \int_0^1 dx_1 dx_2 f_{q_1}(x_1, Q^2) f_{q_2}(x_2, Q^2) d\sigma_{q_1 q_2 \to X}(x_1, x_2, Q^2). \quad (1.5.1)$$

Here $f_{q_i}(x_i, Q^2)$ are the PDFs of the two interacting partons, $d\sigma_{q_1 q_2 \to X}(x_1, x_2, Q^2)$ is the parton level differential cross section for the required final state. The sum is carried over all parton pairs which provide the required final state and the integration is performed over proton momentum fractions x_i.

The proton-proton collision cross sections of some final states are shown in Fig. 1.4. Generally, cross sections for the production of heavy particles increase with the center-of-mass energy of protons because the probability to have high-energy partons required for the creation of heavy states increases. The probability to produce a heavy particle, such as a massive gauge boson, is much smaller than the total pp collision probability. Also, due to the presence of quarks and gluons in the initial state and the dominance of the strong force over the other forces, hadrons are produced more strongly.

1.6 Supersymmetry

It is well known that the Standard Model, although being a very successful theory, is incomplete as it fails to address a few problems in particle physics. Supersymmetry (SUSY) [31] is a possible candidate for undiscovered particle physics and it provides solutions to some of the existing problems.

A dark matter candidate is present in many supersymmetric versions of the Standard Model. The lightest supersymmetric particle is both heavy and stable and is a candidate for a weakly interactive massive particle (WIMP) which is a particular type of dark matter. Dark matter is a form of matter which constitutes about 27% of all mass-energy content in the universe, but its nature is still unknown. The most compelling evidence of dark matter comes from observations of cosmic microwave background (CMB) radiation which suggests that the existence of dark matter is necessary to explain temperature anisotropy in the CMB radiation. The most recent measurements of dark matter density in the Universe comes from the Planck Collaboration [32]. Additionally, indirect evidence of dark matter comes from astrophysical observations of rotation curves of galaxies and of at least one instance of colliding clusters of galaxies, the Bullet Cluster.

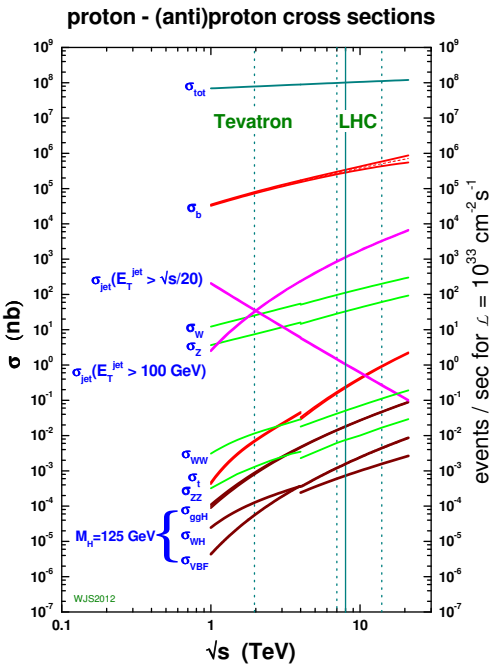

Figure 1.4: Cross sections of various processes in proton-(anti)proton collisions as a function of the center-of-mass energy [30]. Line discontinuities appear due to differences between proton–anti-proton (applicable at the Tevatron) and proton–proton (applicable at the LHC) collisions.

Supersymmetry also provides gauge coupling unification. The three coupling constants in the SM are running constants but they do not have similar values at any energy scale, i.e. they do not meet at a single energy. Additional particles that must be introduced in supersymmetric versions of the SM change the behavior of the running constants and consequently the three coupling constants become unified at a large energy.

Moreover, there are a few hints of new physics observed in decays of B mesons that can be explained by the existence of new particles. The LHCb collaboration tested lepton universality in a few particular B meson decay modes, which are sensitive to possibly undiscovered particles. In particular, the LHCb collaboration measured the ratio of branching fractions $\bar{B}^0 \to D^{*+}\tau^-\bar{\nu}_\tau$ and $\bar{B}^0 \to D^{*+}\mu^-\bar{\nu}_\mu$, called R_{D^*} [33]. Such decays modes with a tau lepton in the final state are sensitive to charged Higgs bosons due to their naturally large coupling to massive particles. The measured ratio of branching fractions is found to be larger than predicted by

the SM at a level of $\approx 2.1\sigma$. This result is in agreement with earlier measurements performed by the BaBar and Belle collaborations (see references in [33]).

Finally, the SM suffers from the fine-tuning problem in which the observed mass of the Higgs boson is much smaller than what could be expected from theory. This is explained in greater detail in the next section.

1.6.1 The Fine-Tuning Problem

The Standard Model is a renormalizable theory which can, technically, be calculated up to infinite energy. But there is a wide range of energy scales between the explored electroweak scale, set by the vacuum expectation value $v \approx 246\,\text{GeV}$, and the scale at which quantum gravity effects are supposed to become important. Namely the (reduced) Plank scale, $M_{Pl} = (8\pi G_N)^{-1/2} \simeq 2.4 \times 10^{18}\,\text{GeV}$, where G_N is Newton's constant. It is very likely that in this vastness of scales stretching 16 orders of magnitude, there are new undiscovered particles. In the presence of additional particles theoretical predictions of the SM will start to break down at the scales of the masses of the new particles. Even if there are no new particles, the highest allowed mass scale for the SM is the Plank scale. Here, gravity becomes strong, and the SM is bound to break down simply because gravity is not part of it. One particular case in theoretical calculations suggests either additional structures to the SM are needed, or that the Plank scale is not as huge as set simply by Newton's constant. These hints come from calculations of radiative corrections to the mass of the Higgs boson [31].

Consider a set of particular one-loop corrections to Higgs self-energy, represented by Feynman diagrams in Fig. 1.5. These corrections arise from Higgs boson (H) interactions with a fermion (f) and a scalar (S). The interactions are of the form $-\lambda_f H \bar{f} f$ and $-\lambda_S |H^2||S^2|$, where λ_f and λ_S are dimensionless coupling constants. The one-loop diagram with a fermion loop gives a correction to the Higgs boson mass:

$$\Delta m_H^2 = -\frac{|\lambda_f|^2}{8\pi^2}\Lambda^2 + \dots\,, \tag{1.6.1}$$

where Λ is the ultraviolet cut-off scale. Equation 1.6.1 shows that quantum corrections to the Higgs boson mass are proportional to Λ^2; a huge number if the cut-off is the Plank scale. We know the physical mass of the Higgs boson is 125 GeV. Therefore, the Higgs boson mass parameter in the Lagrangian must be of the order Plank mass to cancel this radiative correction, giving the small measured Higgs

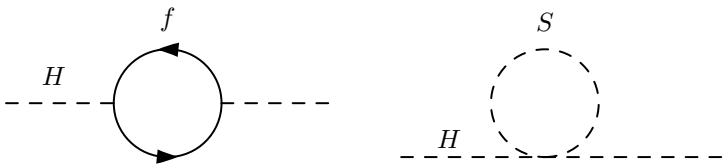

Figure 1.5: One-loop radiative corrections to the Higgs mass due to (left) a fermion and (right) a scalar.

boson mass. The cancellation of two numbers of the order $10^{18}\,\mathrm{GeV}$, resulting in the number of the order $10^{2}\,\mathrm{GeV}$, seems unnatural. This is the fine-tuning problem.

The second diagram in Fig. 1.5 of Higgs field interaction with a scalar field (or Higgs self-interaction) gives a correction to the Higgs boson mass that also has quadratic divergence:

$$\Delta m_H^2 = \frac{\lambda_S}{16\pi^2}\Lambda^2 + \dots . \tag{1.6.2}$$

Reference [31] demonstrates the problem is even worse. Any additional heavy particle, if they exist, that do not necessarily have a direct coupling to the Higgs boson, but have an interaction mediated by a gauge field, will lead to a quadratically divergent mass correction. It seems elementary scalar fields are condemned to feel influence of the largest masses and of the ultraviolet cut-off.

There exist at least two different ways to remedy the fine-tuning problem. One is to revise the assumption that the cut-off scale, currently thought to be the Plank scale, is actually that big. This is investigated in the theory of large extra dimensions (LED) [34], in which it is assumed that the apparent weakness of gravity (and by consequence the size of the Plank scale) is due to gravitons being able to propagate to extra dimensions. While the fields in the SM are localized on the 4-dimensional manifold, gravitons could escape into extra dimensions thus rendering gravity weak. In such a scenario, gravitational and gauge interactions are unified at the weak scale. The cut-off scale Λ in equation 1.6.1 is of order $10^{2}\,\mathrm{GeV}$ thus

nullifying the fine-tuning problem.

Conversely the fine-tuning problem can be solved by an additional symmetry, supersymmetry. A consequence of supersymmetry is cancellation of Λ^2 terms in quantum corrections to the Higgs mass by an appropriate set of particles. Compare equations 1.6.1 and 1.6.2. The crucial minus sign in Eq. 1.6.1 from the fermion loop raises a possibility to cancel the quadratically divergent terms, provided the couplings are related by

$$|\lambda_f|^2 = 2\lambda_S. \tag{1.6.3}$$

This constraint is automatically satisfied in supersymmetric theories. The couplings are related by $|\lambda_f|^2 = \lambda_S$ and the factor of 2 comes from the number of degrees of freedom of scalar fields.

Both possibilities; large extra dimensions and supersymmetry are not excluded. Experimental limits on the large extra dimensions are stronger than those on supersymmetry. Recent ATLAS publication [35] shows that in the LED model with two extra dimensions, Planck scale less than 7.1 TeV is excluded. This thesis focuses on supersymmetry.

The importance and necessity of a symmetry, which potentially prevents quadratic divergences in radiative corrections, has examples in the SM. Quantum electrodynamics (QED) possess a U(1) gauge symmetry, which prohibits photons from having mass. In the absence of this symmetry, quantum corrections to the photon self-energy would grow quadratically with the cut-off scale. Quadratic terms in radiative corrections induce a shift in the mass, thus gauge symmetry ensures the photon stays massless. On the same hand, the chiral symmetry of fermion fields ensures that radiative corrections to fermion self-energy are proportional to the mass of the fermion. Hence, these can only depend logarithmically on the cut-off scale. Parameters, whose radiative corrections have logarithmic dependence on the cut-off, are not considered to be fine-tuned. This is because the physical value of a parameter is of the same order as the corrections.

1.6.2 Supersymmetry

Supersymmetry (SUSY) is a symmetry which relates bosonic and fermionic degrees of freedom. For every boson in a supersymmetric theory there is a corresponding fermion, and vice versa. The boson and the fermion, which are related by supersymmetry, are called superpartners. They belong to symmetry group representations

called supermultiplets. The members of a supermultiplet must have all quantum numbers the same, except their spin must differ by 1/2. This means that the masses of superpartners and the couplings to other particles must be identical. Phenomenologically that would imply the existence of a scalar superpartner of the electron, called selectron, which would have the same mass and the same electric charge as the electron, making it extremely easy to detect. The reason why there is no such particle can be given in terms of a broken supersymmetry. If SUSY is realized in nature then the superpartners of the known particles must be either much heavier than is currently accessible by particle colliders, or their interactions must be much weaker than the ones in the SM. While technically possible, different couplings of superpartners are not considered seriously, because in that case the whole purpose of SUSY would be ignored. The precise relationship between couplings, which allows the cancellation of quadratic divergences, would be violated and the fine-tuning problem would keep glaring with its disrespect for beauty and simplicity. The only option then is to make superpartners much heavier than the SM particles, but leave coupling constants related as required by supersymmetry. This type of supersymmetry breaking is called 'soft'. Generally, it is thought that the masses of the superpartners can not be larger than a few TeV, otherwise the theory would still be fine-tuned. In a softly broken supersymmetric theory the quadratic divergences cancel exactly, but the next term in the quantum correction to the mass of a scalar boson is logarithmic in the cut-off and proportional to particles' masses:

$$\Delta m_H^2 \propto (m_f^2 - m_S^2) \ln \Lambda. \tag{1.6.4}$$

If masses of the superpartners are too heavy, this correction is also large and leads back to the fine-tuning problem [36].

In Lorenz covariant quantum field theories, supersymmetry is the only possible additional space-time symmetry and it also combines space-time and internal (spin) quantum numbers. Contrary to the Lorentz symmetry of the SM generated by objects which transform as tensors, supersymmetry is generated by objects which belong to the spin representation of the Poincare group. A spinor is the simplest non-trivial representation of the Poincare (and Lorentz) group. In the case of supersymmetry there is an operator Q_a (a is a spinor index), which, when acting on a particle state of spin j, results in a different state that has spin value changed

by 1/2:

$$Q_a|j\rangle = |j \pm 1/2\rangle. \tag{1.6.5}$$

The operator Q_a, being a symmetry generator, commutes with the Hamiltonian,

$$[Q_a, H] = 0, \tag{1.6.6}$$

which means that quantum states in the same supermultiplet have same four-momenta and same interactions. Supersymmetry can also be implemented as differential operators acting on superfields. Superfields are functions of space-time coordinates and, additionally, of fermionic coordinates. In this case, supersymmetry can be though of as extending the notion of space-time to superspace, which has 1 time, 3 space and 4 anti-commuting fermionic coordinates.

The simplest supersymmetric quantum field model is the Wess-Zumino model which is also a fundamental component for building more complex supersymmetric models such as the Minimal Supersymmetric Standard Model (MSSM). The Wess-Zumino model describes a left-chiral supermultiplet of a complex scalar field, ϕ, a left-chiral spinor, χ_a, and a non-propagating auxiliary field, F. The Lagrangian of the model is [36]

$$\mathcal{L}_{WZ} = \partial_\mu \phi^* \partial^\mu \phi + i\chi_{\dot{a}}^\dagger \bar{\sigma}_\mu^{\dot{a}a} \partial^\mu \chi_a + F^* F, \tag{1.6.7}$$

where $\bar{\sigma}_\mu$ is a shorthand notation for the identity and Pauli matrices: $\bar{\sigma}_\mu = (I_2, -\vec{\sigma})$. The scalar field in the Lagrangian has two degrees of freedom (dof) and the spinor field also has two degrees of freedom when it is on-shell. In quantum field theories the quantum fields can also be off-shell and then spinor fields have four dof. To match the number of bosonic and fermionic degrees of freedom, the Wess-Zumino model includes the field F which has two bosonic dof when it is off-shell and zero dof when it is on-shell. The Lagrangian is invariant under the supersymmetry transformations (up to a total derivative)

$$\delta\phi = \epsilon^a \chi_a, \tag{1.6.8}$$

$$\delta\chi_a = -i(\sigma^\nu \epsilon^\dagger)_a \partial_\nu \phi + \epsilon_a F, \tag{1.6.9}$$

$$\delta F = -i\epsilon_{\dot{a}}^\dagger \bar{\sigma}_\nu^{\dot{a}a} \chi_a. \tag{1.6.10}$$

The transformations above can be used with the Noether's theorem to construct

conserved currents, called supercurrents, and consequentially calculate conserved charges, called supercharges, Q_a. The conserved charges are the symmetry generators of SUSY and they can be used to construct the supersymmetry algebra which happens to be

$$\{Q_a, Q_b^\dagger\} = \sigma_{ab}^\mu P_\mu, \tag{1.6.11}$$

$$\{Q_a, Q_b\} = \{Q_a^\dagger, Q_b^\dagger\} = 0, \tag{1.6.12}$$

$$[Q_a, P_\mu] = [Q_a^\dagger, P_\mu] = 0. \tag{1.6.13}$$

where P_μ is the four-momentum operator. It is said that supersymmetry generators are the generators of supertranslations.

1.7 Minimal Supersymmetric Standard Model

The Minimal Supersymmetric Standard Model (MSSM) [37] is the simplest extension of the Standard Model that includes supersymmetry. When the particle content of the SM is known, chiral and gauge supermultiplets containing the particles of the SM and their superpartners can be constructed. The SM particles and their quantum numbers were introduced in Section 1.2, Table 1.1. Due to SUSY being very restrictive, all the quantum numbers within a supermultiplet must be equal, because SUSY transformations do not act on the $SU(3)_c \times SU(2)_L \times U(1)_Y$ structure. This means that there is no way to group any known particles into supermultiplets, hence all superpartners must be completely new particles. Every fermion of the SM belongs to a chiral supermultiplet and have a spin-0 superpartner. SM fermions can not have spin-1 superpartners because spin-1 particles in a renormalizable field theory must belong to the adjoint representations of the gauge groups. Every vector boson of the SM belongs to a vector supermultiplet and has a spin-1/2 superpartner.

With the above conditions imposed on the supersymmetric version of the SM, the particle content of the MSSM is the following. Leptons and quarks have superpartners, called sleptons and squarks, and the convention is to name them by adding a prefix 's' to the corresponding names of leptons and quarks. They are denoted by the same symbol as the corresponding SM particle, but with a tilde. Each squark and slepton must be described by two different complex scalar fields, which are corresponding superpartners of the left- and right-chiral fermions. By convention, the scalar superpartners carry subscripts 'L' or 'R' to indicate which

of the two chiral states of a fermion they are superpartners to. For example, a left-chiral electron e_L together with its neutrino $\nu_{e\,L}$, both belonging to an $SU(2)_L$ doublet, have superpartners $\tilde{e}_L$ and $\tilde{\nu}_{e\,L}$:

$$\begin{pmatrix} \nu_{eL} \\ e_L \end{pmatrix} \text{ have superpartners } \begin{pmatrix} \tilde{\nu}_{eL} \\ \tilde{e}_L \end{pmatrix}. \tag{1.7.1}$$

Gauge bosons have spin-1/2 fermion superpartners, called gauginos. Gluons, g, have superpartners called gluinos, $\tilde{g}$, which belong to the adjoint representation of the $SU(3)$. The $U(1)_Y$ gauge field B^μ has a superpartner called bino, $\tilde{B}^\mu$, and $SU(2)_L$ gauge bosons $W^{a\mu}$ have superpartners called winos, $\tilde{W}^{a\mu}$. As in the SM, the third component of the $\tilde{W}^{a\mu}$ field mix with the $\tilde{B}^\mu$ field and the mass eigenstates are called zino, superpartner of the Z boson, and photino, superpartner of the photon. The mixing of the first two components of the $\tilde{W}^{a\mu}$ results in the superpartners of the $W^\pm$ bosons. Charged gauginos are also called charginos and electrically neutral gauginos are also called neutralinos.

The Higgs sector of the MSSM consists of the SM Higgs doublet and, additionally, another Higgs doublet of the opposite hypercharge, and their superpartners. The second $SU(2)$ Higgs doublet is introduced in order to make the theory renormalizable by canceling gauge anomalies which in the SM are already canceled automatically. The condition for the gauge anomaly cancellation is $\mathrm{Tr}[T_3^2 Y] = 0$ where the trace runs over all fermionic degrees of freedom. Another reason for the second doublet is that the Higgs potential in the MSSM must be a holomorphic function of the fields and therefore the down-type fermions can not be coupled to the complex conjugate of one Higgs doublet. The Higgs supermultiplets belong to chiral supermultiplets and the spin-1/2 superpartners are called higgsinos. The charged higgsinos are also called charginos and neutral higgsinos are called neutralinos as in the case of gauge boson superpartners. The two Higgs doublets are denoted by H_u and H_d carrying hypercharges $Y = +1$ and $Y = -1$, respectively.

Finally, the Higgs fields of the MSSM has the following $SU(2)$ structure:

$$H_u = \begin{pmatrix} H_u^+ \\ H_u^0 \end{pmatrix}, \tilde{H}_u = \begin{pmatrix} \tilde{H}_u^+ \\ \tilde{H}_u^0 \end{pmatrix}, \tag{1.7.2}$$

$$H_d = \begin{pmatrix} H_d^0 \\ H_d^- \end{pmatrix}, \tilde{H}_d = \begin{pmatrix} \tilde{H}_d^0 \\ \tilde{H}_d^- \end{pmatrix}. \tag{1.7.3}$$

The particle content of the MSSM is summarized in Tables 1.2 and 1.3. The right-chiral fermions are labeled by their charge-conjugate states and therefore have opposite hypercharge values than the states listed in Table 1.1.

Table 1.2: List of chiral supermultiplets in the MSSM [31].

Names		spin 0	spin 1/2	$SU(3)_c$, $SU(2)_L$, $U(1)_Y$
squarks, quarks	Q	$(\tilde{u}_L, \tilde{d}_L)$	(u_L, d_L)	(**3**, **2**, 1/3)
(×3 families)	$\bar{u}$	$\tilde{\bar{u}}_L = \tilde{u}_R^\dagger$	$\bar{u}_L = u_R^c$	($\bar{\mathbf{3}}$, **1**, -4/3)
	$\bar{d}$	$\tilde{\bar{d}}_L = \tilde{d}_R^\dagger$	$\bar{d}_L = d_R^c$	($\bar{\mathbf{3}}$, **1**, 2/3)
sleptons, leptons	L	$(\tilde{\nu}_{eL}, \tilde{e}_L)$	(ν_{eL}, e_L)	(**1**, **2**, -1)
(×3 families)	$\bar{e}$	$\tilde{\bar{e}}_L = \tilde{e}_R^\dagger$	$\bar{e}_L = e_R^c$	(**1**, **1**, 2)
Higgs, Higgsinos	H_u	(H_u^+, H_u^0)	$(\tilde{H}_u^+, \tilde{H}_u^0)$	(**1**, **2**, 1)
	H_d	(H_d^0, H_d^-)	$(\tilde{H}_d^0, \tilde{H}_d^-)$	(**1**, **2**, -1)

Table 1.3: List of vector supermultiplets in the MSSM [31].

Names	spin 1/2	spin 1	$SU(3)_c$, $SU(2)_L$, $U(1)_Y$
gluino, gluon	$\tilde{g}$	g	(**8**, **1**, 0)
winos, W bosons	$\tilde{W^{a\mu}}$	$W^{a\mu}$	(**1**, **3**, 0)
bino, B boson	$\tilde{B}$	B	(**1**, **1**, 0)

1.7.1 Soft SUSY Breaking

If supersymmetry were not broken, the superpartners of the known particles would be very easy to detected, because they would have the same coupling strengths and masses, and their interactions would be very similar to those of the SM particles. Instead, supersymmetry must be broken, which brings much arbitrariness in the model. The nature of supersymmetry breaking is unclear but effective Lagrangians containing explicit SUSY breaking terms and having the form

$$\mathcal{L} = \mathcal{L}_{SUSY} + \mathcal{L}_{soft} \tag{1.7.4}$$

are of great importance [38]. Here the first term is supersymmetry covariant and has the particle content described above. The second term is called the soft supersymmetry breaking term. This term includes only parameters with positive mass dimension which are super-renormalizable. Super-renormalizable terms do not introduce divergences in coupling constants and masses. This structure of the Lagrangian ensures that quadratic divergences in radiative corrections cancel because they are multiplied by the $(\lambda_S - |\lambda_f|^2)$ term and this is ensured to be zero by the $\mathcal{L}_{SUSY}$ part. Also, the soft supersymmetry breaking term can only result in logarithmic corrections of the form $m_{soft}^2 \log(\Lambda/m_{soft})$ where m_{soft} is a parameter corresponding to the highest mass scale in $\mathcal{L}_{soft}$. This indicates that mass splitting between the SM particles and their superpartners can not be too large, otherwise the solution to the hierarchy problem would be lost.

1.7.2 MSSM Higgs Sector

In the MSSM there are two complex $SU(2)_L$ Higgs doublets of opposite hypercharge which have eight degrees of freedom in total. When the electroweak symmetry is spontaneously broken similarly to the SM, three degrees of freedom become the longitudinal polarization states of the $W^{\pm}$ and Z bosons. Assuming that $\mathcal{CP}$ symmetry is conserved, the remaining five degrees of freedom turn out to be the physical states of five Higgs bosons. The linear combination of H_d^0 and H_u^0 results in two neutral Higgs bosons: the light and heavy $\mathcal{CP}$-even neutral scalars h and H. In addition to those, the three remaining Higgs bosons are the $\mathcal{CP}$-odd neutral scalar A and two charged scalars $H^{\pm}$.

The properties of the MSSM Higgs sector at tree-level depend only on two non-SM parameters that can be chosen to be the mass of the $\mathcal{CP}$-odd Higgs boson,

m_A, and the ratio of the vacuum expectation values of the two Higgs doublets:

$$\tan\beta = \frac{v_u}{v_d} \tag{1.7.5}$$

$$v_u^2 + v_d^2 = v^2 \tag{1.7.6}$$

At leading order, m_h is bound to be less than the mass of the Z boson. When higher order corrections are included, the upper bound increases to a maximum value of $\simeq 135\,\text{GeV}$, in agreement with the measured mass of the observed Higgs boson if it were identified with the h boson. The mass of the charged Higgs bosons is given, at tree-level, in terms of m_A and the $W^\pm$ mass, m_W, by the relation $(m_{H^\pm}^{\text{tree}})^2 = m_A^2 + m_W^2$.

Beyond the tree-level, additional parameters of the MSSM, which come from supersymmetry breaking and therefore are unknown, affect the phenomenology of the Higgs sector. The main radiative corrections to the Higgs boson masses arise from the top/stop sector and, for large values of $\tan\beta$, also from the bottom/sbottom and tau/stau sectors. Mass parameters of the third generation squarks in the basis of the current eigenstates are usually taken to be equal and they set the scale of the SUSY breaking:

$$m_{\text{SUSY}} \equiv m_{\tilde{t}_L} = m_{\tilde{t}_R} = m_{\tilde{b}_L} = m_{\tilde{b}_R} \tag{1.7.7}$$

With this identification, the most important parameters for the radiative corrections in the Higgs sector are the top-quark mass, m_t, SUSY breaking scale, m_{SUSY}, and mass mixing parameters in stop and sbottom sectors. The dominant components of radiative corrections grow like the fourth power of m_t, quadratically with the stop mixing parameter and logarithmically with m_{SUSY}. The stop mixing parameter represents the amount of mixing between L- and R-chiral stop-squark current eigenstates. Larger mixing corresponds to larger mismatch between the current and mass eigenstates of stop-squarks. Finally, parameters of the first and second generation squarks and sleptons have much smaller impact on the MSSM Higgs sector.

1.8 MSSM Benchmark Scenarios

Supersymmetry breaking mechanism, and in particular soft supersymmetry breaking, introduces many free parameters, the values of which are not predicted by

the model. Scans of all the parameters in physics analyses and theoretical calculations is impractical and therefore a few sets of fixed parameter values, called benchmark scenarios, are chosen to represent certain features of the MSSM Higgs phenomenology [39].

Observables in the MSSM Higgs sector at leading order are fully determined by only two non-SM parameters: $\tan\beta$ and m_A. On the other hand, radiative corrections depend on SUSY breaking parameters whose values are fixed in benchmark scenarios. The results of search analyses are usually interpreted in terms of specific benchmark scenarios while scanning the two-dimensional ($\tan\beta$,m_A) space in order to set limits on the allowed values. Every benchmark scenario results in a specific phenomenology of the MSSM Higgs sector which will be described in more detail below.

Additionally, there are also experimental and theoretical constraints on SUSY breaking parameters which are relevant to benchmark scenarios. In particular, one of the MSSM Higgs bosons must be identified with the observed 125 GeV particle at the LHC. In most benchmark scenarios the observed resonance is interpreted as the light Higgs boson, h, with $m_h \simeq 125\,\text{GeV}$ and therefore the allowed values of SUSY parameters must be such as to produce the measured mass of the light Higgs boson. Also, the decay and production rates of the light Higgs boson in the MSSM must be compatible with the experimental measurements which to this day indicate that the 125 GeV particle behaves like the SM Higgs boson [40].

There are some limits set on the parameters from direct searches for SUSY particles and these limits can be taken into account when calculating properties of the Higgs bosons. Recent searches for stop and sbottom squarks set limits on their masses up to $\approx 1\,\text{TeV}$ [41, 42], depending on a model. For this reason the SUSY breaking scale, m_{SUSY}, is usually set to 1 TeV or above.

There are many different benchmark scenarios, which exhibit distinct and interesting phenomenology of the MSSM Higgs sector. However, many of those scenarios became obsolete after the discovery of the SM-like Higgs boson at the LHC, as they are incompatible with interpreting it as the light MSSM Higgs boson. For example, *no-mixing* scenario, which assumes no mixing in the stop sector, or *gluophobic Higgs* scenario, which exhibit large suppression of ggh coupling, are incompatible with $m_h \simeq 125\,\text{GeV}$. On the other hand, the available parameter space is still large enough to accommodate the $m_h \simeq 125\,\text{GeV}$ particle and there are a handful of relevant scenarios that can be used to interpret LHC data.

$m_{\mathrm{h}}^{\mathrm{max}}$ Scenario

The $m_{\mathrm{h}}^{\mathrm{max}}$ scenario was originally defined in such a way as to maximize the mass of the light $\mathcal{CP}$-even Higgs boson at large values of m_A for a fixed value of $\tan\beta$. The mass of the light Higgs boson is most sensitive to the stop mixing parameter and the maximum mass value can be achieved by tuning this parameter. However, due to the definition of this scenario, the mass of the light Higgs boson is compatible with $m_h \simeq 125\,\mathrm{GeV}$ only in a relatively small region of the parameter space, in particular, at rather small values of $\tan\beta$.

$m_{\mathrm{h}}^{\mathrm{mod}\pm}$ Scenario

After the discovery of the 125 GeV resonance, a couple of modified scenarios, called $m_{\mathrm{h}}^{\mathrm{mod}-}$ and $m_{\mathrm{h}}^{\mathrm{mod}+}$, were introduced. Compared to the $m_{\mathrm{h}}^{\mathrm{max}}$, the modified scenarios $m_{\mathrm{h}}^{\mathrm{mod}\pm}$ have smaller amount of mixing in the stop sector, which results in a slightly lower mass of the light Higgs boson. The lower absolute value of the stop mixing parameter in these scenarios makes the mass of the light Higgs boson compatible with the 125 GeV resonance in a large region of the $(m_A, \tan\beta)$ parameter space. The difference between the two $m_{\mathrm{h}}^{\mathrm{mod}\pm}$ scenarios is the relative sign and absolute value of the off-diagonal stop mass matrix elements. In terms of exclusion regions the difference in the relative sign does not have a significant effect.

Branching ratios of the heavy neutral Higgs bosons in the most sensitive decay modes to $\tau^+\tau^-$ and $b\bar{b}$ at high values of $\tan\beta$ are significantly affected by other decay modes at moderate and low values of $\tan\beta$. At lower values of $\tan\beta$, the decay modes to charginos and neutralinos may reach branching fractions of 70% leading to a corresponding decrease of the branching fractions into third generation leptons. In searches for the heavy Higgs bosons in the di-tau decay mode, this makes it more difficult to exclude parameters at moderate and low values of $\tan\beta$.

hMSSM Scenario

A different approach is pursued in the hMSSM scenario. The measured value of the light Higgs boson mass, $m_h \approx 125\,\mathrm{GeV}$, is used to fix the values of dominant radiative corrections. With this approach, Higgs sector can again be described by only two parameters, $\tan\beta$ and m_A. To a good approximation this is true even when the full set of radiative corrections at two-loop order is included. It was shown in [43] that subleading radiative corrections have little impact on the mass

of the heavy $\mathcal{CP}$-even Higgs boson, m_H, and the neutral $\mathcal{CP}$-even Higgs mixing angle, α, when SUSY breaking parameters are varied in a reasonable range.

The cited paper used the following parametrization of the $\mathcal{CP}$-even Higgs mass matrix, in the (H_d, H_u) basis:

$$m^2_{\text{SUSY}} = m_Z^2 \begin{pmatrix} c_\beta^2 & -s_\beta c_\beta \\ -s_\beta c_\beta & s_\beta^2 \end{pmatrix} + m_A^2 \begin{pmatrix} s_\beta^2 & -s_\beta c_\beta \\ -s_\beta c_\beta & c_\beta^2 \end{pmatrix} + \begin{pmatrix} \Delta M_{11}^2 & \Delta M_{12}^2 \\ \Delta M_{21}^2 & \Delta M_{22}^2 \end{pmatrix} \tag{1.8.1}$$

where the shorthand notation $s_\beta \equiv \sin\beta$ etc. has been used. The radiative corrections have been introduced by a general 2×2 matrix ΔM_{ij}^2. The ΔM_{22}^2 entry involves dominant top/stop sector corrections. To a good approximation $\Delta M_{22}^2 \gg \Delta M_{11}^2, \Delta M_{12}^2$. When the subleading radiative corrections are set to zero, the ΔM_{22}^2 term can be expressed in terms of m_h. Then, the mass of the heavy neutral $\mathcal{CP}$-even Higgs boson and the mixing angle α in the hMSSM reads

$$m_H^2 = \frac{(m_A^2 + m_Z^2 - m_h^2)(m_Z^2 c_\beta^2 + m_A^2 s_\beta^2) - m_A^2 m_Z^2 c_{2\beta}^2}{m_Z^2 c_\beta^2 + m_A^2 s_\beta^2 - m_h^2}, \tag{1.8.2}$$

$$\alpha = -\arctan\left(\frac{(m_Z^2 + m_A^2) c_\beta s_\beta}{m_Z^2 c_\beta^2 + m_A^2 s_\beta^2 - m_h^2}\right). \tag{1.8.3}$$

For $m_A = 300\,\text{GeV}$ the relative differences between the hMSSM parametrization of m_H and the exact value with full second-order radiative corrections was shown to be smaller than the decay width Γ_H. The relative differences for α do not exceed ≈ 0.025 at low values of $\tan\beta$, while at high $\tan\beta$, in some rare situations, the differences can reach ≈ 0.05.

Heavy Higgs Scenario

In principle, a more exotic interpretation of the observed 125 GeV particle can be made in terms of the heavy $\mathcal{CP}$-even Higgs boson of the MSSM. In this case all Higgs bosons would be light and the light $\mathcal{CP}$-even Higgs boson would have heavily suppressed couplings to gauge bosons. This kinematic domain is not explored in this thesis.

1.9 Searches for MSSM Higgs Bosons

Various searches have been performed by the ATLAS and CMS collaborations in Run 1 and Run 2 of the LHC to cover the Higgs sector of the MSSM. ATLAS searches are neatly summarized in the $m_A - \tan\beta$ parameter space of the hMSSM scenario shown in Fig. 1.6. Due to the enhancement of Higgs boson couplings to down-type fermions at high values of $\tan\beta$, production and decay modes of the Higgs bosons depend strongly on the $\tan\beta$ parameter, and consequently different search channels are sensitive to different regions of the $m_A - \tan\beta$ parameter space.

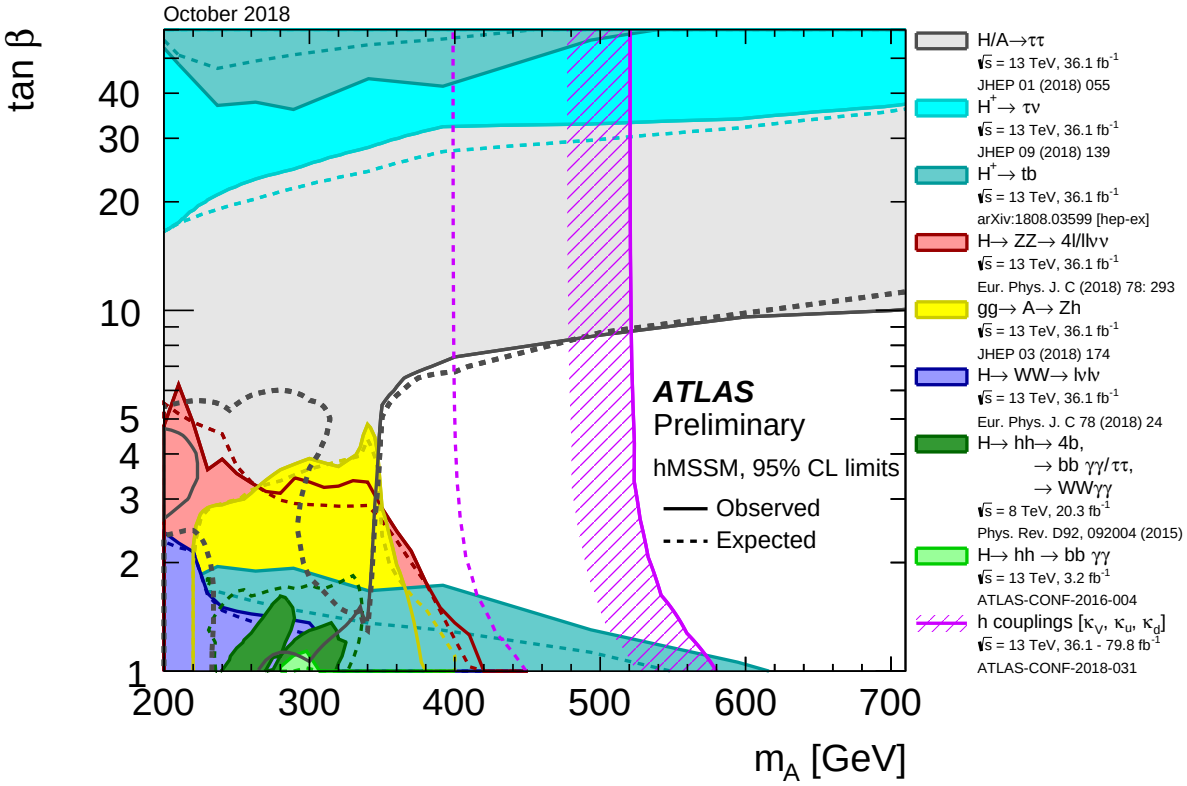

Figure 1.6: Summary plot of ATLAS searches for additional Higgs bosons interpreted in the hMSSM parameter space [44].

The most important production mode of the H/A Higgs bosons is gluon-gluon fusion. Additionally, at high values of $\tan\beta$ the b-associated production mode has a significant cross section. The tree-level Feynman diagrams for the two production modes are shown in Fig. 1.7. A production mode which have a b-quark in the initial state is treated in the five-flavor scheme [45] of parton distribution

functions. This scheme allows for a non-zero PDF of the b-quark but sets its mass to zero.

Also, searches involving gauge bosons in the final states benefit from vector-boson-fusion production mode.

Charged Higgs bosons are mostly produced due to interactions with a top quark, as shown in Fig. 1.8. Charged Higgs bosons with lower masses are produced in top quark decays, while those with higher masses are produced in association with non-resonant or single-resonant top quarks.

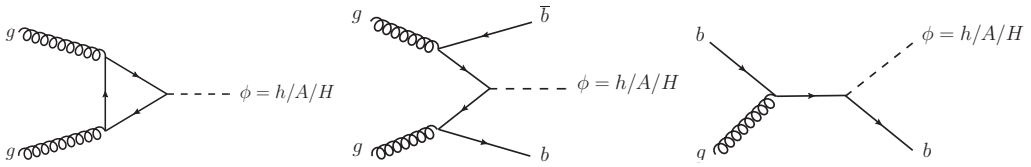

Figure 1.7: Leading-order Feynman diagrams for the production of neutral Higgs bosons in pp collisions. The (left) gluon-gluon fusion dominates at low and moderate values of $\tan\beta$, while b-associated production mode in (middle) four-flavor and (right) five-flavor schemes become significant at high values of $\tan\beta$ [2].

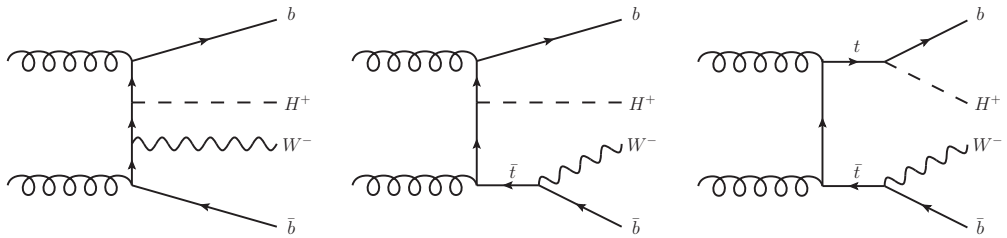

Figure 1.8: Leading-order Feynman diagrams for the production of charged Higgs bosons in pp collisions. The (left) non-resonant and (middle) single-resonant top-quark productions dominate at large H^+ masses, while (right) double-resonant top-quark production dominates at low H^+ masses. The interference between these three main diagrams becomes most relevant in the intermediate mass region [46].

The searches for neutral Higgs bosons H and A use decay channels to gauge bosons, third generation fermions and the light Higgs boson. The $H/A \to \tau\tau$ analysis [2], which includes the work described in this thesis, is sensitive at high $\tan\beta$ region of the hMSSM parameter space due to the enhanced couplings. For the same reason, the $H^+ \to \tau\nu$ [46] and $H^+ \to tb$ [47] analyses are sensitive at high $\tan\beta$ region. Additionally, the $H^+ \to tb$ decay channel is sensitive at low $\tan\beta$ region due to the naturally large Higgs and top-quark coupling. Higgs boson

decay channels $H \to ZZ/WW$ [48, 49] are sensitive at low $\tan\beta$ region where the branching ratios are significantly large. The decay of the heavy neutral $\mathcal{CP}$-even Higgs boson into a pair of light Higgs bosons [50] is sensitive at low $\tan\beta$ and in the kinematically allowed region where the mass of the heavy boson is above the threshold for a light Higgs boson pair production and below the threshold for a top-pair production. The decay channel $A \to Zh$ [51] is significant only at A masses lower than the threshold of the top quark pair because above that threshold the A boson preferably decays into a pair of top quarks.

A fit to the measured SM Higgs boson couplings was performed to constrain modifications to Higgs coupling constants arising from radiative corrections in the MSSM. In this case m_A values below $\sim 530\,\text{GeV}$ are excluded for all values of $\tan\beta$ at 95% CL [40].

Similar searches to the ones mentioned above and a few other searches have been performed by the CMS collaboration. Most of these analyses exploit Run 1 data while only a few analyses with Run 2 data have been published when this thesis was being written. Searches for a heavy scalar boson decaying into a pair of Standard Model Higgs bosons, h, and for a heavy pseudo-scalar boson decaying into a pair of Z and h bosons are published in [52]. Additionally, a search for a pseudo-scalar boson decaying into a pair of Z and h bosons but in a different final state is presented in [53]. A similar analysis to the one presented in this thesis, namely a search for a neutral heavy scalar boson decaying into a pair of tau leptons, was also published by the CMS collaboration in [54]. Searches for a heavy Higgs boson decaying into a pair of b-quarks or a pair of muons have been published in [55] and [56], respectively. Searches for charged Higgs bosons in the production mode through the interaction with top-quarks, and in the vector boson fusion production mode have been published in [57] and [58].

Chapter 2

ATLAS Experiment and the Large Hadron Collider

ATLAS experiment [59] at the European Organization for Nuclear Research (CERN) is carried out by a collaboration of over 3000 physicists, technicians, engineers and administrative staff from 181 institutions around the world. The experiment features the ATLAS detector which is a general-purpose machine used for particle physics research. The detector is designed to detect, reconstruct and identify electrons, muons, taus, and other physics objects, such as jets and missing transverse energy. The particles propagating through the detector are produced in proton-proton collisions provided by the Large Hadron Collider. The members of the experiment are involved in detector development, data collection and data analysis. According to the CERN Document Server [60], the ATLAS collaboration has published 816 papers, 941 conference notes and 2020 PhD theses.

2.1 Large Hadron Collider

The Large Hadron Collider (LHC) at CERN is the largest and most powerful circular particle accelerator and particle collider in the world with the designed center-of-mass (CoM) energy of 14 teraelectronvolts (TeV) for proton-proton collisions. It was proposed in 1984 [61] while another major particle accelerator, the Superconducting Super Collider (SSC) [62] in the USA, Texas, was already in the very early stages of construction. The SSC was designed to provide proton-proton collisions at a center-of-mass energy of 40 TeV, about 3 times more energetic than those of the LHC, but it was canceled in 1993 due to budget problems. The LHC is the current

world record holder for the most energetic particle collisions at a center-of-mass energy of 13 TeV (6.5 TeV per beam) and surpasses the previous record holder, the Tevatron [63] collider at Fermilab in the USA, Illinois, which was operating at a CoM energy of 1.96 TeV. The LHC was built between 1998 and 2008 near Geneva city, Switzerland, in a tunnel ~ 100 m deep underground and crossing the France-Switzerland borders. The tunnel had previously been used for the Large Electron-Positron (LEP) collider [64] which had to be scrapped in 2001 to allow for the installation of the LHC.

Particles at the LHC are accelerated in a storage ring comprising two adjacent parallel beam-pipes and then they can be circulated for many hours with constant kinetic energy. The beam-pipes are 27 km in circumference and they cross each other in four intersection points. The particles propagate in the beam-pipes in opposite directions and collide in the intersection points.

The Large Hadron Collider [65] is a synchrotron type accelerator, a design which allows beam bending, beam focusing and particle acceleration with different components of the machine. In a synchrotron the accelerating electric and bending magnetic fields are synchronized with the increasing energy of the particles. The LHC is composed of 1232 superconducting dipole magnets which keep the particle beams in their circular paths. An additional 392 quadrupole magnets keep the beams focused, with insertion quadrupole magnets closer to the interaction points for more intense focusing to increase the chance of collision. Magnets of higher multipole order are used to correct small imperfections in the magnetic field geometry. The total number of magnets in the LHC is 9593. The superconducting magnets require 96 tonnes of superfluid helium-4 to keep them at the operating temperature of 1.9 K. When the energy of the protons is increased from their injection energy of 450 GeV to the highest energy of 6.5 TeV, the magnetic field generated by the dipole magnets is increased from 0.54 to 7.7 teslas (T). Eight radio-frequency cavities per beam are used to deliver energy to protons during acceleration. The cavities each deliver 2 MV, or an accelerating field of 5 MV/m, at the frequency of 400 MHz. When charged particles are subject to acceleration perpendicular to their velocity, they radiate energy, an effect called synchrotron radiation. For this and other effects, radio-frequency cavities are also used to restore energy losses and keep the kinetic energy of the particles constant.

Before particles are injected into the LHC storage ring, they are accelerated to the injection energy in subsequent systems, shown in Fig. 2.1. First, hydrogen atoms are released from a gas storage tank into an ionizing chamber where electrons

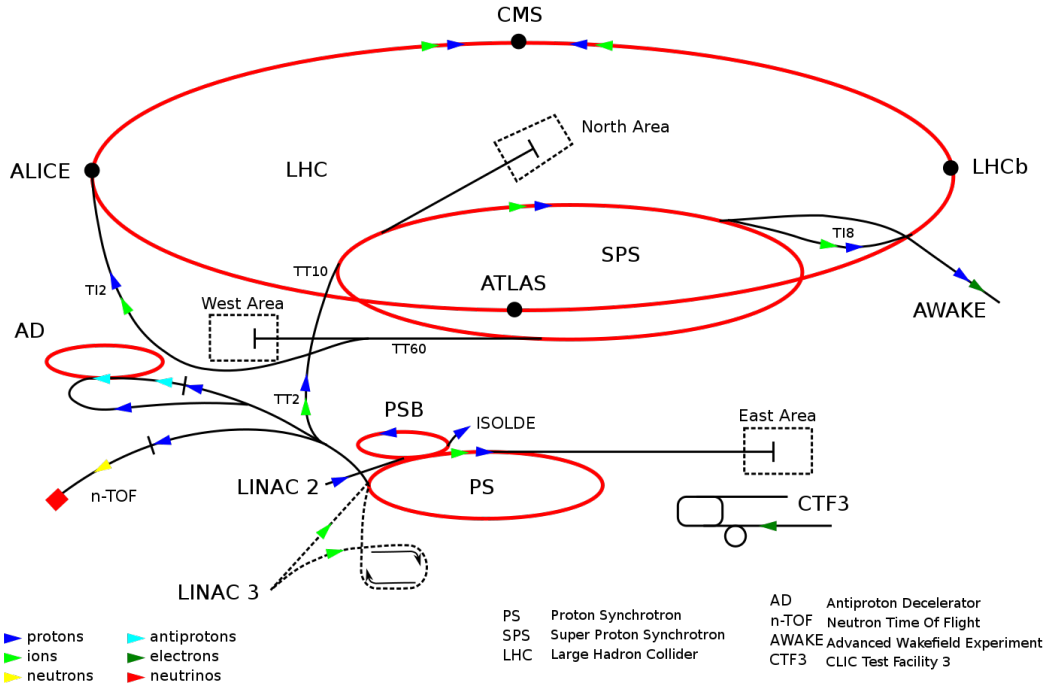

Figure 2.1: CERN accelerator complex serving the LHC. The path of protons starts at LINAC 2, travel through PSB, PS and SPS, and finally reach the LHC [66].

are stripped off of the atoms and hydrogen ions, i.e. single protons, are produced. The protons are accelerated in the linear particle accelerator LINAC 2 to the energy of 50 MeV and injected into the Proton Synchrotron Booster (PSB). There, the protons are accelerated to 1.4 GeV and injected into the Proton Synchrotron (PS) where they reach the energy of 26 GeV. Finally, the protons are injected into the Super Proton Synchrotron (SPS) where their energy is increased to 450 GeV before they are at last injected into the LHC storage ring.

The four largest experiments at the LHC are ATLAS, CMS, LHCb and Alice, each located at one of the four interaction points. ATLAS, which is described in detail in section 2.2, is a general-purpose detector, similarly to the CMS (Compact Muon Solenoid) [67]. On the other hand, LHCb (Large Hadron Collider beauty) [68] is mainly focused on the study of hadrons which contain b-quarks or c-quarks, and ALICE (A Large Ion Collider Experiment) [69] is studying quark-gluon plasma. For the study of quark-gluon plasma, the LHC performs special runs with lead-lead, proton-lead or xenon-xenon collisions.

LHC Operation

The LHC was switched on in 2008 and the first high energy collisions at a CoM energy of 7 TeV were produced in 2010 starting the first period of operation called Run 1. The LHC increased the CoM energy to 8 TeV in 2012 and ran until 2013 when it was temporarily switched off for 2 years, a period called Long Shutdown 1, to carry out some major upgrades for the accelerator and detectors. The collider was switched on again in 2015 for the second period of operation, Run 2, and with increased CoM energy of 13 TeV. Run 2 ended in 2018 after a very successful run and entered the Long Shutdown 2 period to carry out further major upgrades. After Run 2 the LINAC 2 was switched off and will not be restarted; instead, a new linear accelerator LINAC 4 will take over the role of the first step of proton acceleration. The LINAC 4 will be capable of producing higher intensity beams and will be connected to the PSB during Long Shutdown 2.

Proton beams circulating around the storage ring are not continuous but discrete, arranged into bunches. By design, it is possible to inject up to 2808 bunches with some 1.2×10^{11} protons per bunch. The interactions between bunches take place at time intervals of 25 ns (so called 25 ns bunch spacing) and thus result in bunch collision rate of 40 MHz. In Run 1, the LHC collided protons with 50 ns bunch spacing. It takes less than 90 μs for a proton with ultra-relativistic energy to revolve once around the storage ring and therefore the revolution frequency is 11245 Hz. The designed luminosity is $1 \times 10^{34}\,\mathrm{cm}^{-2}\mathrm{s}^{-1}$ which was reached in 2016, but already in 2017 twice this value was achieved.

To deal with huge amounts of data produced in the LHC experiments, the Worldwide LHC Computing Grid (WLCG) [70], a grid-based computer network infrastructure, was built.

2.2 ATLAS Detector

The ATLAS[1] detector [59], shown in Fig. 2.2, consists of an inner detector for tracking charged particles, sampling electromagnetic and hadronic calorimeters for energy measurements, and a muon spectrometer for muon tracking. The inner detector is surrounded by a thin superconducting solenoid providing an axial magnetic field for measurements of charged-particle momenta. The muon spectrometer also includes three air-core toroid magnets. The whole system of detectors covers

[1] A Toroidal LHC Apparatus

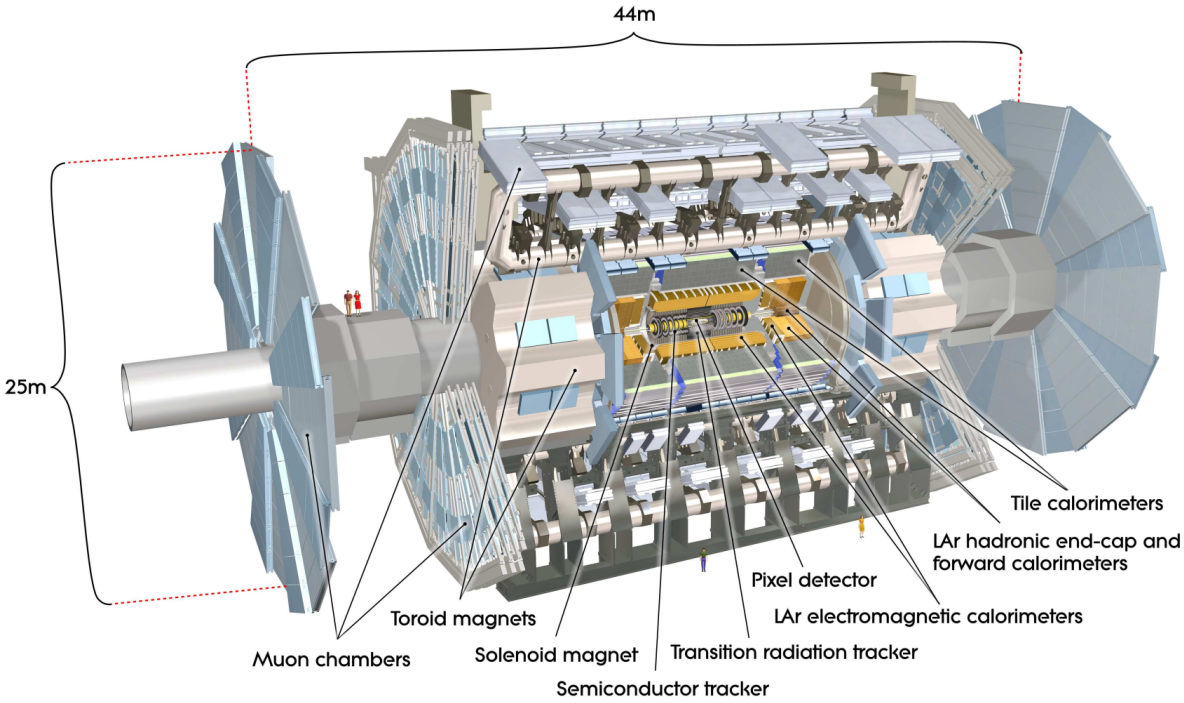

Figure 2.2: ATLAS detector in its entirety. The pixel detector, SCT tracker and TRT tracker make the inner detector which is surrounded by the solenoid magnet. Muon detectors and toroid magnets make the muon spectrometer. The entire calorimeter comprise tile and liquid argon calorimeters [59].

nearly the entire solid angle around the collision point. The detector is the largest apparatus in volume ever built for particle colliders. It is 44 m long and 25 m in diameter, and weights 7000 tonnes.

2.2.1 ATLAS Coordinate System

ATLAS uses a right-handed Cartesian coordinate system (x, y, z) to describe the detector and particles propagating through it. The origin of the coordinate system is identified with the nominal interaction point (in practice, the beam is offset by about 1 mm). The z axis is set along the beam line, the x axis is defined as pointing towards the center of the LHC ring and the y axis pointing upward. The side-A of the detector is defined as that with positive z coordinates and the side-C is that with negative z. A cylindrical coordinate system (r, ϕ, z) is used in complementarity to the Cartesian coordinates. The transverse plane to the z axis is parametrized with the azimuthal angle $\phi = \arctan(y/x)$ and the distance from the beam is measured

in $r = \sqrt{x^2 + y^2}$. Additionally, polar angle $\theta = \arctan(r/z)$ is the angle from the beam and it is used to define pseudorapidity as $\eta = \ln \tan(\theta/2)$. This variable is the limit of rapidity for highly relativistic particles. When the mass of an objects can not be neglected, rapidity $y = 1/2 \ln [(E + p_z)/(E - p_z)]$ is used. Rapidity is an additive variable under boosts in the z direction. It boosts the laboratory frame of reference to a frame of reference in which the particle moves only in the transverse direction. The distance ΔR in azimuthal angle and pseudorapidity space is defined as $\Delta R = \sqrt{\Delta\phi^2 + \Delta\eta^2}$.

Charged particles propagating in a magnetic field have their trajectories bent in the plane perpendicular to the magnetic field. From the curvature of the trajectory transverse momentum, denoted by p_T, can be measured.

2.2.2 Inner Detector

The inner detector (ID) [71] is a compact cylindrically symmetric tracker used to detect charged particles and reconstruct their trajectories. It is composed of three different technology subdetectors: a silicon pixel detector, a silicon microstrip detector and a transition radiation tracker. Overall, the inner detector covers a pseudorapidity range of $|\eta| < 2.5$ and provides particle momentum, electric charge and vertex position measurements. Nominal momentum measurements are for particles with $p_T > 0.5\,\text{GeV}$, measured with a resolution of $\sigma_{p_T}/p_T = 0.05\% p_T \oplus 1\%$. High tracking precision allows measurements of the positions of primary and secondary vertices which are used for b-jet and τ-lepton tagging. The inner detector is immersed in a 2 T axial magnetic field generated by the superconducting solenoid magnet.

The computer generated image of the cut-away view of the ID is shown in Fig. 2.3. The schematic overview of a quarter-section of the ID showing the positions of sensor elements, described in more detail below, is shown in Fig. 2.4.

Silicon Pixel Detector

The silicon pixel detector has the shape of a cylinder 1.4 m long and 0.5 m in diameter. It consists of four barrel layers wrapping concentrically around the beam pipe and three disks on each side in the forward regions. The three outermost barrel layers are located at 50.5 mm, 88.5 mm and 122.5 mm from the center of the beam pipe. The fourth innermost layer, Insertable B-Layer (IBL) [72], is located at 33.25 mm. It was installed during Long Shutdown 1 before Run 2 of the LHC.

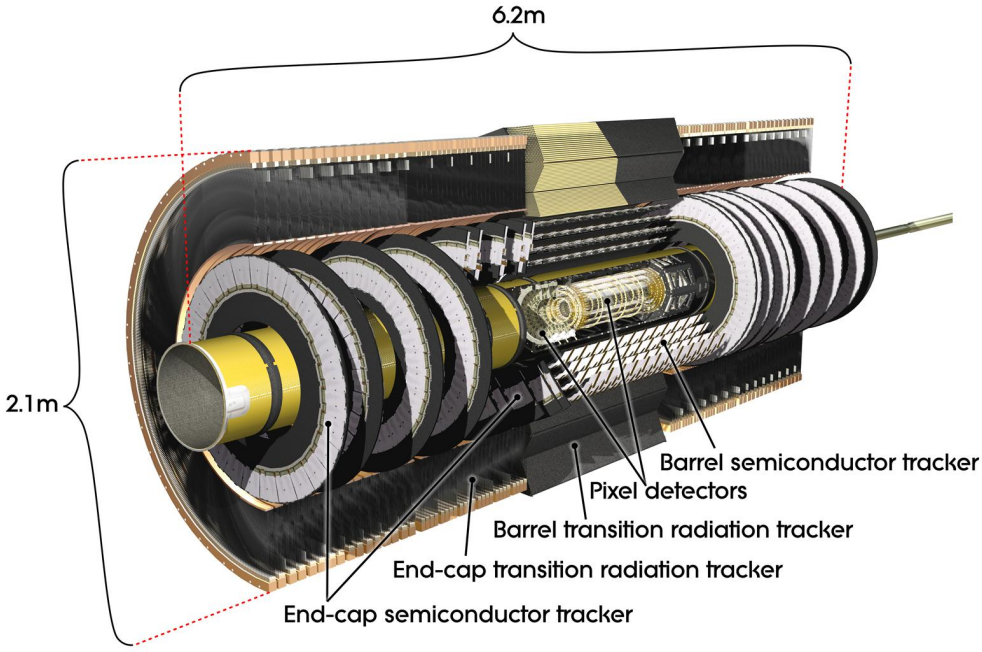

Figure 2.3: Cut-away view of the ATLAS inner detector [59].

For the installation of the IBL, the old beam-pipe within the length of the inner detector had to be replaced with a new one that has a smaller outer radius of 30 mm.

The silicon pixel detector (excluding the IBL) consists of 1744 silicon wafer modules. Each module has 16 front-end chips and one module control chip. Front-end chips are the main heat source dissipating 15 kW into the detector volume. One silicon module has 46080 pixels of size 50×400 microns in $r - \phi \times z$ coordinates. That sums up to the total of about 80.4 million readout channels and the IBL provides an additional 12 million channels.

The silicon pixel detector covers the pseudorapidity range of $|\eta| < 2.5$ and provides up to four measurement points of a charged particle. For the pixels in the barrel layers high intrinsic accuracies of 10 μm in $r - \phi$ coordinates and 115 μm in z are achieved. In the end-cap discs the intrinsic accuracies are 10 μm in $r - \phi$ and 115 μm in r. These large number of high granularity pixels with high intrinsic accuracy are exploited for primary and secondary vertex position measurements.

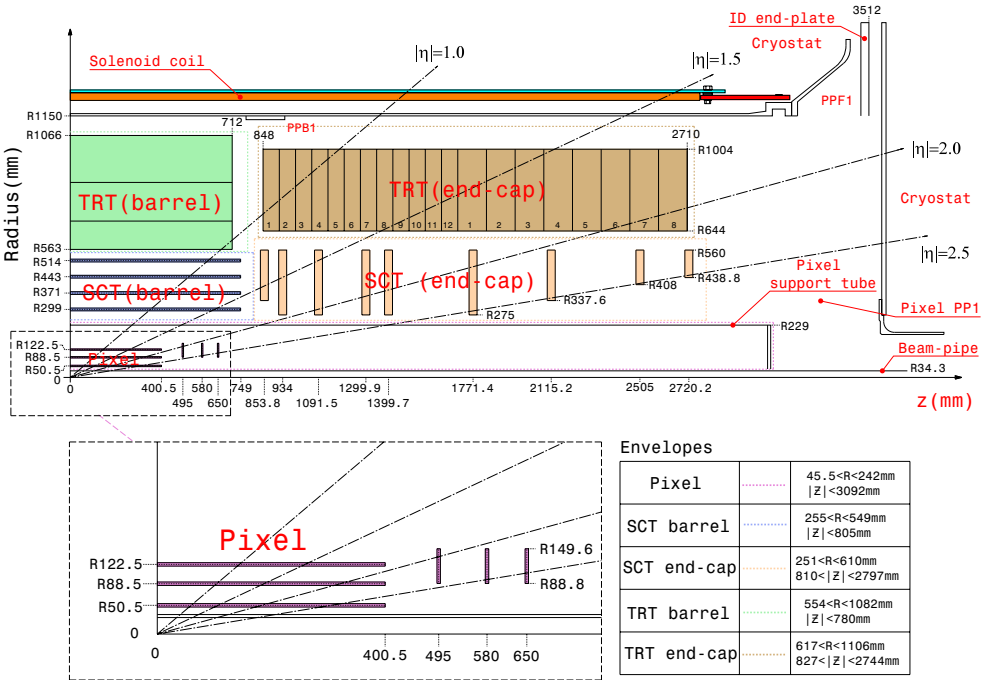

Figure 2.4: Schematic view of the quarter-section of the ATLAS inner detector [59]. The Insertable B-layer is not shown but fits inside the pixel detector; the beam-pipe radius is reduced to 30 mm.

Semiconductor Tracker

The semiconductor tracker (SCT) consists of four barrel layers and eighteen end-cap discs. They are composed of 4088 two-sided silicon microstrip modules with 6.3 million readout strips. The intrinsic accuracies for modules in the barrel are 17 μm in $r-\phi$ and 580 μm in z coordinates. In the end-cap discs they are 17 μm in $r-\phi$ and 580 μm in r coordinates. The semiconductor tracker covers a pseudorapidity range of $|\eta| < 2.5$. It provides up to 8 hits per charged particle and it is the main detector system for momentum measurements.

Transition Radiation Tracker

The transition radiation tracker (TRT) is composed of straw tubes. In the barrel region there are about 50,000 straw tubes of 144 cm in length aligned parallel to the beam pipe. They are divided into two halves at $\eta = 0$ to cover side-A and side-C of the detector. In the end-caps there are about 250,000 straw tubes of 37 cm in

length arranged in wheels perpendicular to the beam pipe. Every straw tube is 4 mm in diameter and filled with a xenon, carbon dioxide and oxygen gas mixture. In the center of the tubes there is a 31 μm diameter gold-plated tungsten wire.

The TRT covers a pseudorapidity range of $|\eta| < 2.0$ and every track typically provides 36 hits. The measurement is two-dimensional in $r - \phi$ coordinates only, with intrinsic accuracy of 130 μm. High number of hits compensate the two-dimensional measurement of lower precision and is contributing significantly to momentum measurement of electrons and high-momentum muons.

Transition radiation is a form of electromagnetic radiation emitted by a charged particle when it propagates through inhomogeneous or stratified material. Ultrarelativistic particles emit X-ray radiation when crossing the boundary between two materials of different dielectric constants. The transition radiation happens because electric and magnetic fields induced by the particle are different in the two materials and this difference needs to be radiated. The intensity of the radiation is proportional to the Lorentz factor of the particle and therefore light particles, which typically have higher Lorentz factor, radiate more than heavy particles. This allows a discrimination between electrons and hadrons. The amount of radiated X-ray photons is generally small; it is expected that electrons with $p_T > 2$ GeV produce seven to ten high-threshold hits in the TRT.

The TRT is saturated at high charged particle density expected to happen at the High Luminosity LHC (HL-LHC). During Long Shutdown 3 this part of the inner detector will be replaced by silicon microstrip modules while the pixel and SCT detectors will be renewed using current technologies. At the HL-LHC the inner detector will become the inner tracker (ITk).

2.2.3 Calorimeter

The ATLAS calorimeter, shown in Fig. 2.5, comprises electromagnetic, hadronic and forward calorimeters [73, 74]. The electromagnetic calorimeter (ECAL or EM calorimeter) is surrounded by the hadronic calorimeter (HCAL) and there are two forward calorimeters (FCAL) which extend pseudorapidity coverage to a maximum of $|\eta| < 4.9$. The calorimeters are segmented in (η, ϕ) coordinates for lateral shower shape measurement and each calorimeter has at least three layers allowing for longitudinal shower shape profile measurements. The calorimeters have segments of active material which measure energy deposits, and passive material which ensures that the energy of particles are fully absorbed in the detector volume.

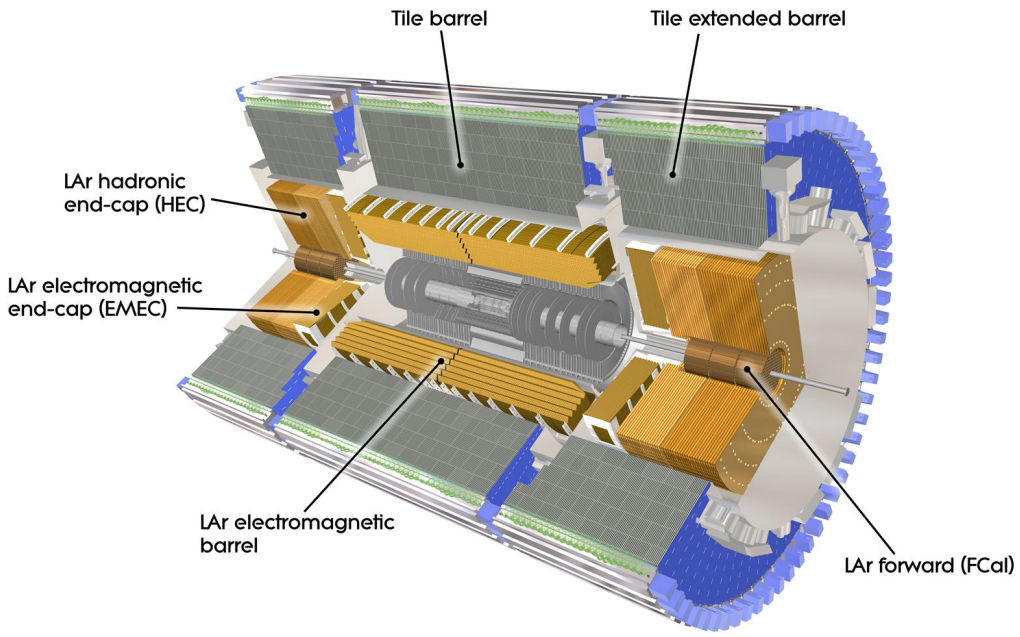

Figure 2.5: The structure of the ATLAS calorimeter [59].

Electromagnetic Calorimeter

The high-granularity sampling electromagnetic calorimeters cover a pseudorapidity range of $|\eta| < 3.2$. The calorimeter is based on liquid argon (LAr) as the active material and lead as the absorber. The central region of the ECAL, the barrel, covers $|\eta| < 1.475$ and has three sampling layers. The EM end-cap (EMEC) has two layers in the range $1.375 < |\eta| < 1.5$, three layers in the range $1.5 < |\eta| < 2.5$ and two in $2.5 < |\eta| < 3.2$. The first barrel layer, also called strip layer, is finely segmented in η for a superb $\pi^0 \to \gamma\gamma$ identification. The second layer collects most of the energy deposited by electrons and photons and the third layer is used to correct for energy leakage of very energetic showers. Complementary presampler layer in the barrel $|\eta| < 1.52$ and end-cap $1.5 < |\eta| < 1.8$ regions measures energy upstream the EM calorimeter. The accordion geometry of the ECAL provides complete coverage in ϕ without cracks. Over the region $|\eta| < 2.5$ devoted for precision physics where the inner detector matches the calorimeter, the calorimeter segmentation in lateral and longitudinal directions is finer than in the rest of the calorimeter and therefore is ideal for electron and photon measurements.

The relative energy resolution of the LAr calorimeter is parameterized by

$$\frac{\sigma_E}{E} = \frac{10\%}{\sqrt{E}} \oplus \frac{0.17}{E} \oplus 0.7\% \tag{2.2.1}$$

where the units for E is in GeV. The first term is the stochastic term, the second is the electronic noise (without pile-up) term and the last is the constant global term.

LAr readout is sensitive to 24 previous bunch-crossings during the 25 ns bunch spacing runs and therefore has an increased sensitivity to out-of-time pile-up. The LAr calorimeters use bipolar signal shaping with positive and negative output to ensure that the average signal caused by pile-up averages to zero. The read-out is optimized for the 25 ns bunch spacing operation.

Hadronic and Forward Calorimeters

The hadronic calorimeter covers the pseudorapidity range of $|\eta| < 3.2$ and is based on two different technologies: a LAr active material calorimeter as in the ECAL, but with copper absorbers, and plastic scintillator tiles (Tile) for the active material with steel for the absorber. Fast readout of the Tile calorimeter makes it relatively insensitive to out-of-time pile-up. The HCAL is structured into a barrel $|\eta| < 1.0$ and extended barrel $0.8 < |\eta| < 1.7$ regions which use Tile/steel technology and has three sampling layers. The end-cap region of the HCAL spans the range of $1.5 < |\eta| < 3.2$, uses LAr/copper technology and has four layers. Between the barrel and extended barrel sections there are scintillators covering the range of $0.85 < |\eta| < 1.51$. The forward calorimeters span the range of $3.1 < |\eta| < 4.9$ and comprise LAr active material with copper absorbers optimized for EM measurements and with tungsten absorbers for hadronic measurements.

The relative energy resolution of the hadronic Tile and LAr calorimeters is parameterized by

$$\frac{\sigma_E}{E} = \frac{50\%}{\sqrt{E}} \oplus 3\% \tag{2.2.2}$$

and that of the forward calorimeter by

$$\frac{\sigma_E}{E} = \frac{100\%}{\sqrt{E}} \oplus 10\% \tag{2.2.3}$$

2.2.4 Muon Spectrometer

The muon spectrometer [75], shown in Fig. 2.6, is the outermost layer of the ATLAS detector and is made of high-precision tracking chambers, trigger chambers, and superconducting air-core toroid magnets. The spectrometer is used primarily to reconstruct and identify muons in pseudorapidity region $|\eta| < 2.7$ and to trigger events with muons in the range of $|\eta| < 2.4$. The spectrometer consists of one barrel and two end-cap sections covering pseudorapidity regions of $|\eta| < 1.05$ and $1.05 < |\eta| < 2.7$, respectively. A system of three large superconducting air-core toroid magnets provides magnetic field used for muon momentum measurements. Over the range $|\eta| < 1.4$ magnetic bending is provided by the large barrel toroid while in the region of $1.6 < |\eta| < 2.7$ muon tracks are bent by two smaller end-cap magnets. Over the transition region $1.4 < |\eta| < 1.6$ magnetic bending is provided by a combination of barrel and end-cap magnets.

The entire spectrometer is composed from various active elements. Resistive plate chambers (RPC) cover $|\eta| < 1.05$ and thin gap chambers (TGC) cover $1.0 < |\eta| < 2.4$ and are used for event triggering and muon track position measurements. Monitored drift tube chambers (MDT) cover the entire pseudorapidity range of the spectrometer and provide precise momentum measurement capabilities. The innermost layer of the spectrometer in the pseudorapidity range $|\eta| < 2.0$ is equipped with cathode strip chambers (CSC) instead of MDTs. The muon chambers are aligned with a precision between $30\,\mu$m and $60\,\mu$m.

2.3 ATLAS Trigger System

The ATLAS trigger and data acquisition system (TDAQ) [76] is engineered to deal with high LHC collision rates and high luminosity. The bunch spacing of 25 ns results in a bunch crossing rate of 40 MHz, and each bunch crossing results in a few dozens of proton-proton collisions (in-time pile-up). These conditions imply that the rate of proton-proton collisions in ATLAS is of the order of 1 billion (10^9) per second. Selective processing of these collisions is required to reduce the initial collision rate to a more manageable rate for storing the collision events. The vast majority of *pp* collisions are low-energy inelastic collisions, as was explained in Section 1.5, and therefore the selection of events is mostly based on high-energy objects produced in hard-scatter collisions which indicate interesting physics events.

The hardware-based level-1 (L1) trigger is capable of analyzing event data

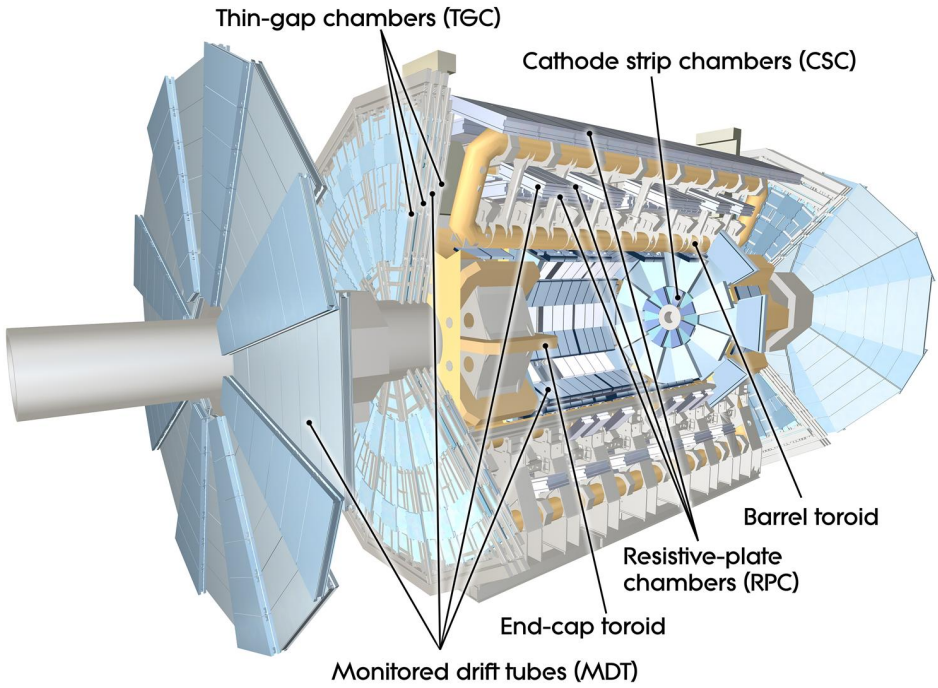

Figure 2.6: The ATLAS muon spectrometer and its components, located outside the ATLAS calorimeter [59].

at the bunch crossing rate of 40 MHz and accepts events at an average rate of 100 kHz for further processing. The software-based high-level trigger (HLT) receives information from L1 at its output rate and selects events for storage at an average rate of 1 kHz.

L1 decision is formed by the Central Trigger Processor (CTP) which receives information from the calorimeter (L1Calo) and muon (L1Muon) triggers. Its latency is about 2.5 μs which includes the time needed for signals to travel from the detector to the trigger system and back to the readout electronics. CTP also applies preventive dead-time. It limits the minimum time between two consecutive L1 accepts (simple dead-time) to avoid overlapping readout windows, and restricts the number of L1 accepts allowed in a given number of bunch crossings (complex dead-time) to prevent front-end buffers from overflowing. Data from the L1 accepted events are buffered into the Readout System (ROS) and processed by HLT. HLT receives region-of-interest (RoI) information from L1 and runs reconstruction and identification algorithms very much like the offline algorithms. HLT has access to information from the whole detector and therefore is capable of running precision

tracking.

Trigger rates depend on the center-of-mass energy and they increase due to more probable production of hard objects. Additionally, short bunch spacing increases detector sensitivity to out-of-time pile-up which increases the rate of the muon trigger. Also, increase in luminosity results in the increased production of objects which can trigger an event recording and consequently increase the trigger rate. While the CoM energy and bunch spacing are constant for each LHC fill, luminosity may vary significantly and it is taken into account when the trigger menu is prepared.

During Run 2 two new level-1 triggers have been commissioned. A new topological trigger (L1Topo) [77] is programmed to perform selections based on geometric or kinematic association between trigger objects received from the L1Calo and L1Muon systems. This includes the refined calculation of global event quantities such as missing transverse momentum. A new Fast TracKer (FTK) [78] system is programmed to provide global ID track reconstruction at L1 trigger rate using lookup tables for pattern recognition.

L1Calo

The level-1 calorimeter triggers use coarse information from ECAL and HCAL, and identify regions-of-interest, shown in Fig. 2.7, which seed electron/photon, tau, jet or $E_{\mathrm{T}}^{\mathrm{miss}}$ high-level triggers. The granularity of L1Calo trigger towers, which span all the calorimeter layers, is 0.1×0.1 in $\Delta\phi \times \Delta\eta$ space, and towers are calibrated at the EM energy scale. The L1Calo electron/photon or tau RoIs are defined as 2×2 trigger tower clusters in the electromagnetic calorimeter in which the sum of transverse energy[2] in 2×1 or 1×2 tower cluster exceeds a predefined energy threshold. Isolation thresholds can be set for the ring of towers around the RoI, for the 2×2 tower cluster in the hadronic calorimeter behind the RoI, and similarly for the ring of towers around it. E_{T} thresholds can be set for different η region at the granularity of 0.1 in η. The level-1 jet RoI is defined as the 4×4 or 8×8 tower cluster in the hadronic and electromagnetic calorimeters in which the sum of transverse energy exceeds a predefined threshold and which surrounds a local maximum in the 2×2 core. The L1Calo then uses jet RoIs to produce global sums of scalar and missing transverse momentum.

[2]Transverse energy, E_T, is defined as the total energy of a cell or cluster multiplied by $\sin\theta$, where θ is the polar coordinate of that cell or cluster.

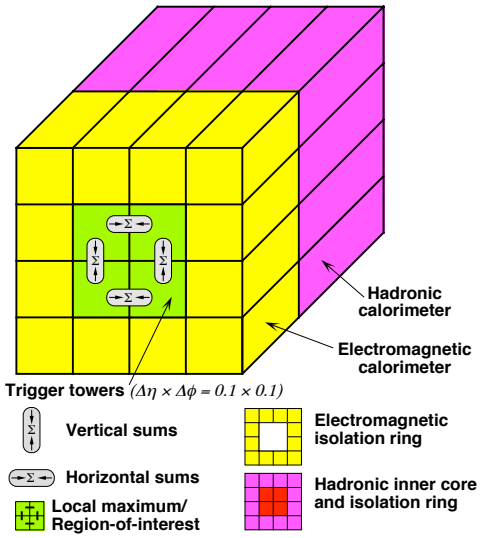

Figure 2.7: Schematic view of the trigger towers used as input to the L1Calo trigger algorithms [76].

L1Muon

L1Muon trigger system [79] uses signals from the RPC system in the region $|\eta| < 1.05$ and from the TGC system in the region $1.05 < |\eta| < 2.4$. Muon candidates are formed from coincidences between different planes of those systems. In order to form coincidences, hits in RPC and TGC must lie within parametrized geometrical muon roads. Roads stand for envelopes containing muon trajectories which originate from the nominal interaction point. Additionally, the L1Muon trigger system identifies correct bunch crossings from which muon candidates originate. In order to assign the hit information to the correct bunch crossing, a precise timing between the RPC and TGC systems is achieved.

Trigger Menu

The trigger menu is a list of L1 and HLT trigger chains and they are categorized in the following way:

- Primary triggers are used for physics analyses and are typically unprescaled.
- Support triggers are used for efficiency and performance measurements or for monitoring; they are typically run at small rates using prescale factors.
- Alternative triggers use alternative reconstruction algorithms for testing pur-

poses compared to the primary or support triggers and typically have large overlap with the primary triggers.

- Backup triggers have tighter selection and smaller rate in case the primary triggers produce too large of an event rate than expected.
- Calibration triggers are used for detector calibration and typically run at very high rates but store very small amount of relevant information only.

A trigger prescale is a number which indicates how many events are skipped by that trigger chain in order to reduce the rate. If a L1 trigger chain is prescaled with a prescale n, it is applied before the attempt to process an event and therefore every nth event is processed. For a HLT trigger chain with a prescale n, it is applied for the events which pass the trigger chain selection and therefore every nth event is recorded.

The primary triggers cover the entire set of objects which can be reconstructed in the ATLAS detector and which are needed for the ATLAS physics program. Objects that may trigger event recordings include electrons, photons, muons, taus, jets and b-jets, $E_{\mathrm{T}}^{\mathrm{miss}}$ and $\sum E_{\mathrm{T}}$ (see Chapter 3).

2.4 Luminosity in ATLAS

Luminosity is important for determining the expected number of background and signal events when they are estimated with Monte Carlo simulation. It is calculated and measured in the following way. Bunch luminosity, which is provided by a single pair of colliding bunches, is expressed as [80]

$$\mathcal{L}_{\mathrm{b}} = \frac{\mu f_{\mathrm{r}}}{\sigma_{\mathrm{inel}}}, \tag{2.4.1}$$

where the pile-up parameter, μ, is the average number of inelastic interactions per bunch crossing, f_{r} is the bunch revolution rate and σ_{inel} is the proton-proton inelastic cross-section. Instantaneous luminosity is then given by summing over the total number of bunches, n_{b}:

$$\mathcal{L} = \sum_{\mathrm{b}=1}^{n_{\mathrm{b}}} \mathcal{L}_{\mathrm{b}} = n_{\mathrm{b}} \langle \mathcal{L}_{\mathrm{b}} \rangle = n_{\mathrm{b}} \frac{\langle \mu \rangle f_{\mathrm{r}}}{\sigma_{\mathrm{inel}}}, \tag{2.4.2}$$

where $\langle \mathcal{L}_{\mathrm{b}} \rangle$ is the mean bunch luminosity and $\langle \mu \rangle$ is the bunch-averaged pile-up parameter.

ATLAS monitors the delivered luminosity by measuring μ_{vis}, the average number of visible inelastic interactions per bunch crossing. For this measurement ATLAS uses a variety of different detectors, called luminometers, and algorithms. The μ_{vis} parameter can be expressed as $\mu_{\mathrm{vis}} = \epsilon\mu$, where ϵ is the efficiency of the detector and the algorithm used. With this information the bunch luminosity can be rewritten as

$$\mathcal{L}_{\mathrm{b}} = \frac{\mu_{\mathrm{vis}} f_{\mathrm{r}}}{\sigma_{\mathrm{vis}}}, \tag{2.4.3}$$

where $\sigma_{\mathrm{vis}} \equiv \epsilon\sigma_{\mathrm{inel}}$ is the visible pp inelastic cross section for the same detector and algorithm used. In order to use the measured parameter μ_{vis} for the luminosity scale, the visible pp cross section must be known. Each detector and algorithm must be calibrated to determine their visible cross section σ_{vis}. The calibration of the visible cross section can be performed in a dedicated absolute luminosity measurement and the measurement of μ_{vis} using Eq. 2.4.3. The absolute luminosity is calculated from the known beam parameters using the van der Meer (vdM) method. In order to use this method, the absolute luminosity is expressed as

$$\mathcal{L}_{\mathrm{b}} = \frac{f_{\mathrm{r}} n_1 n_2}{2\pi \Sigma_{\mathrm{x}} \Sigma_{\mathrm{y}}}, \tag{2.4.4}$$

where Σ_{x} and Σ_{y} are the horizontal convolved beam sizes in the orthogonal x and y directions, and ns are the numbers of protons in two colliding bunches. The Σs are measured in the dedicated van der Meer scans. During these scans the beams are gradually separated horizontally in orthogonal x and y directions and consequently constitutes measurements of Σs. With this information the absolute luminosity scale is calculated from Eq. 2.4.4 and, when combined with Eq. 2.4.3, provides an estimate of the visible inelastic cross section for a particular detector and algorithm:

$$\sigma_{\mathrm{vis}} = \mu_{\mathrm{vis}}^{\mathrm{MAX}} \frac{2\pi \Sigma_{\mathrm{x}} \Sigma_{\mathrm{y}}}{n_1 n_2}. \tag{2.4.5}$$

Here $\mu_{\mathrm{vis}}^{\mathrm{MAX}}$ is the average number of visible interactions per bunch crossing reported at the peak of the scan curve by that particular algorithm. Finally, the σ_{vis} measured in this way can again be used in Eq. 2.4.3 together with the measurement of μ_{vis} during nominal running conditions and consequently this provides the

measurement of bunch luminosity.

The information needed for physics analyses is the integrated luminosity, calculated for some well-defined data taking periods. The smallest time unit for storing luminosity information is the luminosity block (LB). It is a duration under which data taking conditions do not change and it lasts approximately one minute. It is also assumed that luminosity is constant in each luminosity block although it slightly decreases due to proton scattering during which the bunch intensity decreases. Instantaneous luminosity measured in each luminometer is averaged over the luminosity block and stored in the database. The integrated luminosity for a LB is calculated by multiplying instantaneous luminosity by the duration of that LB. The integrated luminosity for physics analyses is a sum over LBs where data taking conditions and data quality requirements are satisfied.

2.5 ATLAS Operation in Run 2

Run 2 of the LHC lasted from 2015 to 2018 and delivered a breathtaking amount of proton-proton collisions to ATLAS corresponding to the integrated luminosity of $158\,\text{fb}^{-1}$ at a center-of-mass energy of $13\,\text{TeV}$, as shown in Fig. 2.8. ATLAS processed a large fraction of these collisions corresponding to the integrated luminosity of $149\,\text{fb}^{-1}$. This luminosity corresponds to a total of about 12 quadrillion (12×10^{15}) inelastic proton-proton collisions, based on the pp cross section of $78\,\text{mb}$ [81]. This many collisions produced around 7.6 million Higgs bosons, based on the total production cross section of $51\,\text{pb}$ [82]. ATLAS recorded less collisions than delivered by the LHC due to the detector warm-up and data acquisition system inefficiency. The detector warm-up is a short time period from the moment the LHC declares stable beams and ATLAS starts ramping up the voltage of tracking detectors and pixel preamplifiers. The data suitable for physics analyses corresponds to $140\,\text{fb}^{-1}$ and satisfies the All Good Data Quality criteria, which require all reconstructed physics objects to be of good data quality.

The analysis presented in this thesis uses the pp collision data set collected in 2015 and 2016. The amount of good quality data in 2015 was $3.2\,\text{fb}^{-1}$ and in 2016 it was $32.9\,\text{fb}^{-1}$, which adds up to the total of $36.1\,\text{fb}^{-1}$.

The instantaneous luminosity and the average number of collisions per bunch crossing were generally increasing throughout Run 2 indicating perfect LHC performance and allowing to record large amount of data. The designed luminosity of $1 \times 10^{34}\,\text{cm}^{-2}\text{s}^{-1}$ was achieved in 2016 and by the end of 2018 it grew more than

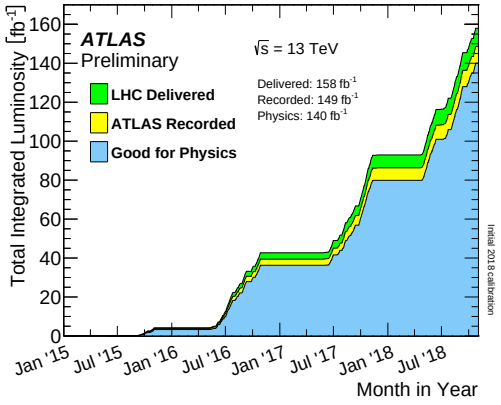

Figure 2.8: Cumulative distribution of the total integrated luminosity in ATLAS during Run 2. Shown are the distributions of the LHC delivered luminosity, ATLAS recorded luminosity, and luminosity of good quality data [83].

twice, as shown in Table 2.1. The mean number of interactions per bunch crossing was mostly in the range between 10 and 70, as shown in Fig. 2.9, reaching the peak value of 90.5 in the end of 2018 (not shown in the plot as it was a special test run). The plot also shows the amount of data collected during the special runs in low pile-up environment with $\mu = 2$.

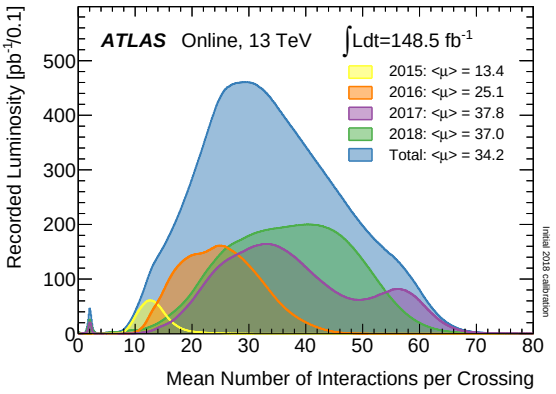

Figure 2.9: Distributions of the average number of interactions per bunch crossing in ATLAS during Run 2 [83].

Table 2.1: List of notable run conditions in ATLAS during Run 2.

Property \ Year	2015	2016	2017	2018
Peak Luminosity ($\times 10^{34}\,\mathrm{cm}^{-2}\mathrm{s}^{-1}$)	0.50	1.38	2.09	2.14
Maximum average collisions per bunch crossing, μ_{max}	28.1	52.2	79.8	90.5
Maximum colliding bunches	2232	2208	2544	2544

Chapter 3

Physics Objects

Processes with photons, electrons, muons, taus and jets in the final states play primary roles in the ATLAS physics program. These objects are reconstructed and identified from the combinations of signals in various ATLAS detector systems, described in section 2.2. The experimental signatures arising from various final state particles are used to trigger event recordings with the ATLAS trigger system, described in section 2.3.

3.1 Tracks and Primary Vertices

Crucial building blocks of many physics objects are tracks, the trajectories of charged particles. Tracks are reconstructed from clusters of signals in the pixel and microstrip sensors, and drift circles in the straw tube tracker, collectively referred to as "hits". Hits in the silicon tracker are also referred to as precision hits. Due to fast read-out of the silicon trackers the track reconstruction is mostly affected by in-time pile-up.

A primary vertex (PV) is a reconstructed vertex with at least two tracks with $p_{\mathrm{T}} > 400\,\mathrm{MeV}$ associated to it. The hard-scatter vertex is a primary vertex with the highest sum of transverse momentum squared of the tracks associated to it. An event can have multiple primary vertices (N_{PV}) but it has only one hard-scatter vertex.

Distance parameters relative to primary vertices and the beam-line are used for the definition of good-quality tracks. The transverse impact parameter d_0 is the shortest distance between the track and the beam-line; σ_{d_0} is the associated uncertainty to this parameter. The longitudinal impact parameter z_0 is the distance

along the z axis from the point where d_0 is measured to the beam-spot position, and Δz_0 is the distance from the d_0 measurement point to the primary vertex position.

The vertex resolution depends strongly on the number of associated tracks and on the event topology. Generally, higher track multiplicity and tracks with large momentum lead to significantly better vertex resolution.

3.2 Electrons and Photons

Electrons and photons provide a clean signature for various physics analyses. The excellent performance of the ATLAS detector for the measurement of these objects enables precision measurements of known physics phenomena as well as searches for new physics.

In proton-proton collisions photons originate from non-resonant QCD+QED production where prompt photons are produced in association with jets or in pairs. Also, prompt photons appear in the decays of heavy particles. The study of QCD production of photons allows to test perturbative and non-perturbative regimes of QCD and gain information about parton distributions. In addition, photons are fundamental to the discovery and properties measurements of the SM Higgs boson.

Prompt electrons are produced in the decays of heavy particles and non-prompt electrons appear in the decays of hadrons inside jets. The particular decay channel $\tau \to e\nu_e\nu_\tau$ with an electron in the final state provides an experimental signature for the search of a Higgs boson in the $H/A \to \tau\tau$ decay channel.

In the ATLAS detector photons propagate through the inner detector and the electromagnetic calorimeter, and therefore are reconstructed from energy deposits in the EM calorimeter and with or without associated tracks in the ID. Photons have associated tracks if they interact with detector material and convert into an electron-positron pair. Electrons (and positrons) also propagate through the inner detector and the electromagnetic calorimeter. The reconstructed tracks from the tracker and clustered energy deposits in the calorimeter are combined to fully reconstruct electrons.

Electron Reconstruction

The fiducial region for electrons is $|\eta| < 2.47$ excluding the calorimeter transition region $1.37 < |\eta| < 1.52$. The reconstruction of electrons comprise several steps [84]. First, a sliding window algorithm is used to search for cluster seeds in the

electromagnetic calorimeter, the step called seed-cluster reconstruction. The entire EM calorimeter is divided into 200×256 elements of size 0.025×0.0245 in $\eta \times \phi$ space, called towers. Towers are spanning all layers of the EM calorimeter, including the presampler where relevant. The energy from cells in all the layers is summed into the tower energy; if a cell belongs to several towers, the energy is divided equally among them. The size of the sliding window is 3×5 in units of 0.025×0.0245 in $\eta \times \phi$ space which is the granularity of the EM calorimeter middle layer. The sliding window consists of several towers and a window with a total transverse energy above 2.5 GeV is selected as the seed. The clustering algorithm is then used to form complete clusters around the seed.

The second stage in the electron reconstruction is the track reconstruction which itself consists of two steps: pattern recognition and track fit. The seed for a track is taken as three hits in different layers of the silicon detectors and is required to have transverse momentum larger than 1 GeV. The pattern recognition step tries to extend the seed to a full track with at least seven hits using either pion or electron hypotheses. First, the pion hypothesis is used to account for energy losses due to interactions with the detector material. If the pattern recognition with the pion hypothesis fails, but the track seed falls within an EM cluster region of interest, the electron hypothesis is used. The EM cluster region of interest is defined as the cluster passing loose shower shape requirements. The track candidate is then fit using either the pion or electron hypothesis, whichever was used in the pattern recognition step. If the fit using the pion hypothesis fails, the track is fit again using the electron hypothesis.

The third stage is called the electron specific track fit. Track candidates are extrapolated into the EM calorimeter middle layer and matching between the track position and the cluster barycenter is performed. The track-cluster matching is carried out using η and ϕ coordinates between the two objects. Tracks having 4 or more precision hits and matched to a cluster are refit using Gaussian Sum Filter [85] which takes into account the non-linear bremsstrahlung effects. Finally, after the refit, a stricter track matching to an EM cluster is performed, which finalizes the electron reconstruction.

Occasionally several tracks are matched to the same energy cluster. In this case a primary track is selected based on the distance between a track and the cluster barycenter calculated using different momentum hypotheses and other criteria. The η and ϕ coordinates of the electron are given by the primary track coordinates relative to the beam-line. Electron candidates without any associated

precision hit tracks are removed and considered to be photons. The efficiency of this association of precision hit tracks to the clusters is the reconstruction efficiency.

The momentum of the electron candidate is calculated from both the primary track and the calibrated energy cluster. The energy of the cluster (also for photon reconstruction) is calibrated using MC simulation and real data based on multivariate techniques [86]. A multivariate regression algorithm corrects energy of electromagnetic particles due to losses in front of the calorimeter and outside the cluster. The electron energy scale is extracted from in-situ measurements of $Z \to ee$ decays.

Additional track quality cuts are employed to reduce backgrounds from photon conversion and heavy flavor decay. The track quality cuts used with all electron identification working points are $d_0/\sigma_{d_0} < 5$ and $\Delta z_0 \sin\theta < 0.5\,\text{mm}$. The efficiency of these requirements are estimated together with the identification efficiency.

Electron Identification

The electron identification algorithm is used to determine whether the electron candidate behaves more like a real electron or as a background object, presumably a converted photon or hadronic jet. The algorithm employs information from calorimeter shower shapes, track-cluster matching, track conditions, hits in the transition radiation tracker and energy leakage to the hadronic calorimeter. The IBL, as the first active layer, provides additional discriminating power between electrons and converted photons. The information from the TRT is encapsulated in a likelihood discriminant variable based on the probability for each hit to exceed the high-threshold requirement. All the information is combined in a single likelihood discriminant constructed from probability density functions of the input variables. Additionally, some discrete variables such as track hits are used for cut-based selection.

The electron shower shape variables depend strongly on the position in the detector due to varying amount of material that the electron has to cross. Moreover, the shower shape quantities and track variables depend significantly on the electron energy. To take these effects into account, the electron identification algorithm is optimized in several bins in pseudorapidity and transverse energy.

Three working points of the identification algorithm are defined, which differ from each other by the background rejection power. The working points of increasing background rejection are labeled as “loose”, “medium” and “tight”.

The electron and background identification efficiencies are shown in Fig. 3.1. The electron identification efficiency was measured in the simulated $Z \to ee$ samples with respect to the reconstructed electrons. For the background identification efficiency the simulated di-jet samples were used. The electron identification efficiency ranges from 78% to 97% depending on the working point and transverse energy.

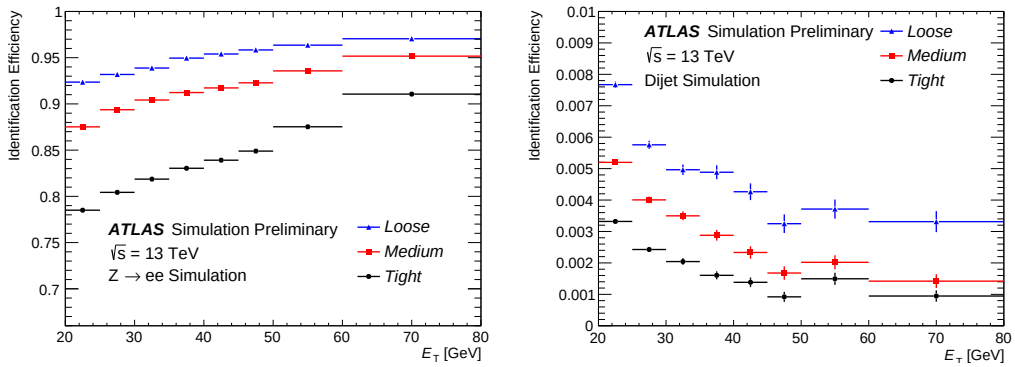

Figure 3.1: (left) Electron and (right) background identification efficiencies for the three working points as a function on the transverse energy [84].

Electron Isolation

Electron isolation is a measure of activity in the detector around the reconstructed electron candidate. The isolation variables allow discrimination between prompt electrons and background electrons originating from photon conversion in hadron decays, electrons from heavy-flavor hadron decays and mis-identified light-flavor hadrons. Two isolation measures are used to describe the activity in the inner detector around the associated tracks of the electron and around the energy clusters in the calorimeter. A track isolation $p_{\mathrm{T}}^{\mathrm{varcone0.2}}$ is defined as the sum of transverse momenta of all tracks satisfying track quality requirements and within a cone $\Delta R = \min(0.2, 10\,\mathrm{GeV}/E_{\mathrm{T}})$ of the primary track of the electron. The surrounding tracks are also required to originate from the primary vertex of the hard collision. The sum excludes tracks associated with the electron candidate. A calorimetric isolation $E_{\mathrm{T}}^{\mathrm{cone0.2}}$ is defined as the sum of the energy of topological cluster (see Section 3.4) surrounding the electron barycenter within a cone of $\Delta R = 0.2$. The topological clusters are calibrated at the electromagnetic scale and only clusters with positive energy are added to the sum. The bulk energy from the electron candidate in a

window of size $\eta \times \phi = 0.125 \times 0.175$ centered around the barycenter is subtracted. Additional corrections depending on η and E_{T}, as well as depending on pile-up, are applied.

The isolation variables are used to define cuts for isolated electron candidates. Two types of isolation working points are defined: efficiency-targeted and fixed-requirement working points. The efficiency-targeted working points are defined to provide known signal efficiency at particular values of transverse energy. The fixed-requirement working points are defined by a fixed cut on the isolation variables.

Electron Trigger

ATLAS trigger system targets electron candidates to trigger event recording. Both L1 and HLT trigger levels reconstruct and identify electron candidates. The L1Calo trigger system uses signals in both the electromagnetic and hadronic calorimeters to calculate energy in regions of 4×4 trigger towers, corresponding to a size of $\approx 0.4 \times 0.4$ in $\eta \times \phi$ space. These regions are used to calculate certain variables, such as the energy leakage to the hadronic calorimeter and relative energy in the core and isolation regions, and use these variables to define trigger requirements. The HLT trigger system proceeds in several steps with the aim to reject events as soon as possible in the trigger chain. Initially, fast algorithms build energy clusters in the EM calorimeter from cells within the regions-of-interest that were identified by the L1 trigger and requirements based on the cluster shower shapes are applied. Tracks are reconstructed using a fast simplified technique and are loosely matched to the clusters. If the event is not rejected, the trigger chain proceeds by using precise offline-like algorithms. Calorimeter clusters are built in the same way as in the offline reconstruction. Additional shower shape requirements are applied to reduce the event rate before the precision tracking step. Then, the electron candidates are built from precision tracks matched to calorimeter cluster. The identification step is performed for the fully reconstructed electron candidates using the same likelihood-based approach as offline.

The trigger efficiency is measured with respect to electron probes which are required to pass the offline reconstruction and identification requirements. The efficiency is defined as the ratio of the number of probes that in addition pass the trigger requirement to the total number of probes in the sample.

Electron Performance Measurements

The electron reconstruction, identification, isolation and trigger efficiencies have been measured with the 2015 data set and MC using the tag-and-probe method. The method uses electron samples from the $Z \to ee$ and $J/\psi \to ee$ decays. One of the electron is called a tag and is required to pass strict selection requirements, while the other is called a probe and is exploited for efficiency measurements. The invariant mass of the electron pair is also required to be compatible with the mass of the decaying resonance, and in the case of J/ψ the lifetime information from the reconstructed vertex is used. These requirements provide an unbiased sample of probe electrons and, moreover, each valid pair in the sample is considered in the efficiency measurements: an electron can be the probe in one pair and the tag in another pair.

The total efficiency to select an electron is a product of multiple efficiencies where various components can be measured with respect to the previous step. The efficiencies are measured in data and MC and the ratio of the efficiencies are used as data-to-MC scale factors to correct for electron mis-modeling in various physics analyses. Since electron efficiencies depend on transverse energy and pseudorapidity, the scale factors are calculated in 2-dimensional array in E_T and η space.

The systematic uncertainties of the measurements are estimated from variations of the tag selection and background model. The central value of a measured efficiency is taken as the average of results over all the analysis variations. The systematic uncertainty is taken as the root mean square of the distribution of measurement results in all the different variations. The statistical uncertainty is taken as the average of statistical uncertainties over all variations.

Reconstruction efficiency is measured for reconstructed electrons with an associated track passing track quality requirements with respect to the total number of energy clusters in the EM calorimeter from electrons. The clustering algorithm is found to be more than 99% efficient for electrons with $E_T > 15\,\text{GeV}$ and therefore they are the cornerstone for the reconstruction efficiency measurement. The efficiency to reconstruct electrons with a good quality track is found to be between 97% and 99% with a smaller efficiency of 95% in the calorimeter transition region. Identification efficiency is measured for electrons passing a particular identification operating point with respect to electrons having an associated primary track which passes track quality requirements. The electron isolation efficiency is measured for electron candidates that pass identification and isolation requirements with respect

to the candidates which only fulfill an identification requirement for all combinations of identification and isolation working points. The electron trigger efficiency is defined as the ratio of the number of probe electrons that are matched to the required HLT electron within a cone of size $\Delta R = 0.07$ to the total number of probe electrons. The offline electron candidates for this measurement are required to pass identification and isolation criteria and the efficiencies are measured for all trigger working points with respect to all combinations of identification and isolation working points.

Photon Reconstruction

Photon reconstruction begins in the same way as the electron reconstruction. The cluster-seed reconstruction step uses a sliding window algorithm to find the seed and then a clustering algorithm is used to construct clusters. The efficiency of the clustering step is found to be 99% for photons with $E_T > 20\,\text{GeV}$. The tracking step, the same as in the electron case, aims to loosely match tracks to the cluster seeds with the expectation that the tracks come from conversion photons. EM calorimeter clusters to which no tracks have been matched are considered unconverted photons. On the other hand, conversion photons are those which transform into an electron-positron pair before reaching the EM calorimeter. For the conversion vertex reconstruction the important building blocks are silicon tracks, which have hits in the silicon detector, and TRT tracks, which have hits in the TRT only. The two-track conversion vertices are built from pairs of tracks which have their invariant mass consistent with zero. The single-track conversion vertices are built from single tracks without hits in the innermost detector layers, which discriminates them from electron candidates. The tracks must generally have a high probability to be electron tracks as determined from the measurements in the TRT. In case there are multiple vertices associated with a cluster, the preference is set for double-track vertices with two silicon tracks over other double-track conversions and followed by single-track conversions. The efficiency to reconstruct a true converted photon is higher than 70% for photons with $E_T > 20\,\text{GeV}$, as determined from simulation. The dependence on pile-up is also measured resulting in the efficiency of 65% at $\mu = 60$ and increasing to 75% at $\mu \approx 0$. The efficiency for a true unconverted photon to be reconstructed as a converted photon is below 9% at $\mu = 60$ and decreases to 1% at $\mu < 24$.

The majority of reconstructed photon candidates are non-prompt photons

produced in the decays of hadrons in jets. Smaller amount of background comes from hadrons which deposit significant amount of energy in the EM calorimeter and therefore are reconstructed as photon candidates.

Photon Identification

Photon identification algorithm uses shower shape variables and requires rectangular cuts on those variables. The fiducial region for photons is $|\eta| < 2.37$ and excluding the calorimeter transition region $1.37 < |\eta| < 1.52$. Prompt photons usually have narrower energy deposits in the EM calorimeter and smaller energy leakage in the hadronic calorimeter than non-prompt photons or jets. For the identification of a pion decay, $\pi^0 \to \gamma\gamma$, a finely segmented first calorimeter layer helps separate two local energy maxima produced by the two photons. The identification algorithm is designed to provide two identification operating points, "loose" and "tight". They are tuned to have minor dependence on the pile-up. The "loose" selection uses information from the second calorimeter layer and the hadronic calorimeter. The "tight" working point adds information from the strip layer of the calorimeter and is separately optimized for converted and unconverted photons. The selection criteria are optimized in several bins of the photon's pseudorapidity to account for different detector geometries.

Photon Isolation

Photon isolation criteria are defined with two variables representing calorimeter isolation and track isolation. The calorimeter isolation is calculated from the sum of energy in topological clusters around the photon candidate within a cone of a certain radius ΔR. The cluster energy associated to a photon candidate and energy from pile-up and underlying event are subtracted from the total sum. The track isolation is calculated from the sum of transverse momenta of all the tracks with transverse momentum larger than 1 GeV and having the distance of closest approach to the primary vertex along the beam axis less than 3 mm. The transverse momenta of tracks associated to photon conversion are subtracted from the total sum. The final photon isolation definition uses various combinations of calorimeter and track isolation with various cone size parameters.

Photon Performance Measurements

The identification efficiency of the "tight" working point was measured using three methods to cover full photon kinematics. The radiative Z boson decays, $Z \to \gamma ll$, provide a clean sample of prompt photons with energies between 10 and 100 GeV. The electron extrapolation method uses showers in the EM calorimeters from electrons originating from $Z \to ee$ process. In this method the electron showers are corrected to match photon showers and this sample provides information for photon identification efficiency measurements for energies between 25 and 150 GeV. The third method is called inclusive photon and it uses an inclusive sample of photons collected with a single photon trigger. This sample allows for a measurement covering a wide range of photon energies between 25 GeV and 1.5 TeV. The efficiencies are reported for converted and unconverted photons since their shower shape variables differ. The measurements are performed in 2-dimensional array in E_T and η space. Photon identification efficiencies are measured to be $50 - 60\%$ at $E_T = 10$ GeV and $95 - 99\%$ for unconverted and $88 - 96\%$ for converted photons with E_T above 250 GeV. The ratio of the efficiencies measured in data and MC are computed and provided as scale factors for physics analyses. The scale factors are compatible with unity within uncertainties and the uncertainties are as low as 1% in the region $30 < E_T < 150$ GeV and rises for $E_T < 30$GeV due to limited sample size until they reach 25% at $E_T = 10$ GeV.

3.3 Muons

Muons in the ATLAS detector have superb energy scale and resolution measurements. They are key to some important precision measurements of known phenomena and to the discovery of the SM Higgs boson in the $H \to ZZ^*$ decay channel. In proton-proton collisions, muons are produced in the decay of heavy particles while non-prompt muons are produced in the decay of hadrons inside jets. In the ATLAS detector muons propagate through all the detector layers and therefore manifest themselves by hits in the inner detector and the muon spectrometer, and generally deposit very little energy in the calorimeters.

Muon Reconstruction

Muons are reconstructed from a combined measurement of tracks in the inner detector and muon spectrometer. Tracks in the inner detector are reconstructed in

a similar way to those of electrons. On the other hand, tracks in the muon spectrometer have a different reconstruction technique. The track reconstruction starts with a search for hit patterns inside each of the muon chambers (section 2.2.4) to form segments. The segments from different layers are then combined by fitting to build a track, starting from seed segments in the middle layers of the spectrometer where more RPC and TGC hits are available. At least two segments are required to build a track except in the barrel-endcap transition region where a single high quality segment can be used for a track.

The ID and MS tracks and in some cases information from the calorimeter are combined to reconstruct a muon. Four types of muons are defined depending on the information used in the reconstruction:

- Combined (CB) muons are built from the reconstructed ID and MS tracks. A combined track is formed by performing a global fit and allowing in some cases for hits in the MS to be removed. The matching of the MS and ID tracks is performed in the outside-in manner but a reverse extrapolation from inside to outside is used as a complementary approach. The bulk of all reconstructed muons falls in this category.

- Segment-tagged (ST) muons use a track in the ID and a single segment in the muon spectrometer if the ID track can be matched to a MDT or CSC segment after extrapolation. Such muons are used when they cross only one layer of the MS chambers either due to low muon momentum or because of a reduced acceptance in certain regions.

- Calorimeter-tagged (CT) muons use an ID track and an energy deposit in the calorimeter if the energy deposit is compatible with a minimum-ionizing particle. Such muons are used to improve acceptance in regions where cabling and services to the calorimeters impede muon spectrometer instrumentation. The selection criteria for this kind of muons is optimized for muons with $|\eta| < 0.1$ and $15 < p_T < 100\,\text{GeV}$.

- Extrapolated (ME) muons use MS tracks only and with a loose requirement to be originating from the interaction point. Such muons are mainly used to improve acceptance in the forward region which is not covered by the ID.

When two muon types are associated with the same ID track the preference is give to CB muons over ST and to ST over CT. The overlap with an ME muon is resolved by giving preference to the type with better track quality.

Muon Identification

Muon identification is focused on the discrimination between prompt and non-prompt muons. The background, non-prompt, muons are originating from in-flight decays of charged hadrons, mainly pions and kaons. The tracks produced by such muons are expected to have a distinctive topology with a kick, because hadrons tend to propagate a bit inside the tracker before decaying into muons. As a result, background muon tracks have poor fit quality and, moreover, momentum measured in the ID and MS may not be compatible. These effects are exploited in the muon identification algorithm. Additionally, some requirements on the number of hits in the ID and MS are placed for a robust momentum measurement. Four specific muon identification working points are defined for the use in physics analyses:

- "medium" muons are of CB and ME types only. The ME muons are allowed only for $2.5 < |\eta| < 2.7$ to extend the acceptance uncovered by the ID.
- "loose" muons are specifically optimized for reconstructing SM Higgs boson candidates in four lepton final state. All muon types are allowed.
- "tight" muons are designed to provide purity at the cost of some efficiency. Only CB muons which satisfy "medium" working point requirements are considered for "tight" identification, which impose additional requirements.
- "high-p_T" muons have optimized selection in the region $p_T > 100\,\text{GeV}$, aiming to maximize momentum resolution. Only CB muons passing "medium" working point with additional requirements on tracks are considered.

The "medium" selection efficiency was measured using $Z \to \mu\mu$ and $J/\psi \to \mu\mu$ events in 2015 data set and in MC with the tag-and-probe method. The resulting efficiencies are shown in Fig. 3.2.

Muon Isolation

Muon isolation is a powerful property for background rejection. Prompt muons from the decays of heavy particles, such as W, Z bosons, are expected to be well separated from any additional activity in the detector. On the other hand, non-prompt muons from semileptonic decays of hadrons are expected to be surrounded by jet constituents. Muon isolation is defined with two, track-based and calorimeter-based, variables. The track-based isolation is defined as the sum of transverse momentum of tracks in a cone of size $\Delta R = \min(0.3, 10\,\text{GeV}/p_T)$ around the muon

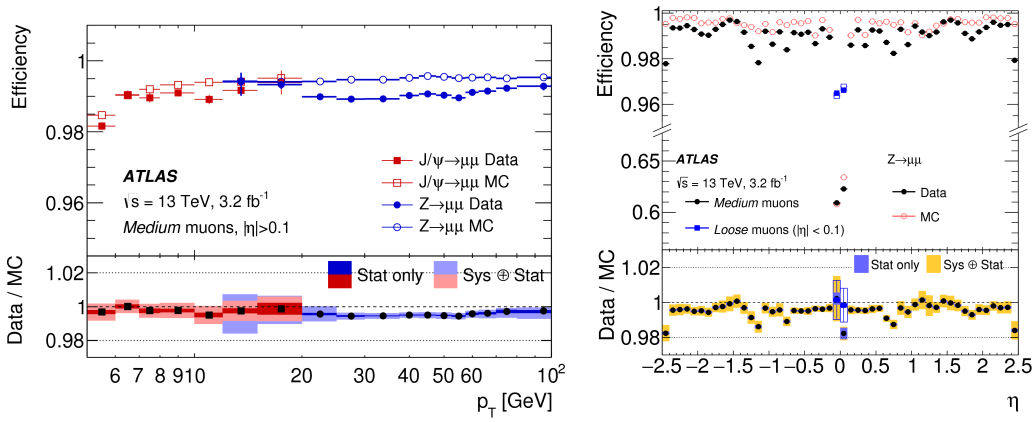

Figure 3.2: Muon reconstruction and identification efficiency for the "medium" working point as a function of the (left) muon p_T and (right) muon η [87].

track and excluding the muon track itself. The calorimeter-based isolation is defined as the sum of the transverse energy of topological clusters in a cone of size $\Delta R = 0.2$ around the muon track and excluding the energy deposited by the muon itself and deposited by pile-up. As in the case of electrons, muon isolation working points are defined as efficiency-targeted and fixed-requirement isolation types. In total seven isolation working points are defined.

3.4 Jets

Jets are sprays of hadrons originating from a single quark or gluon and forming in a process of hadronisation. They are the most abundant objects in hadron colliders due to their QCD origin and they very often accompany production of other elementary particles. Events with multiple high energy jets can be used as an experimental signature for searches of new heavy resonances, e.g. [88].

Jet constituents, hadrons, are stopped in the hadronic and electromagnetic calorimeters where they manifest themselves by producing signals in calorimeter cells. The calorimeter cell signals are clustered together into three-dimensional topological clusters [89]. Topological clusters (topo-clusters) are the main building blocks for jet reconstruction algorithms and consequently for the reconstruction of hadronically decaying tau leptons. Additionally, topo-clusters are employed to represent energy-flow of soft particles needed for missing transverse energy reconstruction.

The reconstructed jets are studied further to identify the presence of b-hadrons inside jets. Such jets are called b-jets and they are used in various measurements of top-quark physics or of the Higgs boson decay to b-quarks. Moreover, some physics models beyond the SM predict particles with large couplings to b-quarks making b-jets a powerful probe for new physics.

Topological Clusters

Topological cluster is a collection of spatially connected individual calorimeter cell signals. The signals in the cells arise as a response to propagating particles from proton-proton collisions. The formation of topo-clusters is an attempt to extract meaningful signals from the hadronic final states in those collisions. On the other hand, a signal in a cell can also arise due to electronic noise of the cell itself. This undesirable signal constitutes noise in the formation of topo-clusters. Additionally, multiple interactions per bunch crossing or remnant signals from earlier bunch crossings (in-time and out-of-time pile-up, respectively) also constitute noise in the sense that they do not belong to the hadronic final state of the hard collision. The clustering algorithm deployed in ATLAS takes into account these effects and suppresses noise while producing clusters.

For the formation of a topo-cluster a cell signal significance is defined as the ratio of the absolute value of the cell signal to the average cell noise. The cell noise is estimated for each run year and run conditions that influence the pile-up. The energy deposited in the cells is measured on the electromagnetic energy scale (EM scale). This energy scale reconstructs the energy of electrons and photons correctly but underestimates the energy of hadronic particles due to non-compensating character of the calorimeters. The cells with signal significance larger than 4 are the primary seeds. The clusters are formed by a growing-volume algorithm around the primary seeds, also called proto-clusters, by collecting cells neighboring the seed and having signal significance larger than 0. Neighboring cells are those which are directly adjacent to each other if they are in the same calorimeter layer or having an overlap in $\eta - \phi$ space if in different layers. If a connected neighbor has a signal significance larger than 2, the parameter defined as the threshold for growth control, its neighbors are also collected into the proto-cluster. If a connected neighbor is also a primary seed, the two proto-clusters are merged together. If a cell with a signal significance passing the threshold for growth control belongs to two proto-clusters, the proto-clusters are also merged.

This procedure is applied until there is no neighboring cells with signal significance larger than 0 left. The topo-clusters constructed in this way have a core of cells with highly significant signals surrounded by an envelope of less significant signal cells. The inclusion of all cells around a cell with signal significance larger than 2 allows for preserving small signal remnants while keeping the noise suppression feature of the algorithm.

During the topo-cluster formation the absolute value of signal significance is used, which means that cells with negative energy can be primary seeds or be collected into a proto-cluster. The negative cell energy usually arise from electronic noise or from out-of-time pile-up when cell signals from earlier bunch-crossings are at the end of their pulse shapes. The inclusion of cells with negative energy mainly serves as a diagnostic tool for the amount of calorimeter noise introduced by pile-up in the given event. Also, clusters seeded by negative energy cells usually have negative total energy due to the dominance of the seed cell and energy correlations between the neighboring cells. Finally, topo-clusters with negative energy can be used as an average global cancellation of other, positive energy, topo-clusters also introduced by out-of-time pile-up.

The procedure described above provides topologically connected proto-clusters with significant signals and suppresses noise from cells with insignificant signals. However, in this way the inner structure of the proto-clusters is ignored although inside each of them structures of local energy maximum can arise from particles in near proximity. For this reason the proto-clusters are further split into smaller clusters if they contain two or more local maxima. After this step the constructed clusters are the topo-clusters used in subsequent reconstruction of physics objects.

Local Hadronic Calibration

Topological clusters are initially calibrated at the electromagnetic scale. This scale has non-linear response to hadronic particles and therefore the energy scale and resolution of intrinsically hadronic objects such as jets and hadronically decaying tau leptons would have a deteriorated energy measurement. The energy calibration called local hadronic calibration (so called LC energy scale) can be applied to topo-clusters when they are used in the reconstruction of certain physics objects. This energy calibration is applied to topo-clusters based on their energy and shapes and it is intended to correct for the non-compensating character of the calorimeter response to hadrons, accidental signal losses due to the clustering method, and

energy loss in inactive material. All calibrations and corrections are based on MC simulation of single pions with various energies and in all calorimeter regions. Local hadronic calibration is applied to topo-clusters used for tau lepton reconstruction, as well as *LC-topo* jets and calorimeter based missing transverse energy soft term (the last two objects are not used in the analysis described in this thesis).

Jet Reconstruction

Jets are reconstructed with the anti-k_T algorithm [90] using topological clusters as the main building blocks. The topo-clusters are calibrated at the EM scale and therefore these jets in ATLAS are called *EM-topo* jets. The reconstruction procedure is implemented in the FastJet [91] software package.

ATLAS reconstructs jets with various radius parameters but the most commonly used jets are those with $R = 0.4$. Only positive energy topo-clusters are considered in the jet reconstruction. Additionally, tracks in the inner detector are used for jet energy calibration and tracks in the muon spectrometer serve as a proxy for the uncaptured jet energy. Tracks are associated to jets based on the ΔR separation; if a track satisfy the association criteria with more than one jet, it is assigned to a jet with smallest ΔR.

Anti-k_T is an inclusive jet finding algorithm belonging to a broader class of sequential recombination algorithms. These algorithms are parameterized by the power of the energy scale in the distance measure and the anti-k_T in particular is characterized by the negative power. The algorithm is essentially useful for its properties of infrared and collinear safety. Additionally, this algorithm constructs jets with regular boundaries, a property known as soft-resilience. It is to be contrasted with other, soft-adaptable, algorithms where soft radiation invokes irregularities in jet boundaries.

For the construction of jets, distance parameters between two topo-clusters and a topo-cluster with the beam-line are defined:

$$d_{ij} = min(k_{Ti}^{2p}, k_{Tj}^{2p}) \frac{\Delta_{ij}^2}{R^2}, \tag{3.4.1}$$

$$d_{iB} = k_{Ti}^{2p}, \tag{3.4.2}$$

where $\Delta_{ij}^2 = (y_i - y_j)^2 + (\phi_i - \phi_j)^2$ and k_{Ti}, y_i and ϕ_i are transverse momentum, rapidity and azimuthal angle of particle i. The algorithm proceeds by finding the smallest distance between two topo-clusters and merging them. If the smallest

distance is d_{iB}, then the particle i is taken to be a jet itself. The merging of clusters is continued until all of them are clustered into jets.

The distance between two topo-clusters is characterized not only by their geometrical distance Δ_{ij}^2 but also by their energy scales. This distance between a hard and a soft objects is therefore smaller than the distance between two soft objects for the same value of the geometrical separation. For this reason jets are clustered around high-energy topo-clusters and soft particles are clustered with the hard ones long before they are clustered with each other. If a hard topo-cluster has no other hard neighbors within a distance $2R$ then it will simply gather soft particles around it into a cone-shaped cluster of size R. On the other hand, hard particles in close proximity will generally result in jets that have their boundaries shaped properly. This is a very desirable feature of the algorithm that it produces jets which are soft-resilient with respect to soft particles but adaptable with respect to hard particles.

Jet Energy Scale

Jet energy scale (JES) calibration procedure restores the full four momentum of jets to that of the truth jets reconstructed at the particle level [92]. The procedure passes a chain of corrections using MC simulation, mitigation of pile-up effects and other. First, the origin correction recalculates the four-momentum of jets to point to the hard-scatter vertex rather than the center of the detector thus improving η resolution. Second, pile-up correction removes the redundant energy due to in-time and out-of-time pile-up. Then, the absolute JES calibration corrects the jet four-momentum to the particle-level energy scale as derived in MC simulation. Then, global sequential calibration uses additional variables from the calorimeters, inner detector and muon spectrometer to further improve JES. Finally, a residual in-situ calibration is performed using well-measured reference objects.

Jet Vertex Tagger

The Jet Vertex Tagger algorithm (JVT) [93] uses tracker information in a multivariate discriminant to identify jets which do not originate from the hard-scatter vertex, i.e. pile-up jets. The algorithm uses two variables in a two-dimensional likelihood function.

The first variable is the corrected jet vertex fraction (corrJVF), similar to the jet vertex fraction (JVF) but adapted to take the number of reconstructed vertices

into account due to increased pile-up in Run 2. JVF is a variable that relates tracks originating from a primary vertex to tracks associated with a jet, and it is calculated for every combination of PV tracks and jet tracks. More precisely, JVF is the ratio of the scalar sum of transverse momenta of tracks, which originate from a given PV and are matched to the jet, to the scalar sum of transverse momenta of all tracks associated with the jet. It is clearly seen that JVF has a value of 1 if all tracks associated with a jet originate from a single primary vertex. On the other hand, JVF values close to zero indicate that a jet does not originate from a particular primary vertex and therefore is useful for identifying pile-up jets that do not originate from hard-scatter vertex.

The second variable ($R_{p_{\mathrm{T}}}$) measures the fraction of the total sum of transverse momenta of tracks associated to the jet and originating from the hard-scatter vertex to the total calibrated jet transverse momentum. For pile-up jets this variable give small values because tracks from the hard-scatter vertex rarely contributes to these jets. For hard-scatter jets $R_{p_{\mathrm{T}}}$ has the meaning of a charged p_{T} fraction and it tends to have larger values than for the pile-up jets.

The JVT tagger has three defined working points for jets with $|\eta| < 2.4$ and $20 < p_{\mathrm{T}} < 60\,\mathrm{GeV}$ which have efficiencies of about 85%, 92% and 97% and those correspond to increasing pile-up jet efficiency of about 0.4%, 1% and 3%.

Jet Flavor Tagging

ATLAS uses the MV2c10 multivariate algorithm [94] based on boosted decision trees (BDT). The algorithm exploits the relatively long lifetime of a b-hadron of the order 1.5 ps ($c\tau \approx 450\,\mu$m). A b-hadron with $p_{\mathrm{T}} = 50\,\mathrm{GeV}$ travels a significant distance in the transverse direction, on average 3 mm, before decaying and consequently leading to topologies with displaced vertices. Tracks from b-hadron decays tend to have large impact parameters which can be distinguished from other tracks associated with a primary vertex. The insertable B-layer being so close to the beam line has a significant impact on the b-tagging performance.

The input variables for the tagging algorithm comprise the likelihood-based combination of the longitudinal and transverse impact parameter significances, the presence of a secondary vertex. Additionally used is the reconstruction of the b-hadron decay chain using Kalman filter to search for a common direction connecting the primary vertex to secondary bottom quark and tertiary charm quark decay vertices. Jet p_{T} and jet η are included in the BDT training to take advantage

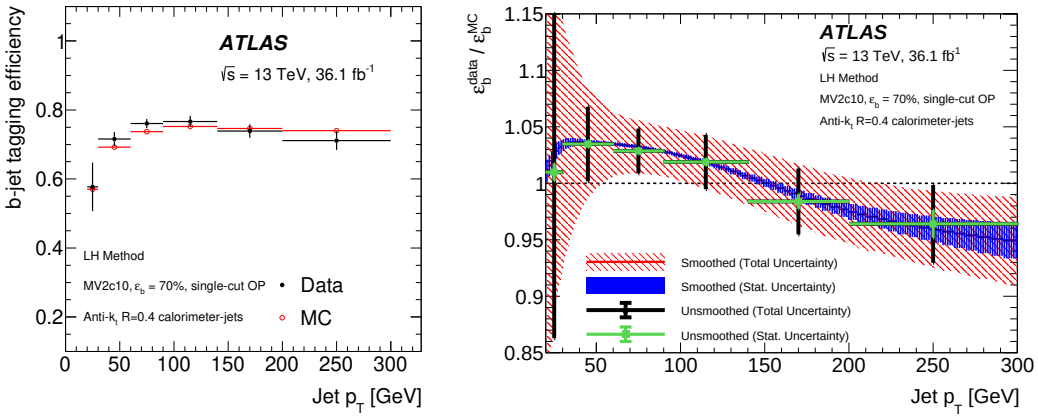

Figure 3.3: (left) The b-tagging efficiency of the 70% working point measured in data and simulation and (right) data-to-simulation scale factors [94].

of correlations with other variables. The BDT training is performed by assigning b-jets as signal and c-jets and light-flavor jets as background.

The b-tagging selection is provided for jets with $|\eta| < 2.5$ and $p_T > 20\,\text{GeV}$ and has four pre-defined working points with different efficiencies for physics analyses. The four working points correspond to efficiencies of 60%, 70%, 77% and 85% which also correspond to the decreasing rejection power of mis-identified b-jets. The performance of the tagging algorithm was measured using $t\bar{t}$ events in data and MC simulation. The measured efficiencies of the 70% working point are shown in Fig 3.3 together with the derived scale-factors for the use in physics analyses.

3.5 Missing Transverse Energy

The missing transverse energy ($E_{\text{T}}^{\text{miss}}$) is the negative vectorial sum of the transverse momenta of objects associated with a hard-scatter primary vertex. It serves the purpose of an experimental proxy for the energy of particles not detected. Only the transverse part of the missing energy can be reconstructed because the conservation of energy cannot be used in the longitudinal direction. The partons participating in the hard interaction have unequal longitudinal momenta and therefore the laboratory frame of reference does not coincide with partons' center-of-mass frame of reference. On the other hand, transverse motion of the partons should be minute compared to the energy scale of the hard interaction.

An event with missing energy is primarily expected from neutrinos which

interact only weekly and therefore propagate through the detector without leaving a trace. For example, $E_{\mathrm{T}}^{\mathrm{miss}}$ can be used in the estimation of the W boson mass in the leptonic decay mode. Moreover, other particles predicted in models beyond the SM could be escaping the detector unnoticed too and a large value of $E_{\mathrm{T}}^{\mathrm{miss}}$ serves as an experimental signature for a search of such particles.

The missing transverse energy is a complex object calculated from other objects associated with the hard-scatter primary vertex and consequently the limitations of measurements of those objects influence it. The momentum resolution of reconstructed particles and tracks not associated to any object propagate to the resolution of $E_{\mathrm{T}}^{\mathrm{miss}}$. Additionally, limitations of detector acceptance and undesirable signals from in-time and out-of-time pile-up biases the measurement of $E_{\mathrm{T}}^{\mathrm{miss}}$. Consequently, hard-scatter events with no genuine missing energy can have non-zero value of $E_{\mathrm{T}}^{\mathrm{miss}}$. In order to measure $E_{\mathrm{T}}^{\mathrm{miss}}$ precisely and accurately, all detector subsystems must be used and unambiguous representation of the hard interaction must be defined.

This section describes how missing energy is represented in the ATLAS experiment, and which objects and in what order enter $E_{\mathrm{T}}^{\mathrm{miss}}$ calculation.

$\boldsymbol{E}_{\mathbf{T}}^{\mathbf{miss}}$ Reconstruction

The missing transverse energy is reconstructed from two parts [95]. The first contributing part is associated with hard-scatter signals consisting of fully reconstructed and calibrated hard objects, such as electrons, photons, muons, taus and jets. The second contributing part to the $E_{\mathrm{T}}^{\mathrm{miss}}$ arises from soft-scatter signals comprising reconstructed tracks that are associated to the hard-scatter primary vertex but not to any hard object.

The hard objects used in $E_{\mathrm{T}}^{\mathrm{miss}}$ calculation are reconstructed, identified and fully calibrated individually and the same signal can be reconstructed as multiple objects. To avoid a double inclusion of a signal an explicit signal ambiguity resolution procedure is applied. In general, objects entering the $E_{\mathrm{T}}^{\mathrm{miss}}$ calculation have different priority with electrons having the highest priority, then photons followed by tau leptons and finally jets. Muons are reconstructed from ID and MS tracks and therefore in principal they do not share signals with other objects. The signal ambiguity resolution procedure ensures that no signal would be included more than once and that includes treatment of muon energy deposits in the calorimeters, partial overlap of jets and accidental jet reconstruction from pile-up.

The soft objects used in the $E_{\mathrm{T}}^{\mathrm{miss}}$ calculation represent soft particles from the hard scatter but which are not associated to any hard object. These signal contributions are based on reconstructed tracks which are matched to the hard-scatter vertex. This track-based $E_{\mathrm{T}}^{\mathrm{miss}}$ soft-term is largely insensitive to pile-up effects due to the proper track association to vertices. However, it does not include contributions from neutral soft particles.

The event observables resulting from this procedure are a 2-dimensional vector of the missing transverses energy, its absolute size and its direction in the transverse plane given by azimuthal angle ϕ. Additionally, a scalar sum of all terms entering the $E_{\mathrm{T}}^{\mathrm{miss}}$ calculation ($\sum E_T$) provides the overall energy scale of the event.

3.6 Taus

Tau leptons have too short lifetime to reach the active parts of the detector before they decay and consequently they can only be detected through their decay products. In the ATLAS detector tau lepton candidates can be reconstructed and identified provided the lepton decays hadronically. Leptonically decaying tau leptons (so called leptonic taus) are not distinguished from the production of electrons or muons in other processes although the leptons from tau decays can have slightly larger impact parameters. Hadronically decaying tau leptons (so called hadronic taus) are reconstructed using anti-k_{T} jet seeds, matched to tracks in the inner detector. Hadronic taus look much like jets but on average have some distinguishing features which can be exploited in the identification. They are identified using a BDT multivariate algorithm based on tracking information and on shower shapes in the calorimeters.

Tau reconstruction

The visible decay products of a hadronic tau lepton are denoted by $\tau_{\text{had-vis}}$ which explicitly corresponds to charged and neutral hadrons but not to the neutrino. Since the hadrons from the tau decay are collimated and resemble low-multiplicity jets, tau candidates are seeded by jets reconstructed with the anti-k_{T} algorithm with the radius parameter $R = 0.4$ using topo-clusters calibrated at the LC scale, as described in section 3.4. Jet seeds are additionally required to have $p_{\mathrm{T}} > 10\,\mathrm{GeV}$ and $|\eta| < 1.37$ or $1.52 < |\eta| < 2.5$.

The tau vertex (TV) [96] is defined as the primary vertex with largest frac-

tion of transverse momenta of tracks associated with the jet within $\Delta R < 0.2$. The TV is used to determine $\tau_{\text{had-vis}}$ direction and to build coordinate system in which identification variables are calculated. Tracks associated to the TV must pass quality criteria based on the number of hits and impact parameters and have $p_{\text{T}} > 1\,\text{GeV}$. In particular, tracks must have at least two hits in the pixel detector and at least seven precision hits in total. The requirements on impact parameter measured relatively to the TV are $|d_0| < 1\,\text{mm}$ and $|\Delta z_0 \sin\theta| < 1.5\,\text{mm}$. Then, the tracks are assigned to the core ($\Delta R < 0.2$) or isolation ($0.2 < \Delta R < 0.4$) regions around the tau candidate. The (η, ϕ) coordinates are calculated using vectorial sum of topo-clusters within $\Delta R < 0.2$ around the jet barycenter and using the TV as the origin. The mass of the tau candidate is set to zero.

The number of associated core tracks and the efficiency as a function of the $\tau_{\text{had-vis}}$ p_{T} in the reconstruction of simulated tau leptons are shown in Fig. 3.4. While the correct jet seed finding is almost always fully efficient, the dominant role of reconstruction efficiency is played by the track and vertex selections. Overestimation of the number of associated tracks usually arise from photon conversion where the photon itself is produced in π^0 decay, while underestimation is mostly due to tracking inefficiency because of hadronic interactions with detector material. The reconstruction efficiency for 1-prong taus is almost constant in p_{T} but a slow decrease is seen at very high p_{T}. Very energetic tau leptons may decay far from the primary vertex due to time dilation and therefore fail the requirements on impact parameters or even decay beyond the first pixel layer and fail the hits requirement. Additionally, energetic electrons from photon conversion have higher probability to be mis-identified as charged pions and might be assigned as genuine hadron tracks from tau decays. For 3-prong tau decays the inefficiency at low p_{T} is a result of the minimum transverse momentum requirement of tracks, and at high p_{T} is due to collimation of energetic tracks which can not be individually resolved in the tracker. The tau lepton reconstruction inefficiency at high p_{T} plays an important role in the searches for high mass resonances decaying to tau leptons and generally results in the loss of sensitivity for increasing resonance masses.

More than 90% of hadronic tau decays proceed through five dominant decay modes. The Tau Particle Flow (TPF) algorithm [97] is an attempt to categorize the reconstructed tau candidates into one of the five modes. The algorithm is designed to reconstruct individual charged and neutral hadrons from hadronic tau decays. Charged hadrons are reconstructed using the tracking system while the neutral hadrons are reconstructed from energy depositions in the calorimeters. The

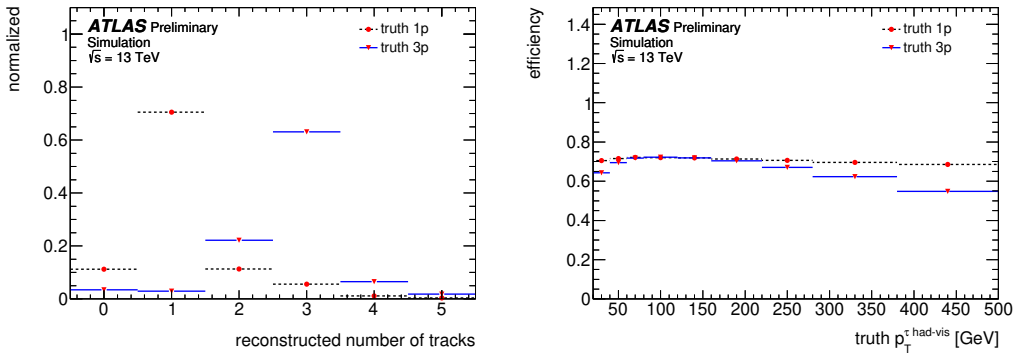

Figure 3.4: Tau lepton reconstruction performance presented as (left) the number of associated core tracks in the reconstruction of hadronically decaying tau leptons for truth 1-prong and 3-prong tau decays, and (right) reconstruction efficiency as a function of the $\tau_{\text{had-vis}}$ p_{T} [96].

main challenge is to disentangle calorimeter energy depositions that are produced by charged and by neutral hadrons. In addition to the classification goal of the algorithm, it provides a superior momentum measurement of charged pions in the tracking system, hence it is capable of improving tau energy measurement.

Tau Energy Calibration

The calorimeter clusters associated with the $\tau_{\text{had-vis}}$ are calibrated with the LC algorithm which accounts for the non-compensating character of the ATLAS calorimeters and for the energy deposited outside the reconstructed clusters and in non-sensitive regions of the calorimeters. However, this particular calibration is not optimized for hadronic tau decays which are known to only have specific numbers and types of hadrons. Thus an additional energy correction is needed to bring the observed energy response closer to the true visible energy of the $\tau_{\text{had-vis}}$.

The baseline correction [98] is derived from simulation comparing reconstructed energy with true energy of the $\tau_{\text{had-vis}}$. This correction is expressed with a formula

$$E_{\text{calib}} = \frac{E_{\text{LC}} - E_{\text{pileup}}}{\mathcal{R}(E_{\text{LC}} - E_{\text{pileup}}, |\eta|, n_{\text{p}})}. \tag{3.6.1}$$

Here E_{LC} is the sum of topo-cluster energy within $\Delta R < 0.2$ of the tau candidate. The reconstructed energy has a component subtracted from it, the pile-up correction E_{pileup}, which takes into account the energy deposited by particles from

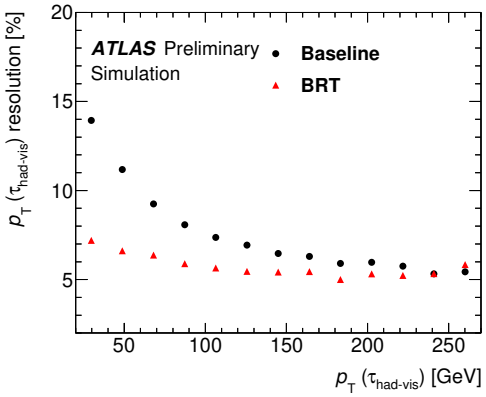

Figure 3.5: Tau energy resolution with the baseline and with the BRT calibrations applied [98].

multiple pp interactions and it increases linearly with the number of primary vertices. The pile-up correction is a linear function of the number of vertices in the event and depends on pseudorapidity and number of prongs. The detector response calibration, $\mathcal{R}$, is extracted as the Gaussian mean of the $(E_{\mathrm{LC}} - E_{\mathrm{pileup}})/E^{\mathrm{vis}}_{\mathrm{true}}$ distribution, where $E^{\mathrm{vis}}_{\mathrm{true}}$ is the energy of generated tau decay products, including final state radiation but excluding the energy of neutrinos. This correction is derived separately for 1-prong and 3-prong candidates, indicated by the variable n_{p}. With this basic correction applied the energy resolution ranges from 15% at transverse momentum of $\tau_{\text{had-vis}}$ of 20 GeV to 5% at 250 GeV.

During Run 2 ATLAS implemented a combined energy calibration which uses information from both baseline and Tau Particle Flow energy calibrations in a multivariate analysis, called boosted regression tree (BRT), together with additional information from the tracking system and calorimeters. The BRT energy calibration provides tau energy resolution of 7% at 20 GeV and of 5% at 250 GeV (this is the region where baseline calibration is more precise). Comparison of tau energy resolution between the baseline and BRT calibrations is shown in Fig. 3.5.

Tau identification

Reconstructed tau candidates include large background contamination from quark- and gluon-initiated jets. The tau identification algorithm is designed to suppress tau candidates arising from background jets. The algorithm combines shower shape and tracking information in a multivariate BDT algorithm. The input variables for

the BDT training are listed in Table 3.1 and explained in the following:

- Central energy fraction (f_{cent}) is the fraction of the transverse energy deposited in the calorimeters within $\Delta R < 0.1$ with respect to the total energy deposited within $\Delta R < 0.2$ around the $\tau_{\text{had-vis}}$ candidate. For this, topo-clusters are calibrated at the EM energy scale.

- Leading track momentum fraction ($f^{-1}_{\text{leadtrack}}$) is the ratio of the transverse energy in the calorimeters within the core region, calibrated at the EM energy scale, to the transverse momentum of the highest-p_{T} track in the core region.

- Track radius ($R^{0.2}_{\text{track}}$) is the p_{T} weighted ΔR distance of the tracks in the core region.

- Leading track IP significance ($S_{\text{leadtrack}}$) is the $|d_0|/\sigma_{d_0}$ of the highest-p_{T} track in the core region.

- Fraction of tracks p_{T} in the isolation region ($f^{\text{track}}_{\text{iso}}$) is the ratio of the scalar sum of the transverse momenta of tracks in the isolation region to that of all associated tracks.

- Maximum ΔR (ΔR_{max}) is the maximum distance in ΔR between the $\tau_{\text{had-vis}}$ direction and a track in the core region.

- Transverse flight path significance ($S^{\text{flight}}_{\text{T}}$) is the decay length of the secondary vertex in the transverse direction relative to the TV, divided by its uncertainty.

- Track mass (m_{track}) is the invariant mass of all associated tracks.

- Fraction of EM energy from charged pions ($f^{\text{track}-\text{HAD}}_{\text{EM}}$) is the fraction of electromagnetic energy of tracks in the core region. The numerator is defined as the difference between the sum of transverse momentum of tracks in the core region and the sum of clustered energy deposition in the hadronic calorimeter, including the third EM calorimeter layer. The denominator is defined as the sum of clustered energy deposition in the two front EM calorimeter layers and the presampler (called the electromagnetic part of total energy). Clusters are calibrated at the LC energy scale.

Table 3.1: List of variables used in the tau identification algorithm. Adapted from [96]

Variable	1-prong	3-prong
f_{cent}	•	•
$f^{-1}_{\text{leadtrack}}$	•	•
$R^{0.2}_{\text{track}}$	•	•
$S_{\text{leadtrack}}$	•	
$f^{\text{track}}_{\text{iso}}$	•	
ΔR_{max}		•
$S^{\text{flight}}_{\text{T}}$		•
m_{track}		•
$f^{\text{track}-\text{HAD}}_{\text{EM}}$	•	•
$f^{\text{EM}}_{\text{track}}$	•	•
$m_{\text{EM+track}}$	•	•
$p^{\text{EM+track}}_{\text{T}}/p_{\text{T}}$	•	•

- Ratio of EM energy to track momentum ($f^{\text{EM}}_{\text{track}}$) is the ratio of the electromagnetic part of the total energy to the sum of momentum of tracks in the core region.

- Track-plus-EM-system mass ($m_{\text{EM+track}}$) is the invariant mass of the system composed of the four-momentum of tracks in the core region and up to two most energetic topo-clusters from the electromagnetic part of the total energy assuming zero mass of the topo-clusters and using its seed direction.

- Ratio of track-plus-EM-system to p_{T} ($p^{\text{EM+track}}_{\text{T}}/p_{\text{T}}$) ratio of the transverse momentum of the track and calorimeter system, as for the previous variable, to the calorimeter-only measurement of $\tau_{\text{had-vis}}$ p_{T}.

An example of one input variable, the central energy fraction, is shown in Fig. 3.6. The BDT is trained on simulated $Z \to \tau\tau$ samples for signal and di-jet samples from data for background. The input variables are corrected such that the

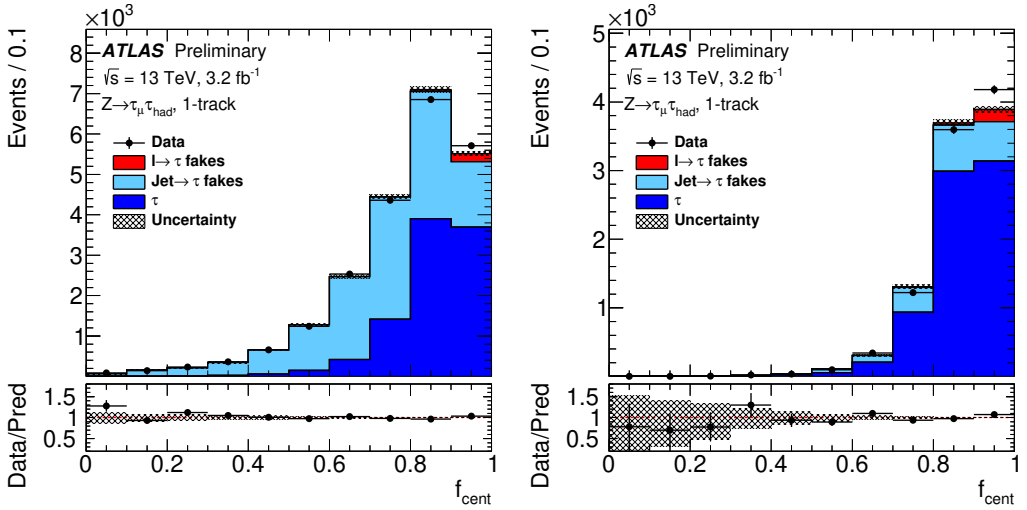

Figure 3.6: Distributions of the central energy fraction, (f_{cent}), (left) for all tau candidates and (right) for tau candidates passing the "medium" tau identification working point. The distributions are obtained from a tag-and-probe analysis using 2015 data set [98].

mean of their distribution for signal samples is constant as a function of pile-up. This ensures that the identification efficiency does not depend strongly on pile-up. Three working points, "loose", "medium" and "tight" have target efficiencies of 60%, 55%, 45% for 1-prong and 50%, 40%, 30% for 3-prong true tau candidates, respectively.

Electron Discrimination

A large background of hadronically decaying tau lepton candidates come from electrons which are mistakenly recognized as single charged hadrons and therefore are reconstructed as 1-prong tau candidates. A dedicated electron identification likelihood working point called "very loose" is used for vetoing tau candidates. Tau candidates are rejected if they are reconstructed within $\Delta R < 0.4$ of an electron candidate satisfying the "very loose" identification working point. This electron likelihood working point is tuned to provide 95% efficiency for true tau candidates.

The electron mis-identification probability is defined as the probability for an electron to satisfy both the tau identification and the electron discrimination algorithm requirements. This probability ranges between 0.5% and 2.5% across the η scope covered by the tracker.

Chapter 4

Search For Heavy Neutral MSSM Higgs Bosons

A search for the heavy neutral MSSM Higgs bosons, H and A, in the $\tau_{\text{lep}}\tau_{\text{had}}$ decay channel is presented in this chapter. The analysis described here was combined with the $\tau_{\text{had}}\tau_{\text{had}}$ channel analysis and the results were published in [2]. The results indicate that the $\tau_{\text{lep}}\tau_{\text{had}}$ channel is more sensitive to the Higgs bosons with masses below $\approx 600\,\text{GeV}$ while the $\tau_{\text{had}}\tau_{\text{had}}$ channel is more sensitive at higher masses. Compared to the $\tau_{\text{lep}}\tau_{\text{had}}$ channel, the $\tau_{\text{had}}\tau_{\text{had}}$ channel loses sensitivity at low masses due to high momentum threshold of the tau trigger, but gains sensitivity at high masses due to smaller background contamination. Compared to the published analysis, the one described here has an improved fake tau background estimation (Section 4.3).

In this chapter the analysis is delineated in detail starting with the event selection and the collected data. Following that, simulated Monte Carlo samples are summarized. Once the data on hand is known, construction of signal and background template model is presented, followed by statistical fitting procedure and the search results. Finally, the results are interpreted in two MSSM benchmark scenarios, which are described in Section 1.8.

4.1 Event Selection

The decay channel under investigation suggests an event selection that ensures high signal acceptance and reduces background contamination at the same time. The necessary target is two objects: a hadronically decaying tau lepton and a leptoni-

cally decaying tau lepton. For hadronically decaying tau leptons ATLAS provides a dedicated identification algorithm (Section 3.6). For leptonically decaying tau leptons no attempt is made to distinguish the outgoing charged lepton from prompt leptons of other particle decays. In the leptonic tau decay the decay products comprise two neutrinos and an electron or a muon, and therefore lepton identification and isolation requirements are enough to ensure high signal efficiency. In this analysis "lepton" refers to either an electron or a muon with an implicit meaning that they arise from a leptonic tau decay denoted by τ_e and τ_μ or collectively as τ_{lep}. Similarly, "tau" (or "tau lepton") refers to one observed in the hadronic decay mode, unless stated otherwise. This tau lepton is denoted by τ_{had} with an implicit meaning that such object is reconstructed from the visible decay products, denoted by $\tau_{\text{had-vis}}$.

This section describes the event selection in the analysis. Object definitions are described in Chapter 3 and selection efficiencies are taken from references therein.

4.1.1 Event Triggering

Since a lepton is present in all signal events, the data are collected using unprescaled single lepton triggers [76]. Electron triggers with transverse momentum thresholds of 24, 60 and 120 GeV were used for collecting data in 2015 and with thresholds of 26, 60 and 140 GeV for the 2016 data. The three electron triggers used in 2015 have a likelihood based identification requirement of "medium", "medium" and "loose" working points, respectively. Although the 24 and 60 GeV threshold triggers have the same identification criteria, the 60 GeV trigger does not have calorimeter isolation requirement at L1. In 2016 the three triggers are required to satisfy "tight", "medium" and "loose" likelihood based identification requirements, respectively. Additionally, the 26 GeV threshold trigger is required to satisfy an isolation requirement.

Muon triggers with transverse momentum thresholds of 20 and 50 GeV were used for collecting data in 2015 and with thresholds of 26 and 50 GeV for 2016 data. The lower threshold muon triggers have an isolation requirement of "loose" working point.

Both electron and muon triggers have tighter requirements in 2016 due to the increased instantaneous luminosity. During the 2015 data-taking a maximum instantaneous luminosity of $5.2 \times 10^{33}\,\text{cm}^{-2}\text{s}^{-1}$ was reached, while in 2016 this

number increased to $1.38 \times 10^{34}\,\mathrm{cm}^{-2}\mathrm{s}^{-1}$.

According to the performance measurements of the ATLAS Trigger System in 2015, electron triggers are 90% efficient in the whole η range covered by the inner detector, except in the transition region between the barrel and end-cap calorimeters. The trigger efficiency with respect to electron momentum has a sharp turn-on at the low p_{T} threshold and reaches 95% efficiency at around 50 GeV. Muon triggers are 70% efficient in the barrel region and 90% in the end-caps.

4.1.2 Data Quality

The collected data corresponds to an integrated luminosity of $36.1\,\mathrm{fb}^{-1}$. Selected events must satisfy criteria designed to reduce backgrounds of non-collision origin. The main sources of non-collision backgrounds are beam-induced events, cosmic rays and calorimeter noise [99]. The beam-induced background arise due to proton losses upstream of the interaction point. Secondary cascades are caused by these protons producing muons which can be reconstructed as fake jets. Cosmic rays, mostly muons, produced in the atmosphere can overlap with collision events. Calorimeter noise can manifest in isolated pathological cells or on a larger scale as a coherent noise. Permanently or sporadically noisy cells are masked prior to jet and missing transverse energy reconstruction. The jet selection criteria are designed to suppress these kinds of background to a negligible level. Selected events must also contain at least one primary vertex.

4.1.3 Event Pre-selection

The triggered events are investigated and some initial requirements are placed on the reconstructed objects, a procedure generally known as pre-selection. The electron candidates are required to pass the "loose" likelihood-based identification requirement, to have a transverse momentum $p_{\mathrm{T}} > 15\,\mathrm{GeV}$ and to be in the fiducial volume of the inner detector, $|\eta| < 2.47$. The transition region between the barrel and end-cap calorimeters, $1.37 < |\eta| < 1.52$, is excluded. The muon candidates are required to be of the combined type, pass the "loose" muon identification requirement and have transverse momentum $p_{\mathrm{T}} > 7\,\mathrm{GeV}$ and pseudorapidity $|\eta| < 2.5$. All leptons are required to have looser selection requirements than those which are used in the triggers in order to carry out an unbiased overlap-removal procedure (see below).

EM-Topo anti-k_{T} jets are required to pass a "loose" selection criteria which

Table 4.1: List of object pre-selection requirements.

Cut name \ Channel	Electron	Muon
Lepton momentum	$p_{\mathrm{T}}^{\tau_e} > 15\,\mathrm{GeV}$	$p_{\mathrm{T}}^{\tau_\mu} > 7\,\mathrm{GeV}$
Lepton pseudorapidity	$\lvert\eta\rvert < 2.47$, exclude $1.37 < \lvert\eta\rvert < 1.52$	$\lvert\eta\rvert < 2.5$
Lepton identification	"loose"	
Tau momentum	$p_{\mathrm{T}}^{\tau_{\mathrm{had}}} > 25\,\mathrm{GeV}$	
Tau pseudorapidity	$\lvert\eta\rvert < 2.5$, exclude $1.37 < \lvert\eta\rvert < 1.52$	
Tau tracks	1 or 3 core tracks	
Tau electric charge	± 1	
Jet momentum	$p_{\mathrm{T}}^{\mathrm{jet}} > 20\,\mathrm{GeV}$	
Jet pseudorapidity	$\lvert\eta\rvert < 2.5$	

corresponds to 99.5% efficiency for 20 GeV jets and 99.9% efficiency for 100 GeV jets [99]. They are also required to have $p_{\mathrm{T}} > 20\,\mathrm{GeV}$ and $|\eta| < 2.5$. The jet vertex tagger (JVT) algorithm is used for jets with $p_{\mathrm{T}} < 60\,\mathrm{GeV}$ and $|\eta| < 2.4$ which reduces the effect of pile-up. The JVT cut corresponds to the average of 92% efficiency to select jets originating from the hard-scatter vertex.

Reconstructed τ_{had} candidates must have a transverse momentum $p_{\mathrm{T}} > 25\,\mathrm{GeV}$ and pseudorapidity $|\eta| < 2.5$ but excluding the transition region between the barrel and the end-cap calorimeters, $1.37 < |\eta| < 1.52$. They must also have one or three associated core tracks and have an electric charge of ± 1. The highest transverse momentum τ_{had} candidate is then selected for a further consideration and all remaining candidates are considered as jets.

Reconstructed and pre-selected objects that have geometric overlap based on ΔR are removed by the following priority. Jets within a $\Delta R = 0.2$ cone of the selected tau candidate are excluded. Jets within a $\Delta R = 0.4$ cone of an electron or muon are excluded. Selected tau candidate within a $\Delta R = 0.2$ cone of an electron or muon is excluded. Electron candidates within a $\Delta R = 0.2$ cone of a muon candidate are excluded.

The complete list of pre-selection requirements is summarized in Table 4.1.

4.1.4 Event Selection and Categorization

After the overlap removal procedure the events are investigated further and additional requirements on the remaining objects are set. The event selection presented in this section is formed by comparing simulated signal and background samples, while event pre-selection presented in the previous section is formed from recommendations by ATLAS Combined Performance working groups.

Events with more than one lepton candidate which pass the "loose" identification criteria are vetoed. The selected electron or muon must then have $p_{\mathrm{T}} > 30\,\mathrm{GeV}$ and pass the "medium" identification requirement. For muons this corresponds to around $97 - 99\%$ efficiency except in the poorly instrumented region $|\eta| < 0.1$ of the muon spectrometer, where the efficiency drops significantly. For the electron candidate this identification criteria corresponds to 90% efficiency at 30 GeV and reaches 95% efficiency at 60 GeV. The selected lepton must be geometrically matched to the object that triggered the event. Finally, the lepton must pass the efficiency-targeted type of isolation requirement at the Gradient operating point. For both lepton flavors this requirement is 90% efficient at a transverse energy of 25 GeV and 99% at 60 GeV.

The BDT identification requirement is then applied to the selected τ_{had} candidate. The Signal Region requires the "medium" working point quality τ_{had} candidate but other quality candidates are also considered in control regions. The "medium" quality tau lepton has about 55% and 40% signal efficiencies for 1-prong and 3-prong tau candidates, respectively. An additional dedicated likelihood-based veto is used to reduce the number of electrons mis-identified as taus. This veto has 95% signal efficiency and a background rejection between 20 and 200, depending on the pseudorapidity of the tau candidate. Additionally, the identified tau candidate must have $|\eta| < 2.3$ to further reduce background from mis-identified electrons.

In the Signal Region the selected tau and lepton must have opposite electric charges. The lepton and tau are expected to propagate in different directions in the transverse plane and therefore a cut on angular separation in the transverse plane is applied, $\Delta\phi^{\tau_{\mathrm{had}},\tau_{\mathrm{lep}}} > 2.4$. There is no particular requirement on the missing transverse energy $E_{\mathrm{T}}^{\mathrm{miss}}$ but it is used in calculating other variables and cutting on a particular one. Since the leptonic tau decay has two neutrinos in the final state but the hadronic decay has one neutrino, the direction of the missing transverse energy is expected to be roughly aligned with the lepton. This configuration produces a small value of the transverse mass m_{T} for the lepton and the missing transverse

energy system:

$$m_{\mathrm{T}} = \sqrt{2 \times p_{\mathrm{T}}^{\tau_{\mathrm{lep}}} \times E_{\mathrm{T}}^{\mathrm{miss}} \times (1 - \cos\Delta\phi^{\tau_{\mathrm{lep}}, E_{\mathrm{T}}^{\mathrm{miss}}})}. \tag{4.1.1}$$

A cut on the transverse mass is applied, $m_{\mathrm{T}} < 40\,\mathrm{GeV}$, which retains the majority of signal events while suppressing the large W+*jets* background. The m_{T} variable is a good estimate of the W boson mass and therefore its distribution has a peak at around 80 GeV. The m_{T} cut removes most of this background.

It was observed that tau leptons that are faked by electrons are very poorly modeled in the MC simulation even after the dedicated electron veto. With the current selection a large $Z/\gamma^* \to ee$ background remains where one electron is mis-identified as a tau lepton. For this reason an additional cut is applied in the electron channel. The invariant mass of the lepton and the τ_{had} is called the visible mass,

$$m_{\mathrm{vis}} = \sqrt{(E^{\tau_{\mathrm{lep}}} + E^{\tau_{\mathrm{had}}})^2 - (\vec{p}^{\,\tau_{\mathrm{lep}}} + \vec{p}^{\,\tau_{\mathrm{had}}})^2}. \tag{4.1.2}$$

This mass variable has a peak at around 90 GeV that arises from the Z boson. A mass window $80 < m_{\mathrm{vis}} < 110\,\mathrm{GeV}$ is cut away to remove the $Z/\gamma^* \to ee$ peak.

Events are further split into two categories to increase the sensitivity to the b-associated production mode of the Higgs bosons. The b-tag category is defined as containing at least one b-tagged jet and the b-veto category does not contain a single b-tagged jet. The MV2c10 algorithm for identifying jets containing a b-hadron is used at the 70% efficiency working point. This working point corresponds to the rejection of 12 against c-jets, 55 against tau leptons and 381 against light-flavor jets. This final categorization defines the four signal regions which are considered in the final fit: the electron and muon channels both of which contain the b-tag and b-veto categories. The complete object selection and event categorization is summarized in Table 4.2.

4.1.5 Di-tau Mass Reconstruction

The mass reconstruction of the di-tau system is important for achieving good separation between signal and background. A proper mass variable should produce a signal resonance peak which would provide a large signal over background ratio. However, the mass reconstruction is complicated due to escaping neutrinos. Neutrinos propagate through the detector without leaving a trace and carry away

Table 4.2: List of object selection requirements in the Signal Region.

Cut name \ Channel	Electron	Muon
Lepton veto	Veto events with more than one "loose" lepton	
Lepton momentum	$p_{\mathrm{T}}^{\tau_{\mathrm{lep}}} > 30\,\mathrm{GeV}$	
Lepton identification	"medium"	
Trigger matching	Lepton must match the object that triggered the event	
Lepton isolation	Gradient isolation	
Tau identification	"medium"	
Tau pseudorapidity	$\lvert\eta\rvert < 2.3$	
Back-to-back	$\Delta\phi^{\tau_{\mathrm{had}},\tau_{\mathrm{lep}}} > 2.4$	
Transverse mass	$m_{\mathrm{T}} < 40\,\mathrm{GeV}$	
Visible mass	Exclude $80 < m_{\mathrm{vis}} < 110\,\mathrm{GeV}$	-
b-tag category	At least 1 b-tagged jet	
b-veto category	No b-tagged jets	

momentum which can not be reconstructed. The missing transverse energy provides incomplete information about this momentum and it is used in various di-tau mass reconstruction techniques which approximate the invariant mass of the resonance. For this analysis the total transverse mass is used as the discriminating variable:

$$m_{\mathrm{T}}^{\mathrm{tot}} = \sqrt{(p_{\mathrm{T}}^{\tau_{\mathrm{lep}}} + p_{\mathrm{T}}^{\tau_{\mathrm{had}}} + E_{\mathrm{T}}^{\mathrm{miss}})^2 - (\vec{p}_{\mathrm{T}}^{\,\tau_{\mathrm{lep}}} + \vec{p}_{\mathrm{T}}^{\,\tau_{\mathrm{had}}} + \vec{E}_{\mathrm{T}}^{\mathrm{miss}})^2}. \tag{4.1.3}$$

It is a simple variable to calculate and it has a property useful in searches for high mass resonances. In background events where jets fake tau leptons the total transverse mass gets reconstructed at lower values and therefore leaves smaller background at high mass where the signal is searched for.

Other more sophisticated mass reconstruction techniques exist and they were investigated but did not improve the expected sensitivity. Collinear Approximation has been one of the first propositions to improve the di-tau system mass resolution [100] and Missing Mass Calculator (MMC) [101] is currently in use in the SM Higgs boson measurements in the di-tau channel [102, 103]. Collinear Approximation

assumes that the neutrinos are collinear with the visible decay products of the taus and that the missing transverse energy is only due to the neutrinos. With these assumptions the direction of the neutrinos are approximately known and their momentum can be estimated from the missing transverse energy. This technique works well only for boosted di-tau systems; when the taus are produced back-to-back the momentum carried away by the neutrinos partially cancel out and therefore the mass reconstruction degrades.

Missing Mass Calculator technique incorporates additional information from the general knowledge of the tau decays. The underconstrained system of equations where the unknowns are the neutrino momenta and coordinates is supplemented with probability distributions for the neutrino coordinates. Not all solutions to the underconstrained system are equally likely and therefore the MMC method relies on finding the most probable one based on the visible decay products. The method finds solutions to 99% of all events (the efficiency loss is due to mis-measurements in the missing transverse energy) and improves the di-tau mass resolution to about 16%.

4.2 Monte Carlo Simulation

Monte Carlo (MC) computational algorithm is widely used in high energy particle physics for event simulation. This section describes event samples that were simulated with MC event generators and gives details on the PDF sets, order of accuracy, and cross-section calculations. The event samples and MC generators are summarized in Table 4.3.

4.2.1 Background Samples

Events containing single Z/γ^* bosons and associated jets were generated using Powheg-Box v2 [104, 105] event generator with the CT10 [106] PDF set in the matrix element. The generated events were interfaced with the Pythia 8.186 [107, 108] parton shower model. The AZNLO [109] set of tuned parameters is used with the CTEQ6L1 [110] PDF set for the modeling of non-perturbative effects: parton shower, hadronisation and the underlying event. Photos++ 3.52 [111] is used for QED emissions from electroweak vertices and charged leptons. The Z/γ^*+jets samples were simulated in slices with different off-shell boson masses. Cross sections are calculated based on the results from the 2013 Les Houches workshop [112]. The

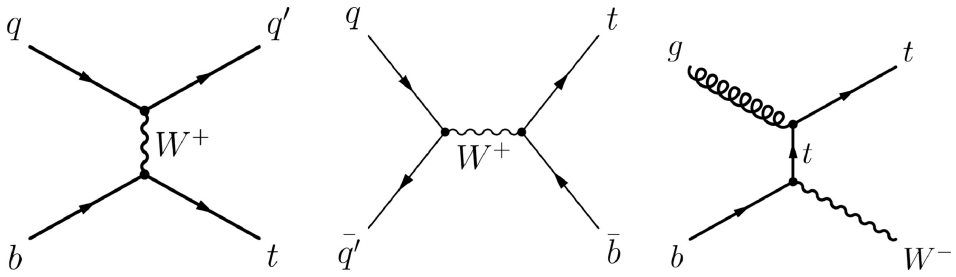

Figure 4.1: Leading order Feynman diagrams of the most relevant single-top production modes at the LHC. From left to right: t-channel, s-channel, Wt-channel.

next-to-next-to-leading-order (NNLO) accuracy in perturbative QCD was obtained with VRAP 0.9 [113] using CT10nnlo [114] set of PDFs. The next-to-leading-order (NLO) accuracy electroweak corrections for high mass Drell Yan were calculated with MCSANC 1.20 [115] using the same PDFs.

In collider experiments top quarks are produced in pairs or singly. $t\bar{t}$ pair production happens through QCD interactions while single-top production is an electroweak phenomenon. Three electroweak single-top-quark processes happen either through a virtual W boson, so called t- and s-channels, or when a bottom quark radiates a W boson, Wt-channel. Feynman diagrams of these processes are shown in Fig 4.1. For the generation of $t\bar{t}$ events, POWHEG-BOX v2 [116] is used with the CT10 PDF set in the matrix element calculations, while single-top-quark events are generated with POWHEG-BOX v1 [117, 118]. This event generator uses the four-flavor scheme for the NLO matrix element calculations together with the fixed four-flavor PDF set CT10f4. For all top-quark processes, the top-quark spin correlations are preserved. For t-channel, top quarks are decayed using MADSPIN [119]. The parton shower, hadronisation and the underlying event are simulated using PYTHIA 6.428 with the CTEQ6L1 PDF set and the corresponding Perugia 2012 [120] set of tuned parameters. The top mass is set to 172.5 GeV. Predictions for $t\bar{t}$ cross sections at NNLO in perturbative QCD, including next-to-next-to-leading-logarithm (NNLL) soft gluon resummation, was prepared using the TOP++2.0 program [121]. The cross section for the Wt-channel was calculated at approximate NNLO QCD and NNLL accuracy [122]. Predictions for the t- and s-channel cross sections at NLO in QCD have been prepared using the HATHOR 2.1 [123] program.

Diboson processes were simulated with the SHERPA 2.1.1 [124] event gen-

erator. The generated events include up to 1 additional parton for the production of ZZ or 0 additional partons for WZ and WW at NLO, and up to 3 partons at LO for all final states. The COMIX [125] matrix element generator and OPENLOOPS [126] scattering amplitudes generator were used in this simulation. The generated events were merged with the Sherpa parton shower algorithm [127] using the ME+PS@NLO prescription [128]. The CT10 PDF set is used in conjunction with dedicated parton shower tuning developed by the Sherpa authors. The event generator cross sections are used in this case (already at NLO).

Events containing W bosons with associated jets were simulated using the SHERPA 2.2.0 [124] event generator with NNPDF30nnlo [129] PDF set. Matrix elements are calculated for up to 2 partons at NLO and 4 partons at LO using COMIX and OPENLOOPS as in the case of Diboson simulation. Non-perturbative effects were simulated as in the Diboson case. The W+*jets* samples were produced with a simplified scale setting prescription in the multi-parton matrix elements to improve the event generation speed. A theory-based re-weighting of the jet multiplicity distribution is applied at event level derived from event generation with the strict scale prescription. The W+*jets* events are normalized with the NNLO QCD cross sections calculated with FEWZ [130].

The EVTGEN 1.2.0 [131] particle decay simulation package was used for the properties of b- and c-hadron decays for all samples except SHERPA. The EVTGEN program is used for consistent heavy flavor particle decays across all the different parton showering simulators as it usually contains more up-to-date particle lifetime and decay tables.

Multiple proton-proton collisions in the same and neighboring bunch crossings were simulated with the soft QCD processes of PYTHIA 8.186 using the A2 [132] set of tuned parameters and the MSTW2008LO [133] PDF set. These simulated minimum-bias (pile-up) events were overlaid on all simulated samples. To simulate the detector response to particles the GEANT 4 toolkit [134] was used, which is implemented in the full ATLAS simulation infrastructure [135]. Every Monte Carlo sample was simulated using these tools, with the exception of the b-associated MSSM Higgs boson signal samples. For the b-associated signal sample the ATLFASTII [135] fast simulation framework was used. The fast simulation is used instead of the full one due to a large fraction of generated events with negative weights which forces to generate larger number of events. The ATLFASTII simulation performs full simulation of the tracker and a parametrized detector response for everything else. Finally, the simulated events were processed with the same

reconstruction software as the data.

4.2.2 Signal Samples

For this analysis two MSSM Higgs production modes, gluon-gluon fusion and in association with b-quarks, have relevant cross-sections. The gluon-gluon fusion Monte Carlo samples were generated with Powheg-Box v2 [136] using CT10 parton distribution functions (PDFs). The b-associated production samples were generated with MadGraph5_aMC@NLO 2.1.2 [137, 138] using CT10nlo_nf4 [139] PDFs. For the parton shower calculation at leading order, underlying event and hadronisation, Pythia 8.210 [140] was used in the gluon-gluon fusion mode together with the AZNLO set of tuned parameters and CTEQ6L1 PDFs. In the b-associated production mode the same generator was used but with the A14 [141] set of tuned parameters and NNPDF2.3LO [142] PDFs. In total 15 mass points between 200 and 2250 GeV were generated for both production modes.

The gluon-gluon fusion sample was generated assuming SM couplings and underestimates the loop contribution from b-quarks at high $\tan\beta$, which can impact the Higgs boson p_{T} spectrum. Generator-level studies indicate this has a negligible impact on the final mass distribution and less than a 10% impact on the signal acceptance, so the effect is neglected.

The production cross sections and branching fractions are taken from the LHC Higgs Cross Section Working Group [143]. For the gluon-gluon fusion process inclusive cross sections are calculated with SusHi [144], which includes NLO supersymmetric-QCD corrections [145, 146], NNLO QCD corrections for the top-quark contribution in the effective theory of a heavy top quark [147, 148] and electroweak effects by light quarks [149]. For the b-associated process the five-flavor NNLO QCD inclusive cross sections are also calculated with SusHi based on bbh@nnlo [150]. The results are combined with the four-flavor NLO QCD calculation [151, 152] to Santander matched cross sections [153]. The masses and mixing (and effective Yukawa couplings) of the Higgs bosons are computed with FeynHiggs [154] for all MSSM scenarios except hMSSM. In the hMSSM branching ratios and Higgs masses are solely computed with HDecay [155, 156]. Branching fractions for all other scenarios are calculated combining the most precise results of HDecay, FeynHiggs and PROPHECY4f [157, 158].

Table 4.3: A summary of Monte Carlo generators and PDF sets used in event simulation. The second label under the MC generator, if present, corresponds to the parton shower model. ME is the acronym of matrix element.

Signal	MC generator	PDF in ME	PDF in non-perturbative
gluon-gluon fusion	POWHEG+PYTHIA8	CT10	CTEQ6L1
b-associated	MADGRAPH5+PYTHIA8	CT10nlo_nf4	NNPDF2.3LO
Background			
Z/γ^*+$jets$	POWHEG+PYTHIA8	CT10	CTEQ6L1
$t\bar{t}$	POWHEG+PYTHIA6	CT10	CTEQ6L1
single-top	POWHEG+PYTHIA6	CT10f4	CTEQ6L1
diboson	SHERPA	CT10	CT10
W+$jets$	SHERPA	NNPDF30nnlo	CT10

4.3 Background Model

The background in the $\tau_{\text{lep}}\tau_{\text{had}}$ channel can be categorized into four exclusive types which contain one of the following: true tau and true lepton; tau faked by a lepton and true lepton; tau faked by a jet and true lepton; tau and lepton faked by jets. The missing combination, true tau and fake lepton, has a negligible rate which was checked in MC simulation.

In the first category both tau and lepton candidates are correctly identified objects; this constitutes background processes which produce real taus and leptons. In the b-veto category it is mostly $Z/\gamma^* \to \tau\tau$ together with a small contribution from top-quark and diboson processes. In the b-tag category it is mostly top-quark processes with a small contribution from $Z/\gamma^* \to \tau\tau$ and a very small contribution from diboson events. This type of background is estimated from Monte Carlo simulation with a requirement that the selected tau would be truth-matched to the corresponding generator-level tau. Corrections derived in dedicated performance studies are applied to correct for trigger, reconstruction, identification and isolation efficiency modeling inaccuracies, as well as momentum scale and resolution mismodeling.

In the second category the selected tau is faked by a lepton but the selected lepton is real. This type of background arise from processes which produce at least two real leptons, one of which fakes the tau. In the b-veto category this background component is large and come from $Z/\gamma^* \to ll$ events. Additionally there is a small

contribution from top-quark and diboson events. In the b-tag category this type of background is very small and comprise top-quark, diboson and $Z/\gamma^* \to ll$ events. In both categories this type of background is estimated from MC simulation with a requirement that the selected tau would be truth-matched to the corresponding generator-level lepton. It was found that in the $\tau_\mu\tau_{\text{had}}$ channel muons faking taus are sufficiently well modeled considering the accuracy of the whole background model. However, in the $\tau_{\text{e}}\tau_{\text{had}}$ channel electrons faking taus were found to be modeled poorly and therefore additional cuts, as described in section 4.1.4, had to be applied to reduce this background to a tolerable level. To improve MC modeling the same corrections, as described above, are applied with an additional correction of electron to tau mis-identification rate.

In order to constrain the shape and normalization of the top-quark background the Top Control Region is defined (Section 4.8) and included in the statistical fitting procedure.

The third and fourth background categories are poorly modeled in MC simulation and therefore a dedicated data-driven method, namely the Fake Factor method, is employed. Fake rates of jets faking taus cannot be simulated accurately due to various reason, most important of which is the necessity to simulate an enormous number of events. This is due to the smallness of the fake rates and due to the fact that such events have values of the variables in the tails of the variables' distributions employed in the tau identification algorithm. The reason to measure the contributions of the third and fourth background categories separately is due to the fake rate dependence on jet composition. Background contribution in which the selected tau is faked by a jet but the lepton is real mostly come from W+$jets$ events in the b-veto category and from W+$jets$ and top-quark events in the b-tag category. Additionally there is a small contribution from Z/γ^*+$jets$ and diboson events in which the lepton is genuine but a jet fakes the tau. This background component is called "W/Top fakes" throughout the thesis. The background in which both tau and lepton are faked by jets arise from QCD multi-jet events. Different combinations of jet types produced in these different processes result in different fake rates which should be measured separately. Compared to the published analysis, this separation results in more accurate background model. Conversely, the published analysis used the combined fake factor method which measures the fake factors separately also, but combine them before using them. In that case the resulting fake background has only one component and some information on background correlations is lost.

4.4 Fake Factor Method

Particle mis-identification from signatures in the detector is an abundant source of background in many analyses. In searches with final state leptons[1] particle-level identification criteria are used for background suppression. However, identification algorithms are not perfect but have a finite background rejection power for a given signal efficiency. A certain fraction of reconstructed objects, which are not real leptons, satisfy identification requirements and therefore contribute to the background. Such mis-identified leptons are called fake leptons. Additionally, real electrons or muons can appear in heavy flavor decays, and electrons can manifest in photon conversion. These types of leptons are also considered fake because they are not produced promptly in a decay of a particle of interest.

In hadron colliders the most plentiful final state objects are jets; the QCD multi-jet process constitute the major fraction of total proton-proton collision cross section. Additionally, processes such as W+$jets$, Z/γ^*+$jets$ and top-quark are relevant sources of jets due to high trigger rate for events with a lepton from the vector boson decay. These background processes are usually dominating over the small signal of new physics. Jets can mimic the signatures of electrons, muons or hadronically decaying tau leptons.

The rate at which jets fake leptons is difficult to model correctly in Monte Carlo simulations. Most importantly Monte Carlo simulation is not an option due to the large jet production cross section and a relatively small number of jets passing lepton identification criteria. Moreover, a proper model would need to accurately predict fake rates from different sources: heavy flavor decays, photon conversion and hadrons. This level of modeling is not expected from the Monte Carlo simulation. Alternative options comprise a variety of data-driven methods. The Matrix Element, ABCD, Fake Rate and Fake Factor methods all use real data in addition to Monte Carlo simulation. The idea behind all data-driven methods is to extract information about the mis-identified object distributions from the data and use it to model background processes.

The BSM $H/A \to \tau\tau$ analysis makes use of the Fake Factor method. The Fake Factor method can be used in analyses which exploit particle-level identification criteria and is capable of providing event yields and kinematic distributions. A fake factor is the ratio of two fake rates of a mis-identified object with different identification criteria. Knowing the number of events with fake objects at one

[1] In this section leptons refer to all three generations of charged leptons.

identification criterion, extrapolation, using the fake factor, to the other identification criterion can be made. The method relies on the assumption that the ratio of two fake rates of the mis-identified object is independent of the rest of the event. This allows one to measure fake factors in a control region and apply it to a signal region. The assumption can only be approximate and such factors as event kinematics, sample composition and sample purity leads to additional complexity and systematic uncertainties. These contributing factors are discussed in the rest of this section.

A fake factor f is calculated from the ratio of the number of events satisfying the particle identification criterion of the signal region, N^{ID}, over the number of events with a modified identification criterion, $N^{Anti-ID}$, counted in a control region CR:

$$f = \left.\frac{N^{ID}}{N^{Anti-ID}}\right|_{CR}. \tag{4.4.1}$$

The final particle identification criterion is the same as that required in a signal region and the modified criterion must be orthogonal to that requirement. This fake factor, i.e. extrapolation factor, is then employed in signal region background estimation. The number of background events in a signal region SR in which the selected particle is a mis-identified object is the product of the fake factor and the number of events which pass the full signal region selection except the particle identification criterion is modified,

$$N^{ID}|_{SR} = f \times N^{Anti-ID}|_{SR}. \tag{4.4.2}$$

Fake factors must be measured in control regions which are enriched in events with mis-identified objects. Large statistics and high sample purity are necessary for a robust estimate of the fake factors. The assumption that fake factors do not depend on the surrounding activity of the mis-identified object works to a certain extent, and therefore it is highly desirable that kinematics of the control regions resemble that of the signal regions as closely as possible. This is in order that the rate at which jets fake leptons is similar in the signal and control regions.

Generally mis-identification rates depend strongly on some kinematic variables. Rejection power of an identification algorithm might depend on the location in the detector due to varying instrumentation. This would result in fake factors depending on pseudorapidity, η. Shower shapes in the calorimeters and particle

tracking capabilities, which are used for particle identification, depend on the momentum. This results in fake factors depending on transverse momentum, p_T. Fake factors can also have dependence on topological variables, for example, the azimuthal angle between the object and missing transverse energy. In these cases fake factors need to be parametrized in appropriate variables. It is important to select intervals of variable's values in which fake factors do not vary considerably. As a result the simple fake factor in Eq. 4.4.1 becomes multi-dimensional (here two-dimensional for simplicity):

$$f_{ij} = \left. \frac{N_{ij}^{ID}}{N_{ij}^{Anti-ID}} \right|_{CR} . \tag{4.4.3}$$

Here i, j label intervals of the values of different variables, i.e. histogram bins.

Additionally, selected control regions are composed of events which are not entirely composed of mis-identified objects. There is always some sample contamination from processes which produce real prompt leptons, and consequently constitute background to the fake factor measurement. Since control regions are designed to be dominated by events with mis-identified objects and, moreover, real leptons are sufficiently well modeled in simulation, this background is usually estimated with MC. If a background component in a control region can not be estimated with MC, then the Fake Factor method can be used therein provided a different fake factor has been measured elsewhere. The number of background events, N^{bkg}, must be subtracted from the number of data events, N^{data}, in each histogram bin ij. This results in an estimate of the number of signal events in the numerator and denominator. In this case Eq. 4.4.3 is modified to

$$f_{ij} = \left. \frac{(N^{data} - N^{bkg})_{ij}^{ID}}{(N^{data} - N^{bkg})_{ij}^{Anti-ID}} \right|_{CR} . \tag{4.4.4}$$

In addition to the kinematic dependence of fake factors, they are also different for the variety of jets that can be produced in hadron colliders. This is called the dependence on sample composition. From all the different types of jets it is customary to distinguish a few major categories. All jets are either gluon-initiated or quark-initiated, and the latter are either heavy-flavor or light-flavor jets. The gluon-initiated jets tend to be wider, having hadron tracks and energy deposits in calorimeter cells further away from the central axis. Also, the presence of heavy-flavor quarks in quark-initiated jets has a significant influence on mis-identification

rates.

Various Standard Model processes produce different types of jets. QCD multi-jet production is dominated by the leading order contribution depicted in Feynman diagram 4.2a. This process is the main source of gluon-initiated jets. Another major source of jets is the W+*jets* process with the leading order contribution depicted in Feynman diagram 4.2b. This process is used to enrich in quark-initiated jets, which are mostly initiated by light-flavor quarks. Finally, processes involving top quark, namely $t\bar{t}$ and single-top, are abundant sources of b-quark, i.e. heavy flavor quark, initiated jets.

Control regions are defined to be enriched with particular types of jets in order to account for the sample composition. Fake factors measured in different control regions are applicable only to those types of jets, or more precisely, those mixtures of jet types. This fact stiffens the definition of a control region with the requirement that the jet composition would be similar to that of the signal region.

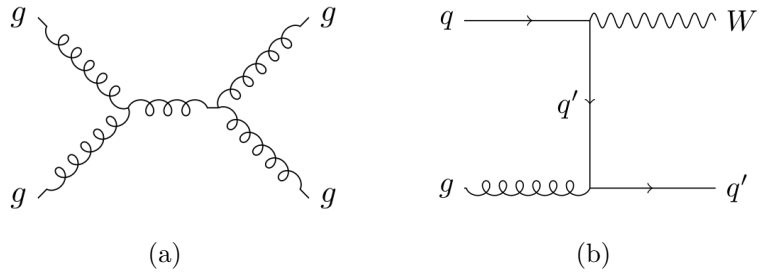

Figure 4.2: Leading order Feynman diagrams for (a) QCD multi-jet and (b) W+*jets* processes.

Various systematic uncertainties are associated with the Fake Factor method. The most important is a systematic uncertainty arising from fake factor dependence on kinematic variables. Ideally a multi-dimensional parametrization with many available variables should be used, but practically only a couple of the most important variables are considered. The remaining variation of the fake factors is accounted for with a systematic uncertainty. Another important source of uncertainty emerges from the dependence on sample composition. Even the same process in different kinematic regimes can produce different fractions of jet types and consequently lead to different fake factors. The difference between mixtures of jet types in control and signal regions leads to mismodeling which is usually small if the control region has been defined properly and can be accounted for with a

systematic uncertainty. This uncertainty can be estimated in MC by measuring the trend of fake factors in control and signal regions and this trend is taken as a systematic uncertainty. The last source of uncertainty arises from background contamination which is being subtracted. Precise modeling of the background leads to smaller systematic uncertainty.

The BSM $H/A \to \tau\tau$ analysis uses a validation region, which is very close in definition to the signal region, to validate the fake factors. The mismodeling in this validation region is taken as a combined systematic uncertainty which takes into account the kinematic and sample composition systematic uncertainties.

In the BSM $H/A \to \tau\tau$ analysis the final event selection involve all three flavors of charged leptons. Lepton mis-identification constitutes a background for each lepton flavor. QCD multi-jet, W+*jets* and top-quark backgrounds are large; QCD multi-jet process produce jets, one of which can fake an electron or a muon and another jet can fake a hadronically decaying tau lepton. In the W+*jets* process a prompt electron or muon is present from a W boson decay, but a jet can fake a hadronically decaying tau lepton. Processes involving top-quarks produce prompt electrons, muons or taus, but a heavy-flavor quark-initiated jets can fake hadronically decaying tau leptons. The Fake Factor method is applied to model background events arising from each lepton's mis-identification and the procedure is described below.

4.5 QCD Multi-jet Background

The QCD multi-jet process contributes to the background in the BSM $H/A \to \tau\tau$ analysis when jets are mistakenly identified as leptons. In the $\tau_{\text{lep}}\tau_{\text{had}}$ channel one jet fakes the selected electron or muon and another jet fakes the selected hadronically decaying tau lepton. This background source is estimated with the Fake Factor method and the fake factors are measured in the Fake Lepton Control Region.

4.5.1 Fake Lepton Control Region

The Fake Lepton Control Region (FLCR) is defined for lepton fake factor measurement. The lepton fake factors are then used to estimate QCD multi-jet background in the Signal Region, Validation Region (Section 4.7) and in the W+*jets* Control Region (Section 4.6.1).

The FLCR is defined in such a way that the event sample is enriched in

multi-jet events but at the same time the event topology is similar to that of the Signal Region. Event selection mainly differs from that of the Signal Region by a requirement on the BDT score of the tau identification algorithm. A cut on the BDT score is applied which corresponds to 1% signal (true tau) efficiency and means the control region is mainly composed of multi-jet events with W+$jets$ and $t\bar{t}$ processes constituting the background. There is no requirement on the electric charges of the electron/muon and tau candidates and there is no cut on $\Delta\phi^{\tau_{\mathrm{had}},\tau_{\mathrm{lep}}}$. This is because fake factors are insensitive to the differences in sample composition which would be obtained if these cuts were used, as was observed by studying these cut requirements. The cut value of the transverse mass is reduced to $m_{\mathrm{T}} < 30\,\mathrm{GeV}$ to further suppress W+$jets$ background. No requirement on lepton isolation is made because both isolated and anti-isolated leptons are needed to define numerator and denominator event numbers. An additional requirement of a single lepton is applied which increases the purity of multi-jet events, especially in the b-tag category where it suppresses top-quark background. The single lepton requirement vetoes events which, in addition to the selected lepton, contain other leptons with the failed "loose" identification requirement. The selected tau lepton in the MC background is not required to be truth-matched.

All background sources in this control region are modeled with MC, as shown in Fig. 4.3. Even the W+$jets$ contribution is estimated with MC, because the tau identification algorithm is well modeled for the fake taus which have low BDT score. This is because the variables that are used in the BDT are tuned to multi-jet and W+$jets$ data in this regime. Moreover, this process has a sufficiently large number of simulated events in this control region. The plots indicate that almost all the events where the lepton fails the isolation requirement arise from QCD multi-jet process. Events where the lepton passes the isolation requirement mostly come from QCD multi-jet process but there is a large background from W+$jets$ and $Z/\gamma^* \to ll$ processes which produce a real isolated lepton. Moreover, in the b-tag category a large background comes from top-quark processes which also produce a real isolated lepton.

The lepton fake factors are defined as the ratio of the number of events passing gradient lepton isolation requirement over the number of events failing this requirement, according to Eq. 4.4.4:

$$f^{jet\to lep}_{p_T,\Delta\phi} = \left.\frac{(N^{data} - N^{MC})^{pass\,ISO}_{p_T,\Delta\phi}}{(N^{data} - N^{MC})^{fail\,ISO}_{p_T,\Delta\phi}}\right|_{FLCR} . \tag{4.5.1}$$

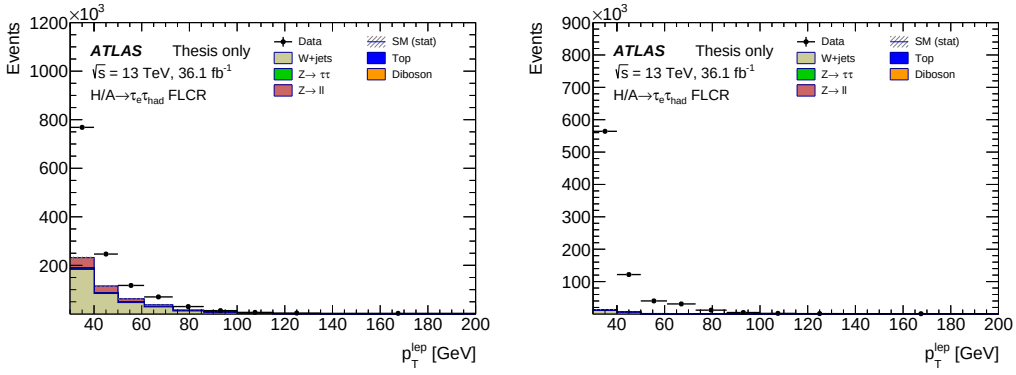

Figure 4.3: Electron p_{T} distributions in the b-veto category of the FLCR. Shown are numbers of events with leptons which (left) pass gradient isolation requirement and (right) fail the requirement. The difference between the data and MC is taken as the QCD multi-jet contribution.

The number of events from background processes are subtracted using an estimate derived from MC simulation. Lepton fake factors are measured separately for muon and electron channels because the rates at which jets fake leptons are very different for the two lepton flavors. The channels are further separated into b-tag and b-veto categories because some fake factor dependence is observed due to different light/heavy quark composition. Lepton fake factors are parametrized in lepton momentum, $p_{\mathrm{T}}^{\tau_{\mathrm{lep}}}$, and, in the electron channel, also in angular separation between the electron and the direction of the missing transverse energy, $\Delta\phi^{\tau_{\mathrm{e}},E_{\mathrm{T}}^{\mathrm{miss}}}$.

The measured fake factors are shown in Fig. 4.4 and Appendix A. In the electron channel the fake factors are seen to vary a lot at low electron p_{T} for different values of $\Delta\phi$. There is a rapid change in the electron fake factors at $p_{\mathrm{T}} = 60\,\mathrm{GeV}$ due to a different isolation criterion in the 60 GeV threshold electron trigger. At high values of lepton momentum the multi-jet signal sample is very small and therefore fake factors have large statistical uncertainties. Moreover, to cover possible mis-modeling a 20% variation on MC backgrounds is applied which leads to additional uncertainty. This systematic uncertainty is inflated at high values of lepton momentum because in this regime most events come from background processes.

It was observed that electron and muon fake factors depend quite strongly on lepton pseudorapidity, $\eta^{\tau_{\mathrm{lep}}}$, and could also be parametrized in this variable. However, this is not expected to improve the modeling of the discriminating variable m_T^{tot}, because it does not depend on $\eta^{\tau_{\mathrm{lep}}}$. This parametrization could matter if

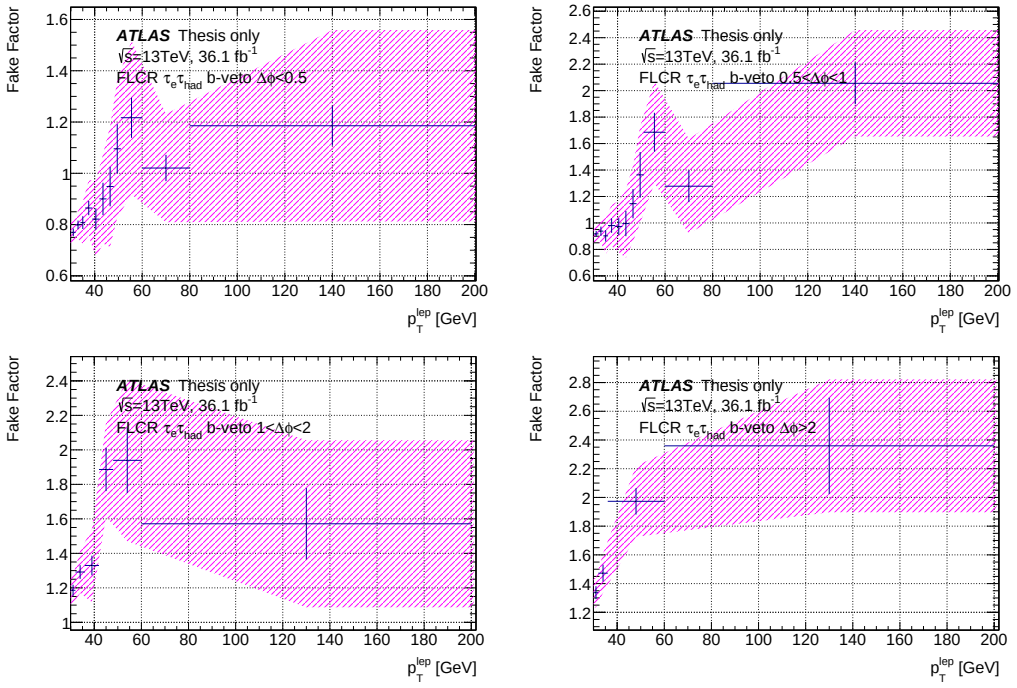

Figure 4.4: $Jet \rightarrow e$ fake factors in the b-veto category, parametrized in electron momentum and $\Delta\phi^{\tau_e,E_T^{miss}}$. The error bars indicate statistical uncertainty and the error bands indicate total uncertainty.

the multi-jet background had different shapes in this distribution in the SR and FLCR. However, distributions are not expected to be much different, because the two regions are very similar in event kinematics and an additional control region is defined to validate lepton fake factors. In that control region the modeling of the discriminating variable m_T^{tot} is sufficiently accurate within uncertainties.

4.6 Background With a Correctly Identified Lepton and a Jet Mis-identified as τ_{had}

A large background source is events in which the selected lepton is a real lepton but the selected τ_{had} is actually a jet. A hadronically decaying tau lepton candidate is composed of a small number of light charged and neutral mesons, mostly pions. However, this pattern of hadronically decaying tau lepton is also characteristic of jets. A large fraction of jets with a small number of hadron constituents are resembling hadronically decaying tau leptons. The tau lepton identification algorithm

has a finite jet rejection power and consequently some identified tau leptons are truly jets. Such objects are called fake taus throughout the thesis.

Most of the background events with a correctly identified lepton and a fake tau lepton come from W+$jets$ process in the b-veto category or top-quark and W+$jets$ processes in the b-tag category. In the b-veto category top-quark processes constitute a small background. Additionally, a small mixture of Z/γ^*+$jets$ and di-boson processes contribute to this background in both categories. However, these small backgrounds are not distinguished from the main W+$jets$ and top-quark processes.

This background source is estimated with the Fake Factor method. Fake factors are measured in the W+jets Control Region for the b-veto category and in the Same Sign Top Control Region for the b-tag category.

4.6.1 W+jets Control Region

The W+$jets$ control region (WCR) is defined for $jet \to \tau_{\text{had}}$ fake factor measurement. These fake factors are used to estimate the background contribution arising from processes in which a jet fakes the selected hadronically decaying tau lepton but the selected lepton is a real prompt lepton. Jets produced in W+$jets$ and top-quark processes are mostly quark-initiated jets. This is the main difference to the multi-jet case in which most jets are gluon-initiated.

The region selected to measure $jet \to \tau_{\text{had}}$ fake factors for the b-veto category is enhanced in W+$jets$ process events. A small mixture of other processes, namely Z/γ^*+$jets$ di-boson and top-quark, in which jets fake taus, are present in this sample. They are also present in the Signal Region b-veto category but there was no attempt made to separate them because the effect is negligible. Mis-identification rates depend on the substructure of jets and the mentioned processes also mostly produce quark-initiated jets.

Selected events in this control region differ from the events in the Signal Region by the m_{T} cut, $60 < m_{\text{T}} < 150\,\text{GeV}$. This particular transverse mass window is where the W+$jets$ process distribution has its peak. The higher cut on m_{T} is applied because above that mass the events mostly contain true taus from $t\bar{t}$ process. A requirement on the tau identification BDT score is applied, which corresponds to 99% signal (true tau) efficiency. This cut is used to remove those jets which are mostly gluon-initiated and therefore far from the Signal Region definition. Fake factors derived in this region are only used in the b-veto category

and therefore b-veto requirement is also applied.

The sample composition in the WCR is displayed in Figure 4.5 which shows τ_{had} transverse momentum distributions in the combined electron and muon channels. All backgrounds in which tau candidates are true taus or taus faked by leptons are estimated from MC. This type of events constitutes a very small background to the WCR. The QCD multi-jet contribution is estimated with the Fake Factor method. The $jet \rightarrow lepton$ fake factors, which are described in section 4.5.1, are applied to events which satisfy selection requirements of the WCR but the selected lepton fails the gradient isolation requirement. This control region, called WCR-anti-iso, also contain background events from processes which produce real prompt leptons, similarly to the events in the FLCR. Unfortunately there is no good estimate of the major W+$jets$ background in this WCR-anti-iso region, because the MC simulation is not precise for high BDT score tau fakes. Also the Fake Factor method can not be applied here because that would require the knowledge of the $jet \rightarrow \tau_{\text{had}}$ fake factors which are being measured in the WCR. It was decided to use MC in the WCR-anti-iso region for τ_{had} candidates which fail the tau identification criterion as shown in Figure 4.6 on the right-hand side. Monte Carlo simulation can be used because this intermediate BDT regime contains adequate statistics and this crude estimate is not significantly affecting the final fake factor measurement due to the smallness of the QCD multi-jet background in the WCR. For the τ_{had} candidates which pass the tau identification requirement background is assumed to be zero because, as shown in Figure 4.6 on the left-hand side, MC can not be used.

The combined electron and muon channels are used for the τ_{had} fake factor measurement. The prompt leptons from the W decay have no effect on the jet that fakes the tau. However, having a good estimate of the W+$jets$ signal contribution in both channels is needed in order to use the combined channel. It is noteworthy that the modeling of the QCD multi-jet background was important in bringing electron and muon channel tau fake factors close to each other. The electron channel has a much larger multi-jet background and therefore excluding it would bias the fake factor measurement. The absolute difference between the tau fake factors of the electron and muon channels was observed to be smaller than the statistical uncertainty of the fake factors.

The $jet \rightarrow \tau_{\text{had}}$ fake factors are defined as the ratio of number of events passing the "medium" tau identification working point requirement over the number

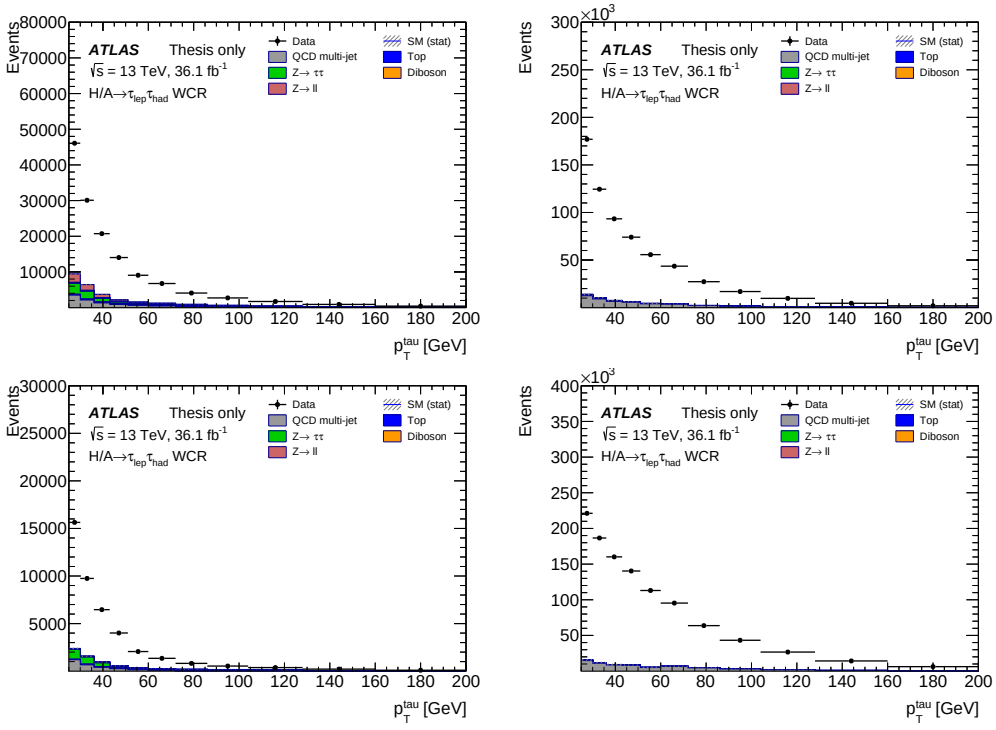

Figure 4.5: τ_{had} transverse momentum distributions in combined electron and muon channels in W+$jets$ Control Region. Shown are events with (top) 1-prong and (bottom) 3-prong τ_{had} candidates (left) passing and (right) failing the tau identification criterion. The difference between the data and background is taken as the W+$jets$ contribution.

of events failing this requirement. According to Eq. 4.4.4 the fake factor is

$$f^{jet\to\tau_{\text{had}}}_{p_T,\Delta\phi,prong} = \left.\frac{(N^{data}-N^{bkg})^{pass\,ID}_{p_T,\Delta\phi,prong}}{(N^{data}-N^{bkg})^{fail\,ID}_{p_T,\Delta\phi,prong}}\right|_{WCR}. \tag{4.6.1}$$

Events from QCD multi-jet and other processes are subtracted from data events. The fake factors are parametrized in tau transverse momentum p_{T}, angular separation in the transverse plane between tau and missing transverse energy $\Delta\phi^{\tau_{\text{had}},E_{\text{T}}^{\text{miss}}}$ and are separate for 1-prong and 3-prong tau candidates.

The measured fake factors are shown in Fig. 4.7 for 1-prong and in Fig. 4.8 for 3-prong tau candidates. The fake factors are varying considerably at low values of tau transverse momentum for different values of $\Delta\phi$ for both 1-prong and 3-prong tau candidates. At high values of tau p_{T} the 1-prong tau fake factors are varying significantly while 3-prong tau fake factors become stable with respect to $\Delta\phi$.

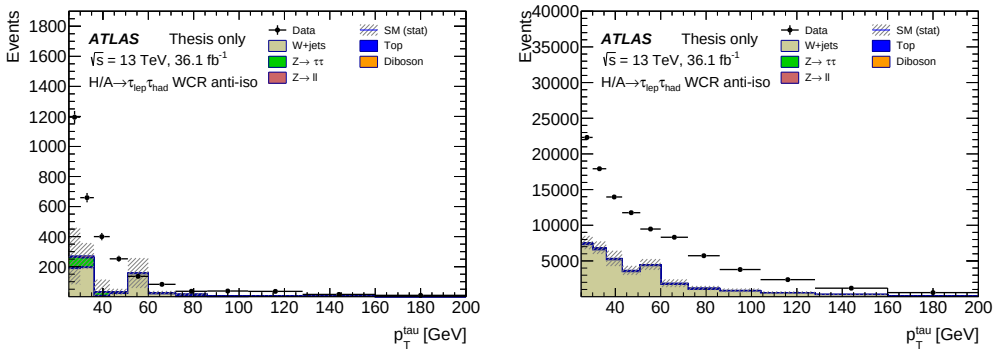

Figure 4.6: τ_{had} transverse momentum distributions in combined electron and muon channels in WCR-anti-iso weighted with lepton fake factors of section 4.5.1. Shown are events with 3-prong τ_{had} candidates (left) passing and (right) failing the tau identification criterion. The difference between the data and background in the right-hand side plot, and the data only in the left-hand side plot, is taken as the QCD multi-jet contribution in the WCR.

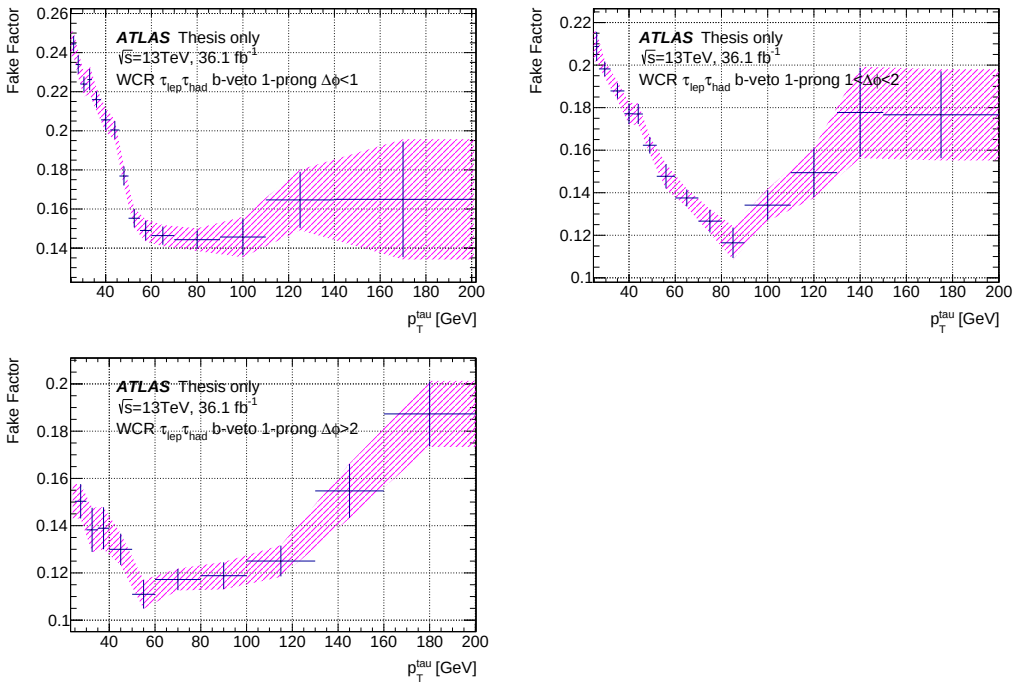

Figure 4.7: $Jet \rightarrow \tau_{\text{had}}$ fake factors for the b-veto category and 1-prong τ_{had} candidates, parametrized in τ_{had} momentum p_{T} and angular separation $\Delta\phi^{\tau_{\text{had}},E_{\text{T}}^{\text{miss}}}$. The error bars indicate statistical uncertainty and the error bands indicate total uncertainty.

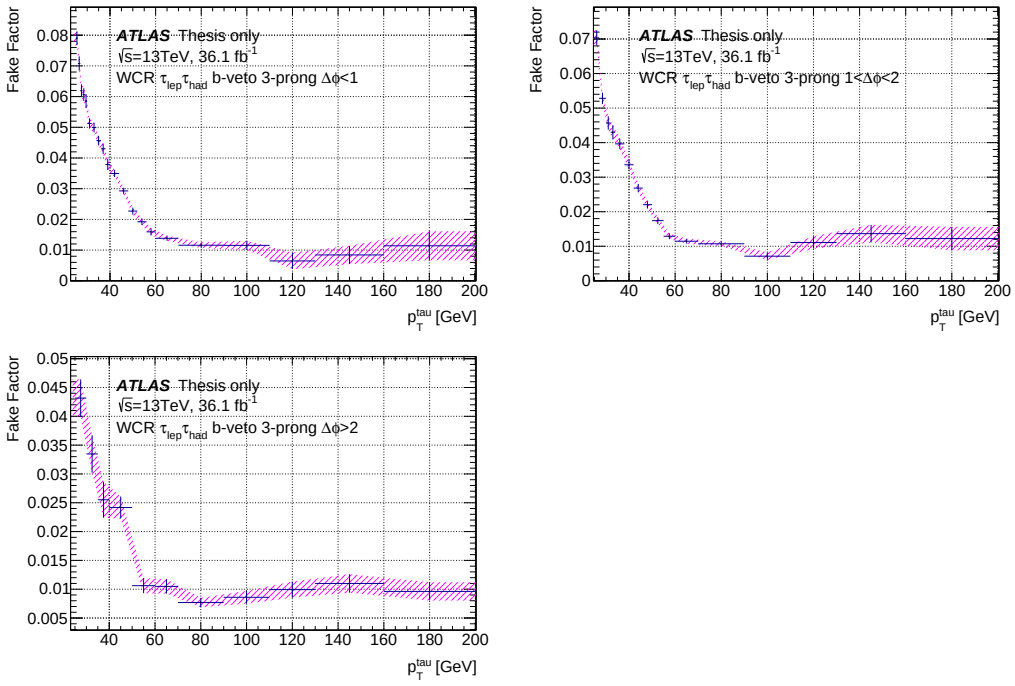

Figure 4.8: $Jet \rightarrow \tau_{\text{had}}$ fake factors for the b-veto category and 3-prong τ_{had} candidates, parametrized in τ_{had} momentum p_{T} and angular separation $\Delta\phi^{\tau_{\text{had}},E_{\text{T}}^{\text{miss}}}$. The error bars indicate statistical uncertainty and the error bands indicate total uncertainty.

To cover any possible mis-modeling a 10% variation on MC backgrounds is applied. This number is estimated conservatively according to the theoretical cross section precision and the precision of the in-situ measurements on electron, muon and τ_{had} in ATLAS. The uncertainty on the QCD multi-jet background arising from lepton fake factor uncertainties has negligible impact on the tau fake factor uncertainties and therefore is ignored.

4.6.2 Same Sign Top Control Region

The Same Sign Top Control Region (SSTCR) has a similar purpose to that of the WCR but fake factors measured here are used in the b-tag category. Events containing a b-tagged jet have a large top-quark background and provide a sample of heavy-flavor quark-initiated jets. In the b-tag category in all regions events with a jet faking a hadronically decaying tau lepton mostly arise from top-quark processes and the W+$jets$ process is the second largest contributor. As discussed in section 4.4 the rate at which jets fake tau leptons might depend significantly on the jet type. This contemplation is confirmed by measuring $jet \to \tau_{\text{had}}$ fake factors in a sample enriched with heavy-flavor jets.

Selected events in the SSTCR differ from the events in the W+$jets$ control region by the requirement that the tau and the lepton must have same electric charges. It was checked in MC simulation that there is no difference between the fake factors measured in this same sign region and the corresponding opposite sign region. The reason for using the same sign region is due to the fact that a large true tau background from top-quark processes is present in the opposite sign region. This background prevents collecting a pure heavy-flavor jet sample and consequently measuring the fake factors accurately. Additionally, the m_{T} cut in the SSTCR is only applied on the lower end, $m_{\text{T}} > 60\,\text{GeV}$. Fake factors derived here are only used in the b-tag category, and therefore b-tag requirement instead of b-veto requirement is applied in this region.

The sample composition in the SSTCR is displayed in Figure 4.9 which shows τ_{had} transverse momentum distributions in the combined electron and muon channels. All backgrounds are estimated in the same way as they are in the WCR with an exception of QCD multi-jet in events which fail the tau identification requirement. For this QCD multi-jet background no MC subtraction was performed because it is negligible.

The $jet \to \tau_{\text{had}}$ fake factors are defined as the ratio of number of events passing the "medium" tau identification working point requirement over the number of events failing this requirement. Similarly to Eq. 4.6.1 the fake factor is

$$f^{jet\to\tau_{\text{had}}}_{p_T,prong} = \left.\frac{(N^{data} - N^{bkg})^{pass\,ID}_{p_T,prong}}{(N^{data} - N^{bkg})^{fail\,ID}_{p_T,prong}}\right|_{SSTCR}. \tag{4.6.2}$$

Events from QCD multi-jet and other processes are subtracted from data events. The fake factors are parametrized in tau transverse momentum p_{T} and are separate

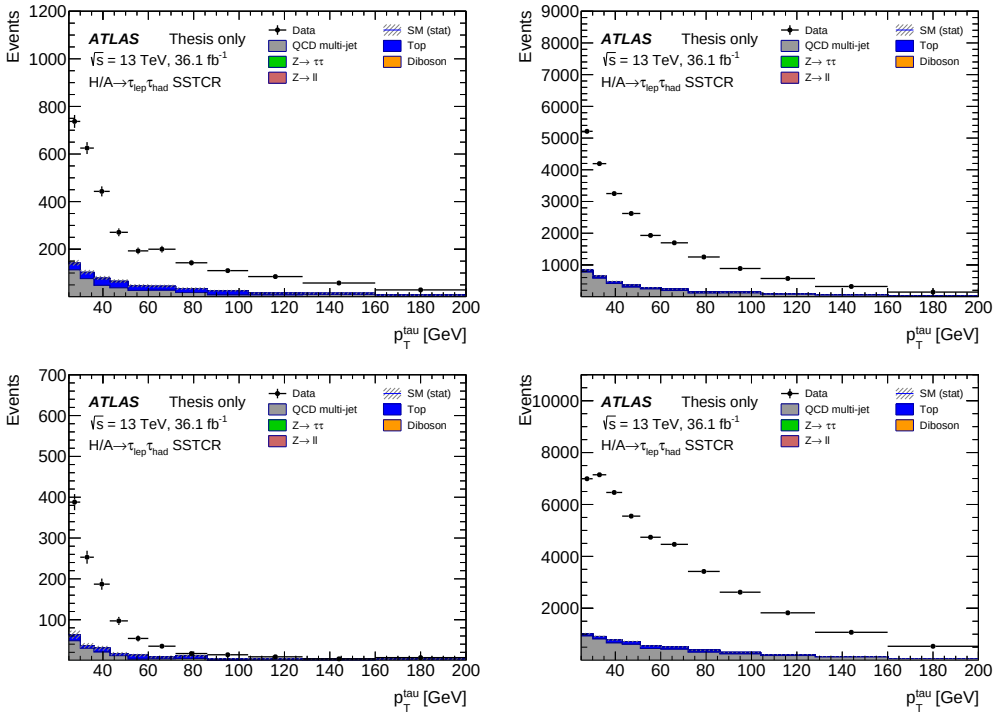

Figure 4.9: τ_{had} transverse momentum distributions in combined electron and muon channels in SS Top Control Region. Shown are events with (top) 1-prong and (bottom) 3-prong τ_{had} candidates (left) passing and (right) failing the tau identification criterion. The difference between the data and background is taken as the *W+jets* and top-quark contributions.

for 1-prong and 3-prong tau candidates.

The measured fake factors are shown in Figure 4.10 for 1-prong and 3-prong tau candidates. No variation with respect to $\Delta\phi^{\tau_{\text{had}},E_{\text{T}}^{\text{miss}}}$ was observed compared to the fake factors measured for the *b*-veto category. The fake factors in the SSTCR are considerably smaller than they are in the WCR confirming that heavy- and light-quark initiated jets have different fake rates.

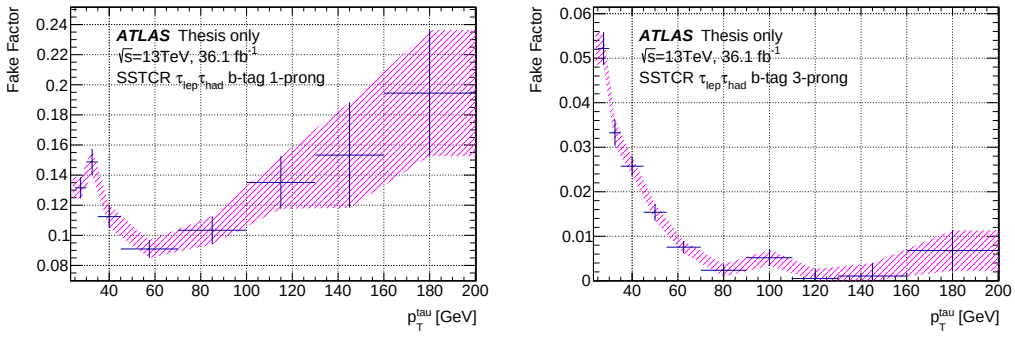

Figure 4.10: $Jet \rightarrow \tau_{\text{had}}$ fake factors for the b-tag category (left) 1-prong and (right) 3-prong τ_{had} candidates, parametrized in τ_{had} momentum p_{T}. The error bars indicate statistical uncertainty and the error bands indicate total uncertainty.

To cover any possible mis-modeling a 10% variation on MC backgrounds is applied as in the WCR. This MC uncertainty and the uncertainty on the QCD multi-jet background are negligible compared to the statistical uncertainties of the fake factors.

4.7 Validation Region

Validation Region (VR) is a region that is closest in definition to the Signal Region and therefore has a similar background composition. It serves two purposes: before the official ATLAS data un-blinding in 2017 it was used to check background modeling and currently it is being used to validate the fake factors. Events in the Validation Region differ from those in the Signal Region by the transverse mass cut; $40 < m_{\text{T}} < 60\,\text{GeV}$. In the b-veto category this region is dominated by fake taus from W+$jets$ events and in the b-tag category by true taus from top-quark processes and fake taus from W+$jets$ and top-quark. Due to the large fake tau background this region is exploited to check the validity of the $jet \rightarrow \tau_{\text{had}}$ fake factors. Discrepancies between data and background would indicate a serious mismeasurement of the fake factors or an underestimate of their uncertainties.

The modeling is checked in b-veto and b-tag categories separately for 1- and 3-prong tau candidates and separately in electron and muon channels. This splitting into additional categories is finer than in the Signal Region because fake factors are measured separately and are uncorrelated for 1- and 3-prong tau candidates. The fake factors are checked in τ_{had} transverse momentum distribution because they are

parametrized in this variable.

Distributions for the b-tag category are shown in Figure 4.11 and for the b-veto category in Figure 4.12. The QCD multi-jet background is estimated by reweighting events in which the selected lepton fails the gradient isolation requirement as in the WCR and SSTCR. The W/Top fakes background in the b-veto and b-tag categories are estimated with $jet \to \tau_{\text{had}}$ fake factors measured in the WCR and SSTCR, respectively. To estimate these backgrounds an additional control region is defined with the same VR selection except the selected tau lepton fails the identification requirement (with an additional cut on the BDT score as in the regions where the fake factors were measured). This region is called VR-anti-id and its events are reweighted with the τ_{had} fake factors to get the fake tau estimation in the VR. The VR-anti-id region contains large QCD multi-jet background as shown in Figure 4.13 for the electron channel b-veto category as an example. This background component is estimated from yet another control region which satisfy the selection requirements of the VR-anti-id except the selected lepton fails the gradient isolation requirement. This control region is called VR-anti-id-anti-iso and its events are reweighted with the lepton fake factors to get the multi-jet estimate in the VR-anti-id. Other background components in the VR-anti-id and VR-anti-id-anti-iso are estimated from the MC simulation (without tau truth-matching in the VR-anti-id-anti-iso). The whole procedure is schematically visualized in Figure 4.14. This method is also used in the Signal Region. The benefit of this procedure is that the selected tau lepton in the QCD multi-jet background, which is actually a fake tau, is taken from the data and therefore have the BDT score variable measured in data.

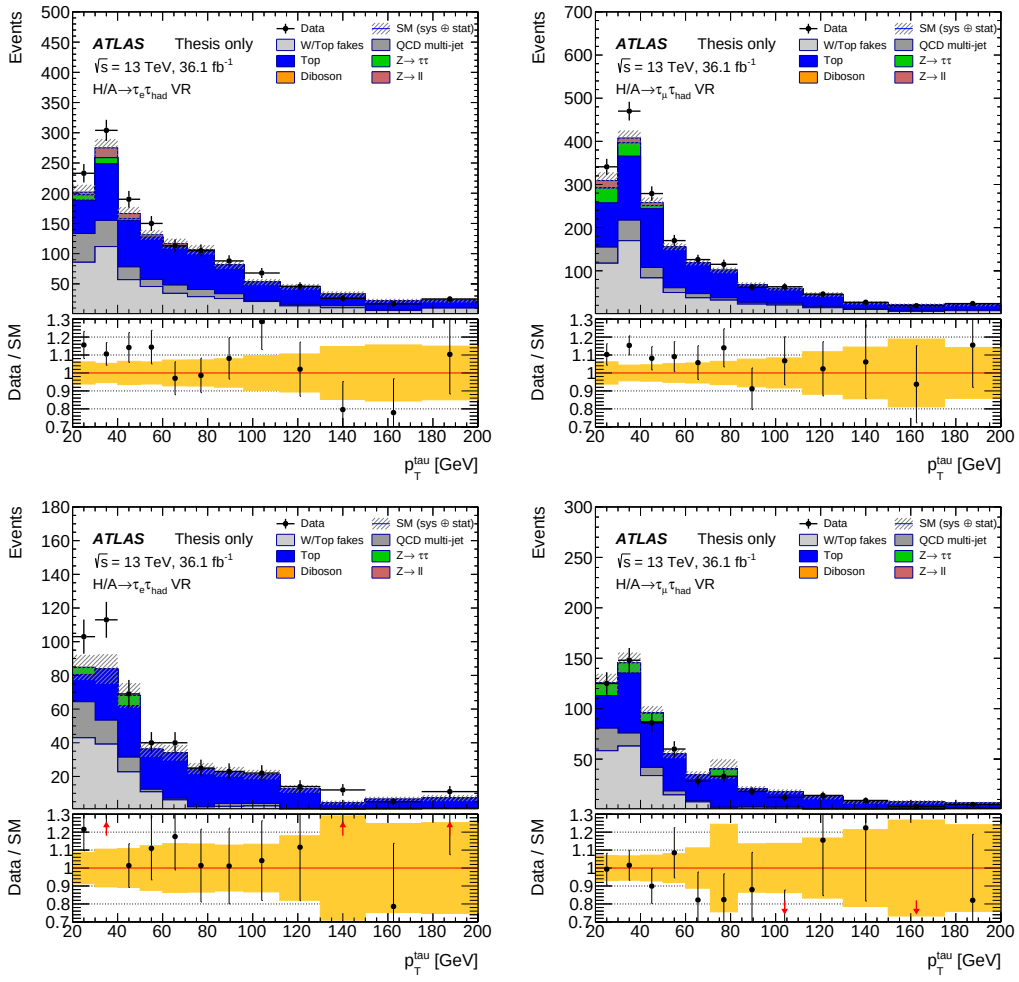

Figure 4.11: τ_{had} transverse momentum distributions in Validation Region b-tag category for (top) 1-prong and (bottom) 3-prong tau candidates in (left) electron and (right) muon channels. Systematic uncertainties from $jet \rightarrow lepton$ and $jet \rightarrow \tau_{\text{had}}$ fake factors are included in the error bands.

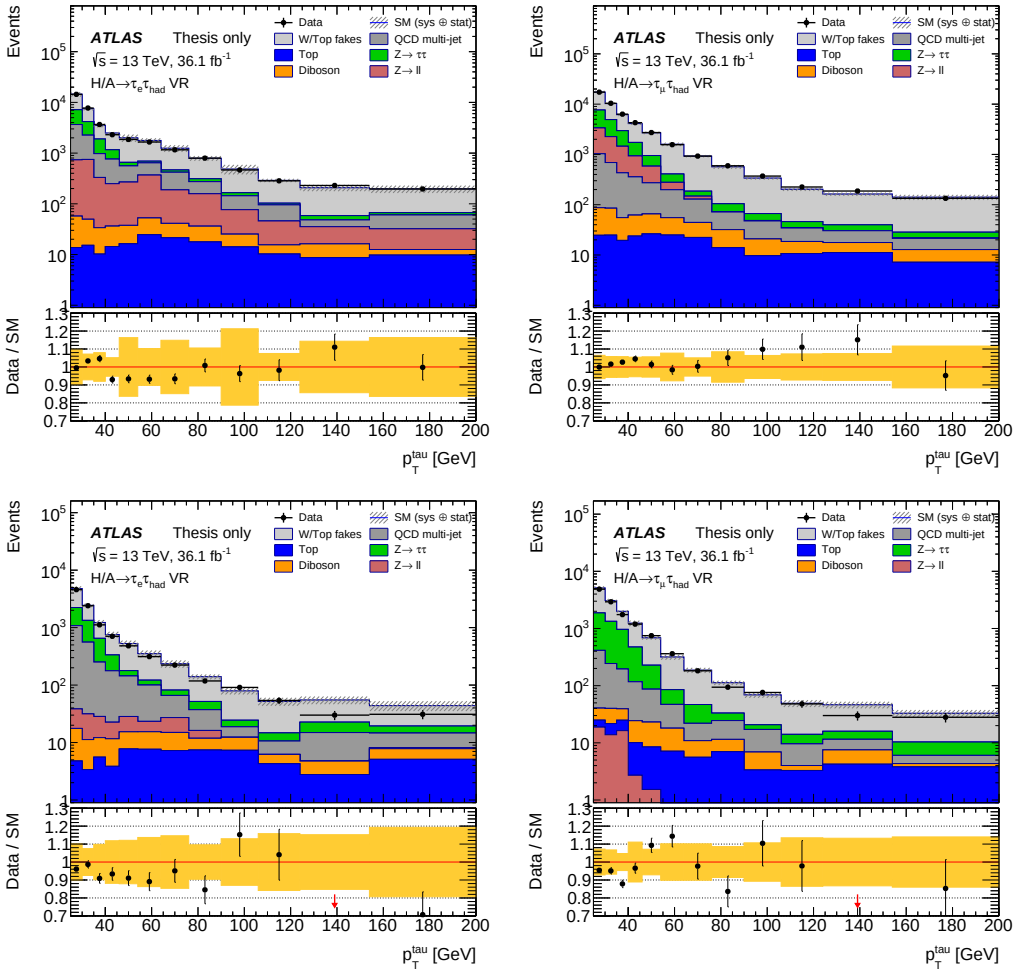

Figure 4.12: τ_{had} transverse momentum distributions in Validation Region b-veto category for (top) 1-prong and (bottom) 3-prong tau candidates in (left) electron and (right) muon channels. Systematic uncertainties from $jet \rightarrow lepton$ and $jet \rightarrow \tau_{\text{had}}$ fake factors are included in the error bands.

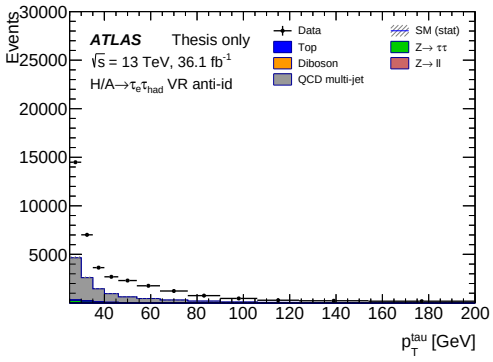

Figure 4.13: τ_{had} transverse momentum distribution in the VR-anti-id electron channel b-veto category reweighted with the tau fake factors. The QCD multi-jet background is estimated as written in the text. The difference between data and background is the W/Top fakes estimate in the VR.

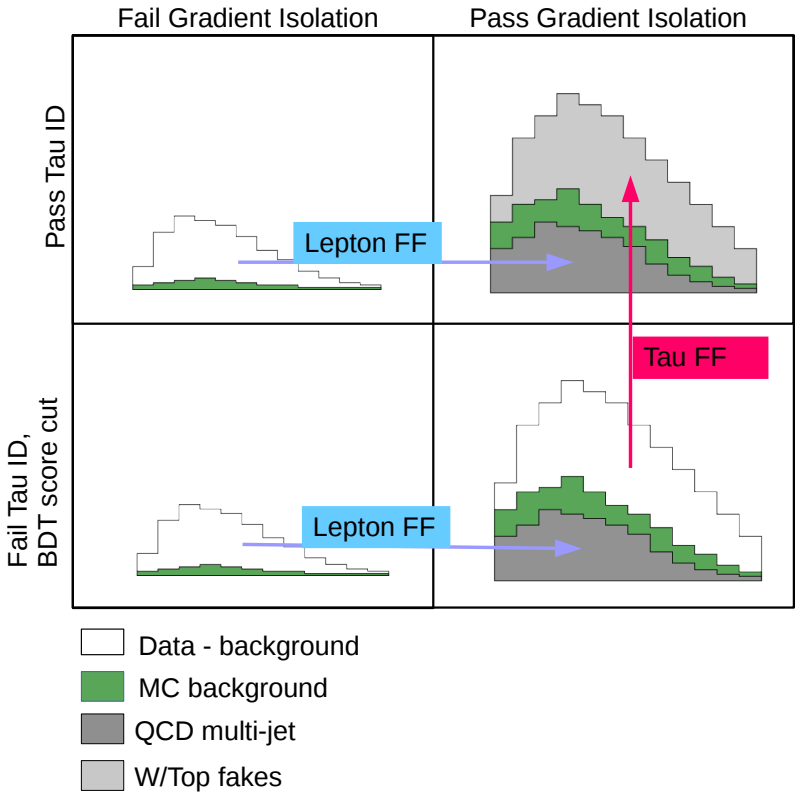

Figure 4.14: Schematic overview of the fake background estimation procedure.

Generally the agreement between data and the background model is good in the VR. Data mostly fluctuates within 1σ background error which includes statistical uncertainties as well as systematic uncertainties from the fake factors. Larger discrepancies are observed at low τ_{had} p_{T} in the b-tag category for 1-prong tau candidates and at high p_{T} in the b-veto category for 3-prong tau candidates. For this reason an additional 10% uncertainty on the τ_{had} fake factors are included for 1-prong b-tag fake factors below 60 GeV and for 3-prong b-veto fake factors above 120 GeV.

Distributions of total transverse mass in the VR are shown in Figure 4.15 for the b-tag category and in Figure 4.16 for the b-veto category. The background error contains lepton and full tau fake factor uncertainties together with a 10% error on MC subtraction in the VR-anti-id and a 20% error in the VR-anti-id-anti-iso. Modeling is good and brings confidence that the SR will be modeled well, too.

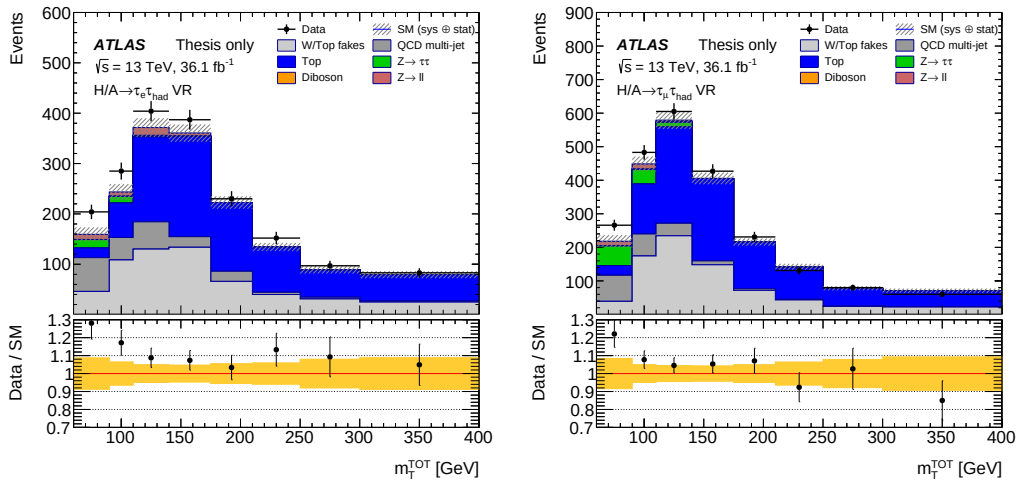

Figure 4.15: Total transverse mass distributions in the Validation Region b-tag category in (left) electron and (right) muon channels. Systematic uncertainties from $jet \rightarrow lepton$ and $jet \rightarrow \tau_{\text{had}}$ fake factors and from MC subtraction, as written in the text, are included in the error bands.

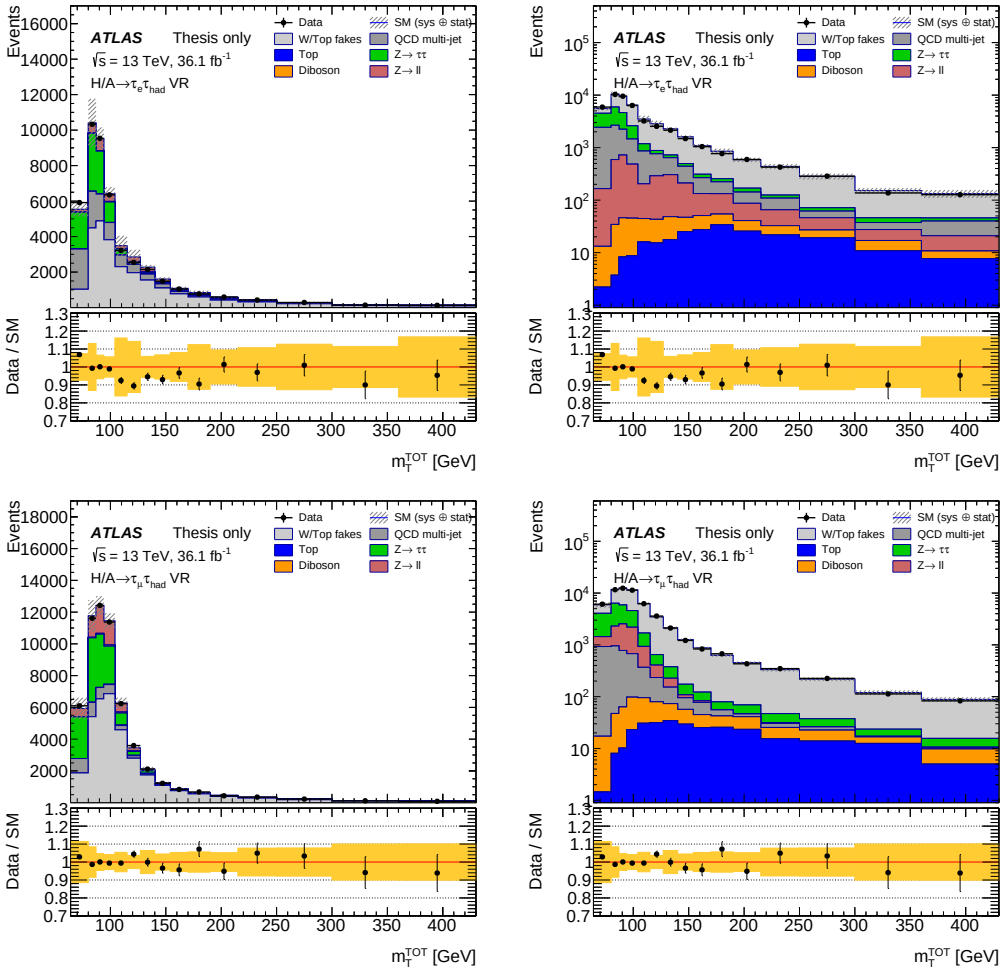

Figure 4.16: Total transverse mass distributions in the Validation Region b-veto category in (top) electron and (bottom) muon channels in (left) linear and (right) logarithmic scales. Systematic uncertainties from $jet \to lepton$ and $jet \to \tau_{\text{had}}$ fake factors and from MC subtraction, as written in the text, are included in the error bands.

4.8 Signal and Top Control Regions

The Signal and Top Control Regions are employed in the final fitting procedure. The Top Control Region (TCR) is included in order to reduce systematic uncertainties of the top-quark background. The event selection of the TCR differ from that of the Signal Region by the transverse mass cut, $m_{\text{T}} > 100\,\text{GeV}$, and, moreover, only the b-tag category is used. The background estimation in the TCR is performed

in the same way as in the Validation and Signal Regions. The composition of this background before the fitting procedure is shown in Fig. 4.17. The lower panel showing the data-background agreement in the $m_{\mathrm{T}}^{\mathrm{tot}}$ distribution clearly indicates the large systematic uncertainties affecting the top-quark background. This control region is relatively pure in the top-quark processes with some contamination from W/Top fake events and minor contribution from other events; the QCD multijet component is negligible in this region. The TCR also contains rather large amount of signal events which are also included in the fit for completeness, although the region is not sensitive to the signal. The large m_{T} cut of the TCR implies that background events are distributed at high total transverse mass and therefore contaminate the signal.

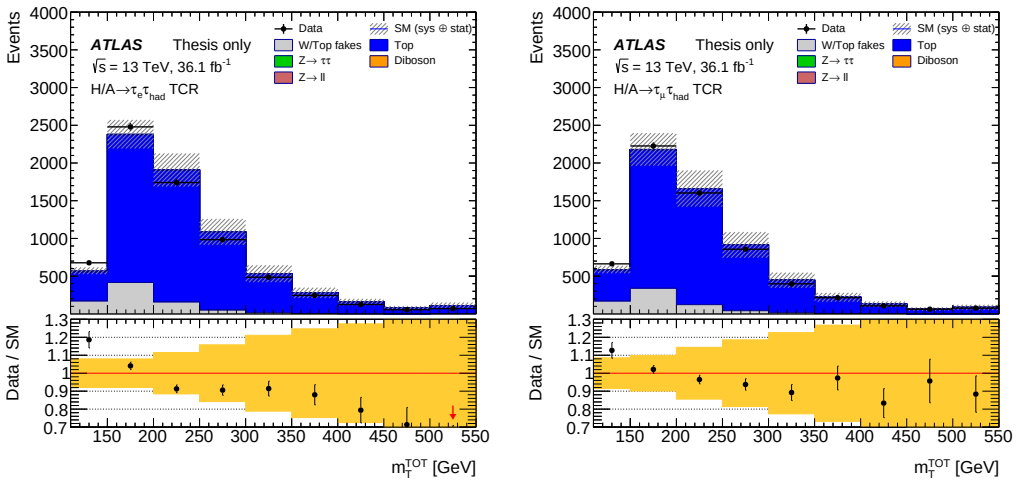

Figure 4.17: Pre-fit total transverse mass distributions in the Top Control Region (left) electron and (right) muon channels.

The background composition in the Signal Region is shown in Fig. 4.18. In the b-veto category largest background components at high masses come from $Z/\gamma^* \to \tau\tau$ and W/Top fake events. It is noteworthy that the QCD multi-jet and W/Top fake background distributions, which were estimated separately with the Fake Factor method, have rather different shapes among themselves and among the two channels. The QCD multi-jet background distribution falls much faster at high masses than the W/Top fake distribution. Moreover, in the muon channel the QCD multi-jet background is absent at high mass, which is the result of a very low probability for a jet to fake an energetic muon.

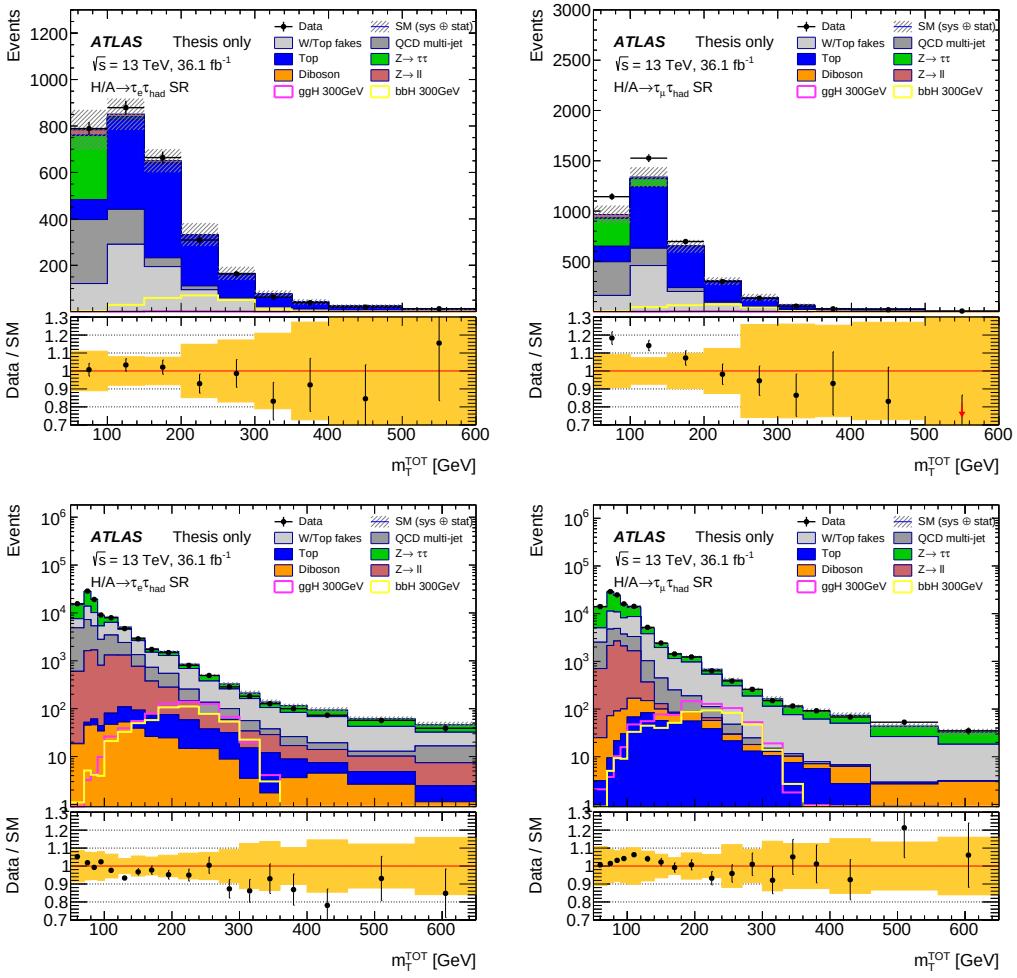

Figure 4.18: Pre-fit total transverse mass distributions in (top) b-tag and (bottom) b-veto categories of the (left) electron and (right) muon channels. The overlayed signal contribution is normalized to cross-section of 1 pb.

In the b-tag category the dominant background contribution at high masses arise from top-quark events and therefore the inclusion of the TCR in the fit helps to regain some signal sensitivity.

The amount of signal events in the Signal and Top Control Regions depends strongly on the signal category, signal production mode and mass of the resonance, as shown in Tables 4.4 and 4.5 for the gluon-gluon fusion and b-associated production modes, respectively. Electron and muon channels provide approximately similar event yields in corresponding categories.

Generally, lower mass points suffer from event loss due to rather strict re-

Table 4.4: The amount of gluon-gluon fusion (ggH) signal events in the Signal and Top Control Regions for different mass points of the resonance. The signal is normalized to cross-section of 1 pb and only statistical uncertainties are shown.

Category / Mass [GeV]	b-veto		b-tag		TCR	
	$\tau_e\tau_{had}$	$\tau_\mu\tau_{had}$	$\tau_e\tau_{had}$	$\tau_\mu\tau_{had}$	$\tau_e\tau_{had}$	$\tau_\mu\tau_{had}$
200	301 ± 11	466 ± 16	2.7 ± 1.0	3.6 ± 1.3	0	0
300	702 ± 18	741 ± 17	7.0 ± 2.1	10.2 ± 1.9	1.4 ± 0.6	1.6 ± 0.7
400	955 ± 22	953 ± 21	10.8 ± 2.0	10.0 ± 2.0	8.5 ± 4.3	3.1 ± 1.0
500	1093 ± 22	1075 ± 22	22 ± 3	15 ± 3	8.2 ± 1.8	5.9 ± 1.5
600	1128 ± 27	1123 ± 25	11 ± 2	17 ± 3	8.0 ± 2.0	8.6 ± 2.1
700	1186 ± 27	1184 ± 25	22 ± 4	22 ± 3	10.3 ± 2.3	8.8 ± 2.0
800	1159 ± 27	1194 ± 27	18 ± 3	24 ± 4	8.3 ± 2.0	10.6 ± 2.4
1000	1036 ± 25	1078 ± 24	29 ± 4	28 ± 4	16 ± 4	14.0 ± 2.4
1200	950 ± 24	1038 ± 24	22 ± 3	24 ± 4	15 ± 3	19 ± 5
1500	751 ± 18	912 ± 21	20 ± 3	42 ± 6	13.0 ± 2.3	16 ± 2
1750	659 ± 17	817 ± 19	17 ± 3	26 ± 3	13.6 ± 2.3	24 ± 3
2000	546 ± 16	722 ± 17	12.1 ± 2.3	25 ± 4	16 ± 3	20 ± 3
2250	471 ± 15	633 ± 16	12.7 ± 2.2	23 ± 3	14.2 ± 2.3	19 ± 3

quirements on the transverse momentum of the tau and the leptons. The signal event yield is maximum for mass points around $600 - 800$ GeV and decrease for increasingly higher masses. This signal loss at high masses is mostly due to the tau reconstruction inefficiency (shown previously in Fig. 3.4) when the charged-hadron tracks merge or miss the innermost layer hit in the tracker.

The gluon-gluon fusion production mode has a very small event yield in the b-tagged categories due to the b-tag requirement. On the other hand, the b-associated production mode has a large contribution to the b-tagged categories and also to the b-veto category. The amount of signal events in this mode is still largest in the b-veto category due to limitations of jet acceptance when the b-jets are produced in the forward directions.

Table 4.5: The amount of b-associated production (bbH) signal events in the Signal and Top Control Regions for different mass points of the resonance. The signal is normalized to cross-section of 1 pb and only statistical uncertainties are shown.

Category / Mass [GeV]	b-veto		b-tag		TCR	
	$\tau_e\tau_{had}$	$\tau_\mu\tau_{had}$	$\tau_e\tau_{had}$	$\tau_\mu\tau_{had}$	$\tau_e\tau_{had}$	$\tau_\mu\tau_{had}$
200	258 ± 13	328 ± 13	78 ± 7	111 ± 8	11.0 ± 2.6	8.7 ± 2.2
300	551 ± 18	523 ± 16	224 ± 11	231 ± 10	53 ± 6	48 ± 5
400	647 ± 18	606 ± 16	311 ± 12	304 ± 11	109 ± 7	85 ± 6
500	701 ± 21	632 ± 19	357 ± 15	360 ± 13	141 ± 9	134 ± 8
600	698 ± 14	664 ± 13	391 ± 10	392 ± 10	186 ± 7	159 ± 6
700	687 ± 24	739 ± 22	422 ± 18	409 ± 17	219 ± 12	179 ± 11
800	689 ± 23	652 ± 22	427 ± 19	412 ± 17	218 ± 13	194 ± 12
1000	561 ± 19	617 ± 18	375 ± 15	416 ± 15	218 ± 11	226 ± 11
1200	533 ± 20	590 ± 20	340 ± 16	353 ± 16	222 ± 13	245 ± 13
1500	421 ± 17	492 ± 18	269 ± 15	349 ± 15	218 ± 13	234 ± 13
1750	306 ± 36	454 ± 39	231 ± 34	270 ± 34	202 ± 29	250 ± 28
2000	272 ± 36	375 ± 40	174 ± 30	225 ± 33	225 ± 27	212 ± 29
2250	280 ± 33	280 ± 34	137 ± 28	234 ± 31	160 ± 26	209 ± 28

4.9 Statistical Analysis

4.9.1 Fitting procedure

The background model was fit to the data using the maximum likelihood method. The method comprises constructing a likelihood function and finding the maximum value of that function. The likelihood function is a product of Poisson probability distribution terms where each term comes from histogram bins of the discriminating variable; in this particular case it is the total transverse mass. The Poisson terms are formed from the expected number of events that are predicted by the model and from the observed number of events. The expected number of events in each histogram bin i of the discriminating variable is the sum of signal s_i and background b_i events predicted by the model:

$$E[n_i] = \mu s_i + b_i. \tag{4.9.1}$$

Parameter μ is called the signal strength parameter where $\mu = 0$ corresponds to background-only hypothesis and $\mu = 1$ corresponds to nominal signal+background hypothesis. With these definitions the Poisson probability term for one histogram bin can be written as

$$\mathcal{P}_i^{\text{Poisson}}(n_i; \mu s_i + b_i) = \frac{(\mu s_i + b_i)^{n_i}}{n_i!} e^{-(\mu s_i + b_i)}, \tag{4.9.2}$$

where n_i is the observed number of events in bin i. In general, predicted numbers of events are influenced by systematic uncertainties coming from various sources in the experiment. The predicted signal and background events are functions of parameters that are employed to parametrize the systematic uncertainties. These parameters, denoted by a vector $\boldsymbol{\theta}$, are called nuisance parameters as opposed to the previously introduced parameter μ, which is called the parameter of interest. The values of nuisance parameters are not of interest in the searches for new physics as they parametrize the errors of the experimental setup. On the other hand, the value of the parameter μ is of great importance as it parametrizes the amount of signal that can be present in the data. Finally, the likelihood function can be written as

$$\mathcal{L}(\mu, \boldsymbol{\theta}; \boldsymbol{n}) = \prod_{i=1}^{N} \mathcal{P}_i^{\text{Poisson}}(n_i; \mu s_i(\boldsymbol{\theta}) + b_i(\boldsymbol{\theta})). \tag{4.9.3}$$

The finding of the maximum value of this function follows. The best-fit values, maximum likelihood estimators, are denoted with a hat:

$$\mathcal{L}(\hat{\mu}, \hat{\boldsymbol{\theta}}; \boldsymbol{n}) = \max|_{(\mu,\theta)} \mathcal{L}(\mu, \boldsymbol{\theta}; \boldsymbol{n}). \tag{4.9.4}$$

Conditional fit with a fixed value of μ is commonly used and the resulting best-fit values of the nuisance parameters, conditional maximum likelihood estimators, are denote with a double-hat:

$$\mathcal{L}(\mu, \hat{\hat{\boldsymbol{\theta}}}; \boldsymbol{n}) = \max|_{\theta} \mathcal{L}(\mu, \boldsymbol{\theta}; \boldsymbol{n}). \tag{4.9.5}$$

A profile likelihood ratio, λ, which will be used in the definition of a test statistic, is defined as

$$\lambda(\mu) = \frac{\mathcal{L}(\mu, \hat{\hat{\boldsymbol{\theta}}}; \boldsymbol{n})}{\mathcal{L}(\hat{\mu}, \hat{\boldsymbol{\theta}}; \boldsymbol{n})} \tag{4.9.6}$$

Since the conditional fit is used in the numerator, the profile likelihood ratio is a function of μ. In the search for a new process which is expected to increase the total number of observed events, it is assumed that the signal contribution can only be non-negative, that is $\mu \geq 0$. If the best-fit value of μ is found to be below 0, $\hat{\mu} < 0$, then the best level of agreement between data and any physical value of μ happens at $\mu = 0$. The profile likelihood ratio is then defined with additional constrains as

$$\tilde{\lambda}(\mu) = \begin{cases} \frac{\mathcal{L}(\mu, \hat{\hat{\boldsymbol{\theta}}}(\mu); \boldsymbol{n})}{\mathcal{L}(\hat{\mu}, \hat{\boldsymbol{\theta}}; \boldsymbol{n})} & \hat{\mu} \geq 0, \\ \frac{\mathcal{L}(\mu, \hat{\hat{\boldsymbol{\theta}}}(\mu); \boldsymbol{n})}{\mathcal{L}(0, \hat{\hat{\boldsymbol{\theta}}}(0); \boldsymbol{n})} & \hat{\mu} < 0. \end{cases} \tag{4.9.7}$$

4.9.2 Statistical Interpretation

The goal of statistical analysis is to test models against data. The models under investigation arise from various hypotheses, which can generally be of two types: the null and the alternative hypotheses. The null hypothesis is the one which is currently widely accepted and therefore needs to be challenged by experiments in order to discover any new phenomena. The alternative hypothesis is prepared to take over the null hypothesis if the latter fails to stand the test of experiments. In particle physics experiment searches for new physics the null hypothesis is the

Standard Model[2] and, in this particular case, the alternative hypothesis is the MSSM.

To practically test a model against data a measure of how good the model describes the data needs to be defined. In the frequentist approach to statistical interpretation this measure is the p-value. The p-value is a cumulative probability to observe the value of a test statistic with equal or worse agreement to that of the measured value. In order to calculate the p-value, a test statistic needs to be defined and its probability distribution needs to be obtained. According to [159], for a search of a new signal the test statistic is

$$q_0 = \begin{cases} -2\ln\lambda(0) & \hat{\mu} \geq 0, \\ 0 & \hat{\mu} < 0, \end{cases} \tag{4.9.8}$$

where $\lambda(0)$ is the profile likelihood ratio defined in Eq. 4.9.6. The fitted value of $\hat{\mu}$ much higher than 0 means larger disagreement between the data and background-only ($\mu = 0$) hypothesis and gives larger value of q_0. Larger values of q_0 are less probable and consequently the background-only hypothesis might be rejected if the observed p-value is equal to or smaller than the one agreed upon in advance.

The probability distribution of the test statistic can be obtained by randomly sampling the model and calculating the value of the test statistic for every sample. This approach can be computationally expensive and therefore an alternative approximate method, called the asymptotic approximation, can be used to calculate probability distribution functions. According to [159] the asymptotic formulae for the probability distribution functions (pdf) of test statistics allows the calculation of significance for a given dataset as well as the median expected significance and it's variation due to statistical fluctuations in the data. If the pdf of a test statistic q_0 for a background-only hypothesis is denoted by $f(q_0|0)$ the p-value is calculated as

$$p_0 = \int_{q_0,\text{obs}}^{\infty} f(q_0|0)dq_0 \tag{4.9.9}$$

The result of the p-value can be translated into the Gaussian significance, Z, using

[2]The Standard Model without the SM Higgs is still being used.

the inverse of the cumulative Gaussian function:

$$Z = \Phi^{-1}(1-p), \tag{4.9.10}$$

The significance Z is equal to the number of standard deviations found above the mean of the Gaussian distributed variable that leaves the upper-tail probability equal to p. Smaller p-values correspond to larger significances; 1σ deviation corresponds to a p-value of 0.34, 2σ - to 0.025, etc. It is agreed in the high energy physics community to claim discovery if 5σ significance is reached. This significance corresponds to the probability $p = 2.87 \times 10^{-7}$ to observe data in disagreement with the model at the level of the data obtained or worse. It is also agreed that the status of evidence can be claimed if 3σ significance is reached.

4.9.3 Exclusion Limits

Most of the time experiments do not find evidence of a new signal but in these cases exclusion limits on the signal strength parameter can be obtained. In such a case the goal is to reject various signal hypotheses using the measure of the p-value. For the purpose of deriving exclusion limits on the parameter of interest μ a test statistic, namely

$$\tilde{q}_\mu = \begin{cases} -2\ln\tilde{\lambda}(\mu) & \hat{\mu} \leq \mu, \\ 0 & \hat{\mu} > \mu, \end{cases} \tag{4.9.11}$$

was used, where $\tilde{\lambda}(\mu)$ is defined in Eq. 4.9.7. The test statistic is set to 0 when the hypothesized signal strength is below the best-fit value because one would not regard data with $\hat{\mu} > \mu$ as being less compatible with μ than the data obtained. On the other hand, much higher values of μ than the best-fit value $\hat{\mu}$ would give large values of $\tilde{q}_\mu$, which is improbable, and therefore such μ would be excluded based on the p-value.

The pdf for the test statistic under hypothesis μ is denoted by $f(\tilde{q}_\mu|\mu)$ and the p-value is equal to

$$p_\mu = \int_{\tilde{q}_{\mu,\mathrm{obs}}}^{\infty} f(\tilde{q}_\mu|\mu)d\tilde{q}_\mu. \tag{4.9.12}$$

For exclusion limits it is agreed to demand a p-value of 0.05, the 95% confidence

limit (CL), which corresponds to the significance of $Z = 1.64$.

Prior to looking at the data it is of interest to quantify the experimental sensitivity by quoting the expected median significance. The expected sensitivity can be given in terms of the p-value corresponding to the median q_μ obtained from a distribution with a different strength parameter μ'. For the exclusion limits it is of interest to know with what significance one would be able to reject different values of μ. Since the test statistic $\tilde{q}_\mu$ is used, the expected median significance is given by the median value $\text{med}(\tilde{q}_\mu)$ of the $f(\tilde{q}_\mu|0)$ pdf, which assumes that data is distributed according to the background-only hypothesis. Then, the expected p-value for the μ hypothesis is

$$p_{\mu,\text{exp}} = \int_{\text{med}(\tilde{q}_\mu)}^{\infty} f(\tilde{q}_\mu|\mu) d\tilde{q}_\mu. \tag{4.9.13}$$

For high values of μ the median significance would give p-values below the specified threshold and therefore be rejected.

Before looking at the real data, the required pdfs are obtained from a fictitious data set called Asimov data set. It is defined as the one that gives the maximum likelihood estimators of nuisance parameters and the parameter of interest their hypothesized values.

4.10 Systematic Uncertainties

Systematic uncertainties by their effect can be normalization and/or shape uncertainties. Normalization uncertainties affect the total number of events in a signal or control region, while shape uncertainties affect the bin-by-bin distribution of the discriminating variable without altering the total number of events. A particular systematic uncertainty can be both normalization and shape uncertainty. Origin of a systematic uncertainty can be categorized into theoretical and experimental. Theoretical uncertainties include cross section predictions, which is used in the normalization of simulated background samples, and signal shape uncertainties, which in reality depend on the model. The normalization of signal samples is the free variable in the fit: the parameter of interest. Experimental uncertainties comprise uncertainties on the integrated luminosity, detector simulation, event generation and data-driven background estimation. In this section the nature of systematic uncertainties is described and their effect for this analysis is estimated.

The treatment of systematic uncertainties is included in the analysis by

producing, for every systematic variation, a histogram template, which happens to be different from the nominal histogram template. Those histogram templates are considered to be the 1σ variations of systematic uncertainties. The intermediate values between the nominal values and the 1σ variations are interpolated linearly and parametrized with the nuisance parameters, $\boldsymbol{\theta}$, defined in Section 4.9.1. The nuisance parameters are constrained in the fit with Normal Gaussian probability density functions. These probability terms do not allow the nuisance parameters to get the best-fit values far from their central values. The best-fit values of nuisance parameters which have largest pulls are shown in Appendix B.

In order to decrease computation time of the statistical analysis, a pruning procedure is applied to systematic uncertainties. Pruning is applied to systematic uncertainties which generally have small impact on the histogram templates. A normalization uncertainty is neglected if for all samples the variation is less than 0.5% compared to the nominal background model. Similarly, a shape uncertainty is neglected if for all samples not one single bin has a variation over 0.5% after the overall normalization is removed.

4.10.1 Experimental Uncertainties

Luminosity

The total uncertainty on the integrated luminosity for the $36.1\,\text{fb}^{-1}$ proton-proton collision data set, taking into account uncertainties in the luminometer measurements and van der Meer scans, is 3.2%. This normalization uncertainty affects all simulated samples.

Pile-up

The effect of the average number of interactions per bunch crossing (pile-up) on the simulated samples is estimated by varying the pile-up by 9%. This variation results in normalization and shape uncertainties of the simulated samples.

Electrons

Uncertainties related to electron measurements include reconstruction, triggering, identification, isolation efficiencies as well as energy scale and resolution.

The precision of the scale factors that were used to correct electron efficiencies in simulated samples reach a few percent at low E_{T} and is below 1% at

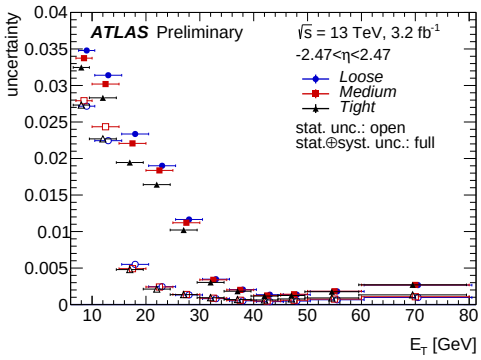

Figure 4.19: Electron reconstruction and identification uncertainties as a function of the electron E_{T} [84]. Uncertainties for electrons with $p_{\mathrm{T}} > 30\,\mathrm{GeV}$ and "medium" identification are below 0.5%.

high E_{T}. The combined reconstruction and identification uncertainties are shown in Fig. 4.19. The electron energy scale has been obtained with uncertainty less than one per mille.

These uncertainties were found to have a negligible impact on the analysis results.

Muons

Uncertainties related to muon measurements include, similarly to the electron measurements, reconstruction, triggering, identification, isolation efficiencies as well as energy scale and resolution.

Uncertainty on muon identification scale factor is around $0.06 - 0.5\%$ for muons with $30 < p_T < 200\,\mathrm{GeV}$ and an additional uncertainty of $2 - 3\%$ per TeV is applied for muons with $p_T > 200\,\mathrm{GeV}$. Muon isolation scale factor uncertainties range from per mil level in a wide p_T range and reaches the percent level for high p_T muons. Muon energy scale has an uncertainty of 0.05% in the barrel region, increasing with $|\eta|$ to 0.1% in the region $|\eta| \approx 2.5$. Muon momentum resolution is between $2 - 3\%$.

All uncertainties related to muon measurements are found to have minor impact on the analysis results.

$\boldsymbol{E}_{\mathbf{T}}^{\mathbf{miss}}$

Systematic uncertainties associated with the measurement of $E_{\mathrm{T}}^{\mathrm{miss}}$ are provided for the scale and for the resolution. They depend on the composition of hard terms as well as on the magnitude of the soft term. Uncertainties on scale and resolution of the hard objects are propagated to the $E_{\mathrm{T}}^{\mathrm{miss}}$ where correlations between systematic uncertainties for the same type objects are taken into account. The systematic uncertainty of the $E_{\mathrm{T}}^{\mathrm{miss}}$ resolution is extracted from parallel and perpendicular projections of the $E_{\mathrm{T}}^{\mathrm{miss}}$ vector onto the vector sum of the p_{T} of hard objects. The widths of the distributions of the projections yield the respective systematic uncertainties. The parallel projection yields the uncertainty of the $E_{\mathrm{T}}^{\mathrm{miss}}$ scale.

b-tagging

Systematic uncertainties affecting the b-tagging efficiency arise from MC generator modeling, normalization and experimental. The MC generator modeling affects the kinematics and jet flavor composition of simulated events. The normalization uncertainties account for the theoretical cross section errors used to normalize simulated events. The experimental uncertainties account for the detector effects and reconstruction efficiencies of physics objects. These uncertainties are implemented in the analysis as variations of SFs. The SFs themselves range from 0.96 to 1.04 depending on the jet p_{T} and the uncertainties range from 2 to 12%. It is noteworthy that SFs show no dependence on μ or jet η.

Jets

The JVT performance measurements show agreement between data and simulation at the 4% level for jets with $p_{\mathrm{T}} = 20\,\mathrm{GeV}$ and at the 1% level for jets with $p_{\mathrm{T}} = 60\,\mathrm{GeV}$. The uncertainty of the JVT selection efficiency is less than 0.6%.

The final JES uncertainty is derived from individual uncertainties of calibration techniques and in-situ measurements and is found to be 4.5% at 20 GeV, 1% at 200 GeV and 2% at 2 TeV. JES uncertainty as a function of the jet p_{T} and jet η is shown in Fig. 4.20.

Taus

Systematic uncertainty of the reconstruction of hadronically decaying tau leptons is between 2% and 4.5%, as shown in Fig. 4.21.

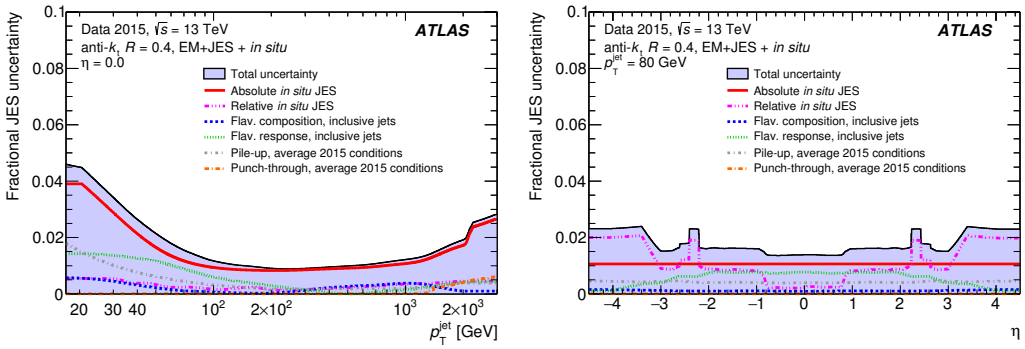

Figure 4.20: The jet energy scale uncertainty as a function of the (left) jet p_{T} and (right) jet η [92].

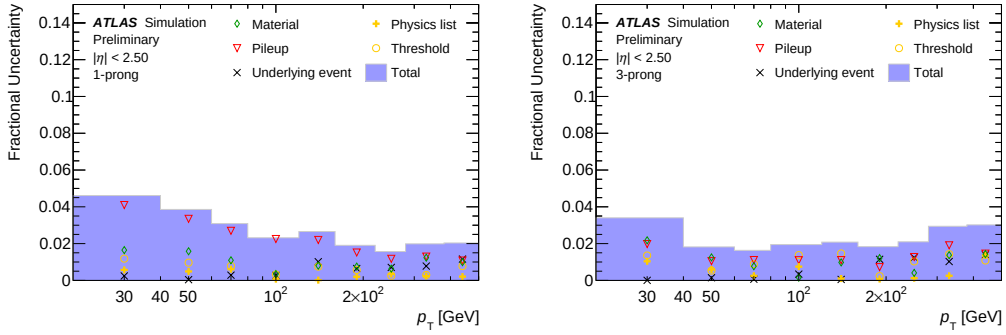

Figure 4.21: Systematic uncertainties of the reconstruction of hadronically decaying tau leptons as a function of the tau η for (left) 1-prong taus and (right) 3-prong taus [96].

Tau identification efficiencies in data and simulation agree to a level that the correction scale factors are compatible with unity. Tau identification uncertainty of the "medium" working point is around 5% and 6% for 1-prong and 3-prong tau candidates, respectively. This uncertainty applies for tau candidates with $p_{\mathrm{T}} \lesssim 100\,\mathrm{GeV}$ because it is measured in the tag-and-probe analysis using $Z \to \tau_{\mathrm{had}}\tau_{\mu}$ events and therefore is limited in the $\tau_{\text{had-vis}}$ p_{T} range. Tau identification uncertainty for tau candidates with higher transverse momentum is inflated and grows with the $\tau_{\text{had-vis}}$ p_{T}.

The electron discrimination performance has been measured in a tag-and-probe analysis using $Z \to ee$ events. The electron discrimination uncertainty is up to 6% the largest being around $\eta \approx 0$ and $|\eta| \approx 2.5$, i.e. at the edges of the inner detector.

Tau energy scale (TES) has been measured in the in-situ tag-and-probe

analysis [98]. Distribution of the visible mass, m_{vis}, around the Z mass peak in $Z \to \tau_{\text{had}}\tau_{\mu}$ events is sensitive to shifts in TES. The tau energy is parametrized as $E_{\text{T,scaled}} = (1+\alpha)E_{\text{T}}$ by introducing a scale parameter α, while the muon energy is measured independently with high precision. The best fit value of α is extracted from a χ^2 fit of the m_{vis} distribution in data and simulation. For the BRT tau energy calibration, the TES scale parameter α is around 1% and -3% for $\tau_{\text{had-vis}}$ with one and three associated tracks, respectively. The uncertainties on the TES are similarly around 1% and 3% for $\tau_{\text{had-vis}}$ with one and three associated tracks, respectively. These uncertainties arise from the background modeling in the in-situ analysis, tau energy resolution and muon reconstruction. In addition to the total uncertainty from the in-situ measurement, TES uncertainty is also affected by uncertainties of detector response to a single particle and of energy thresholds in object selection definitions.

Fake Factor Uncertainties

Systematic uncertainties in lepton and tau fake factors arise from background modeling uncertainties in the control regions where they were measured. The electron fake factors have uncertainties ranging from a few percent at low transverse momentum to up to 60% at high transverse momentum depending on the category and $\Delta\phi$ bin. Large uncertainty at high electron p_{T} is due to large background contamination in the control region which makes fake factors sensitive to background modeling. The muon fake factors have uncertainties of a few percent at low muon p_{T}. At high muon transverse momentum the fake factors have very low values but the uncertainties are quite large due to sensitivity to background modeling as in the electron case. The fake factors of jets faking taus have uncertainties of up to 20% arising almost exclusively from statistics of the sample size of the control regions. These fake factors are insensitive to background modeling in the control regions because the regions are very pure in the signal (fake tau) component.

4.10.2 Theoretical Uncertainties

The simulated background samples of top-quark and di-boson processes have a 6% uncertainty on their theoretical cross sections. Additionally, top-quark samples are affected by uncertainties in the parton shower model, initial- and final-state radiation and the MC tune. Uncertainty due to the hadronization model is evaluated by comparing $t\bar{t}$ samples interfaced to the default Pythia 6 model with an alternative

HERWIG++ [160] model.

Background samples of the Z/γ^*+*jets* processes have dedicated normalization uncertainties, taken from [161], which take into account errors on the strong coupling constant α_s, beam energy, choice of parton distribution functions, mass scale of the Z boson and electroweak and photon-induced corrections.

Signal Acceptance Uncertainties

The simulated signal samples are affected by several sources of systematic uncertainties. In particular, the sources comprise variations of factorisation and renormalisation scales up and down by a factor of two, either coherently or oppositely; modeling of initial- and final-state radiation as well as the underlying event, which were estimated from the variations of the A14 and AZNLO tunes (see section 4.2 for the description of MC simulation); alternative sets of PDFs. Total acceptance uncertainty for the gluon-gluon fusion process with resonance masses between 200 GeV and 2250 GeV ranges from 18% to 28%, respectively. For the b-associated production mode the uncertainty ranges from 40% to 50% for the same generated mass spectrum.

4.11 Results

The likelihood function is formed from the total transverse mass histogram bins in the four categories of the Signal Region and two channels in the Top Control Region: in total 32 bins. The input histograms were used as building blocks in the HISTFACTORY [162] package to construct the statistical model. The model fitting and exclusion limits were obtained using ROOFIT and ROOSTATS packages. The data was found to be in good agreement with the prediction of the background-only hypothesis. The total transverse mass distributions after the fitting procedure with a $\mu = 0$ condition are shown in Fig. 4.22, 4.23 and 4.24. In those plots the overlaid signal is normalized to the cross section which is at the exclusion limit in the hMSSM scenario (exclusion limits are presented below). For the $m_A = 600$ GeV mass point the exclusion limit is at $\tan\beta \approx 10$ which provides the total H/A production cross section of ≈ 29.8 fb. For the $m_A = 1000$ GeV mass point the exclusion limit is at $\tan\beta \approx 30$ which provides the total H/A production cross section of ≈ 20.2 fb. The event yields and their total uncertainties are listed in Tables 4.6 and 4.7.

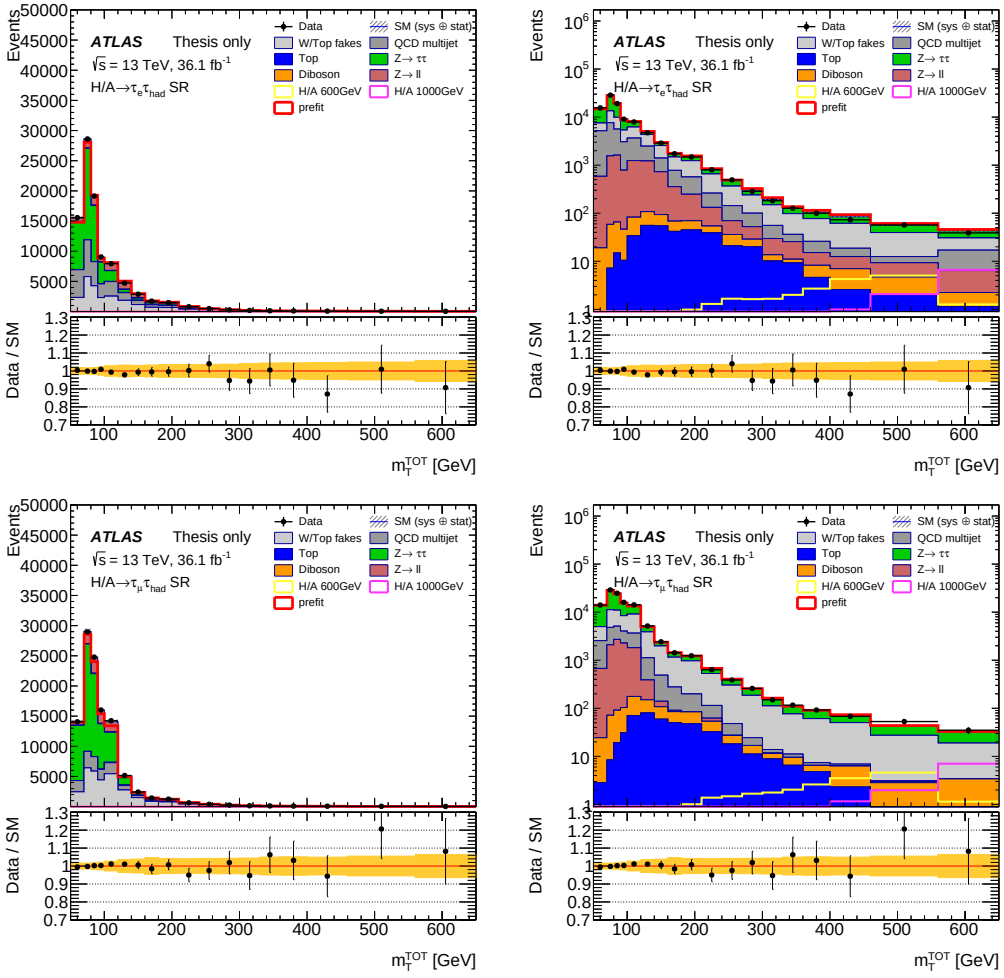

Figure 4.22: Post-fit distributions of the total transverse mass in the b-veto category of the (top) electron and (bottom) muon channels displayed in (left) linear and (right) logarithmic scales. The ratio of the data and the expected background events is shown in the lower panel of each subplot. Statistical and systematic uncertainties are included in the error band.

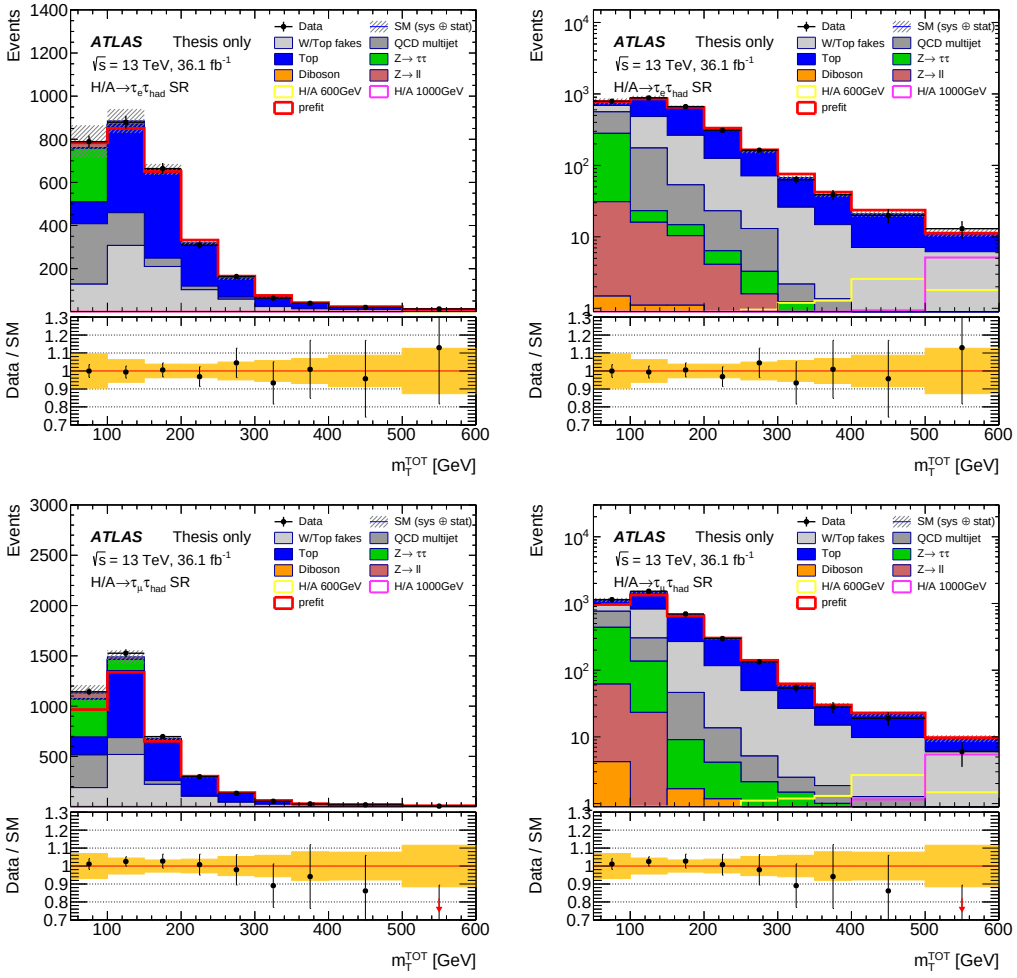

Figure 4.23: Post-fit distributions of the total transverse mass in the b-tag category of the (top) electron and (bottom) muon channels displayed in (left) linear and (right) logarithmic scales. The ratio of the data and the expected background events is shown in the lower panel of each subplot. Statistical and systematic uncertainties are included in the error band.

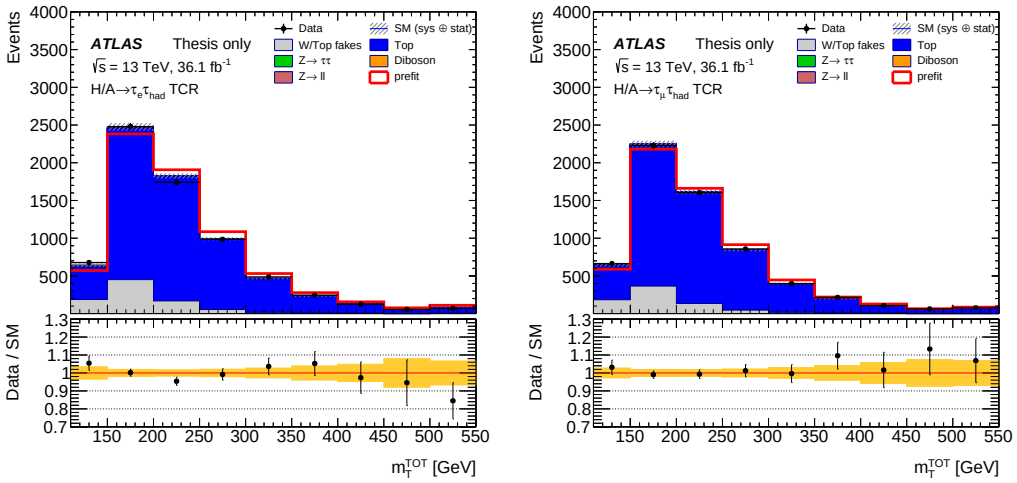

Figure 4.24: Post-fit distributions of the total transverse mass in the Top control region of the (left) electron and (right) muon channels. The ratio of the data and the expected background events is shown in the lower panel of each subplot. Statistical and systematic uncertainties are included in the error band.

Table 4.6: Event yields in the Signal Region after the fitting procedure. Event yields are listed for the electron and muon channels b-veto and b-tag categories. The uncertainties include statistical and systematic uncertainties. The uncertainties of the individual background components do not add up to the total uncertainty because they are correlated.

Process \ Category	$\tau_e\tau_{had}$		$\tau_\mu\tau_{had}$	
	b-veto	b-tag	b-veto	b-tag
W/Top fakes	22700 ± 1300	850 ± 110	31700 ± 1500	1130 ± 120
QCD multi-jet	22300 ± 1200	500 ± 110	12100 ± 1400	544 ± 91
Top	373 ± 37	1263 ± 42	454 ± 46	1582 ± 55
$Z/\gamma^* \to \tau\tau$	39700 ± 540	267 ± 31	55840 ± 740	506 ± 41
$Z/\gamma^* \to ll$	7930 ± 310	59.4 ± 8.4	9390 ± 490	80 ± 14
Diboson	404 ± 29	4.7 ± 0.9	578 ± 41	8.5 ± 2.0
Total background	93400 ± 300	2947 ± 45	110000 ± 350	3850 ± 56
Data	93256	2939	110109	3904

Table 4.7: Event yields in the Top Control Region after the fitting procedure. Event yields are listed for the electron and muon channels. The uncertainties include statistical and systematic uncertainties. The uncertainties of the individual background components do not add up to the total uncertainty because they are correlated.

Process \ Category	$\tau_{\mathrm{e}}\tau_{\mathrm{had}}$	$\tau_{\mu}\tau_{\mathrm{had}}$
W/Top fakes	892 ± 55	760 ± 48
Top	5943 ± 88	5381 ± 81
$Z/\gamma^* \to \tau\tau$	5.9 ± 0.9	14.1 ± 3.8
$Z/\gamma^* \to ll$	39 ± 20	2.3 ± 0.6
Diboson	23.7 ± 3.5	17.6 ± 3.3
Total background	6904 ± 70	6175 ± 63
Data	6861	6205

For the exclusion limits, a modified frequentist method [163] is used to set 95% confidence level (CL_s) upper limits on the cross section times branching ratio of the Higgs boson. The exclusion limits on the signal strength parameter μ is used with Eq. 4.9.1 to extract the exclusion limit of expected signal events and consequently translate it to the cross section times branching ratio limits. The limits as a function of Higgs boson mass are shown in Fig. 4.25 for the two Higgs boson production modes. The observed limits show a good overall agreement with the expected limits within 2σ uncertainty. In the gluon-gluon fusion mode the observed limits are tighter than expected for masses below 600 GeV. This can be explained by a small deficit of data events in the b-veto category of the $\tau_\mu\tau_{\text{had}}$ channel between 200 and 350 GeV and of the $\tau_{\text{e}}\tau_{\text{had}}$ channel between 300 and 450 GeV, see Fig. 4.22. The observed limit agrees very well with the expected one above 600 GeV because almost all high-mass signal events fall into the last bin of the m_T^{tot} distribution which is predicted accurately by the background model. In the b-associated production mode the observed limits are tighter than expected across the whole mass range. This can be explained by the small deficits in the b-veto category, the same as for the gluon-gluon mode, and also small deficit of data events in the b-tag category of the $\tau_\mu\tau_{\text{had}}$ channel, see Fig. 4.23.

Additionally, exclusion limit plots show the expected signal sensitivity in the b-tag and b-veto categories separately. The gluon-gluon fusion production mode does not have sensitivity in the b-tag category (which also includes the TCR) because of the b-tagged jet requirement. The b-associated production mode have comparable sensitivity in both categories with b-tag being stronger due to the 70% b-tagging efficiency which leaves only 30% of the signal events in the b-veto category.

The resulting cross section times branching fraction exclusion limits are interpreted in MSSM. The exclusion limits of $m_A - \tan\beta$ parameter space in MSSM are shown in Fig. 4.26 for the $m_{\text{h}}^{\text{mod}-}$ and hMSSM benchmark scenarios. In these scenarios the signal contribution consists of both production modes and the fraction of each mode's contribution depends on the parameter values in the plane. The b-associated production mode is contributing more at higher values of $\tan\beta$. In order to take this fraction dependence into account the fit was performed for every mass point with various relative signal contributions from both production modes. Then, the resulting exclusion limits are compared to a signal fraction and a cross section that are predicted from a benchmark scenario corresponding to a point in the $m_A - \tan\beta$ parameter space. If the excluded cross section times branching fraction is smaller than what is predicted by a benchmark scenario, the point is

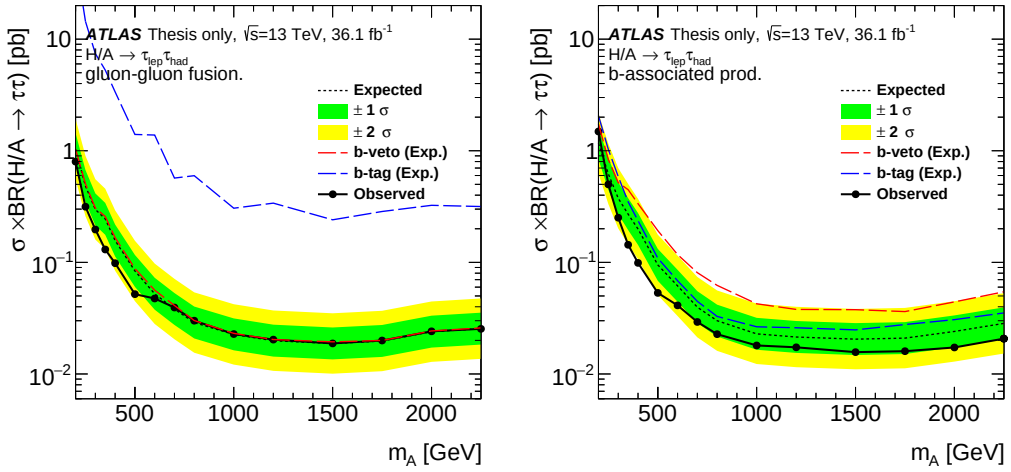

Figure 4.25: Higgs boson production cross-section times branching fraction to a pair of tau leptons 95% confidence level upper limits. The expected and observed limits are shown for the (left) gluon-gluon fusion and (right) b-associated production modes. The signal sensitivity in the b-veto and b-tag categories are indicated by the expected exclusion limits derived separately in those categories.

excluded.

The plots show tighter observed limits than expected which is a consequence of tighter exclusion limits on cross section times branching ratio. The limits in the hMSSM scenario are more stringent due to higher branching ratio to tau leptons; in the $m_{\mathrm{h}}^{\mathrm{mod}-}$ scenario the presence of light neutralinos reduce the branching ratio to taus. In the hMSSM scenario $\tan\beta > 1$ is excluded at Higgs boson masses from 200 to 350 GeV except for a small area at 200 GeV around $\tan\beta \approx 5$. The limits become less stringent above 350 GeV because a Higgs boson decay channel to a pair of top-quarks opens up.

4.12 Conclusions

Using the 36.1 fb^{-1} data set collected in 2015 and 2016 with the ATLAS detector during Run 2 of the LHC at $\sqrt{s} = 13$ TeV, a search for the heavy neutral MSSM Higgs bosons was performed. The Higgs bosons were assumed to be produced either in gluon-gluon fusion or b-associated production modes, and subsequently decay into a pair of tau leptons. The Higgs bosons were searched for in the decay channel where one tau decays leptonically, with either an electron or a muon

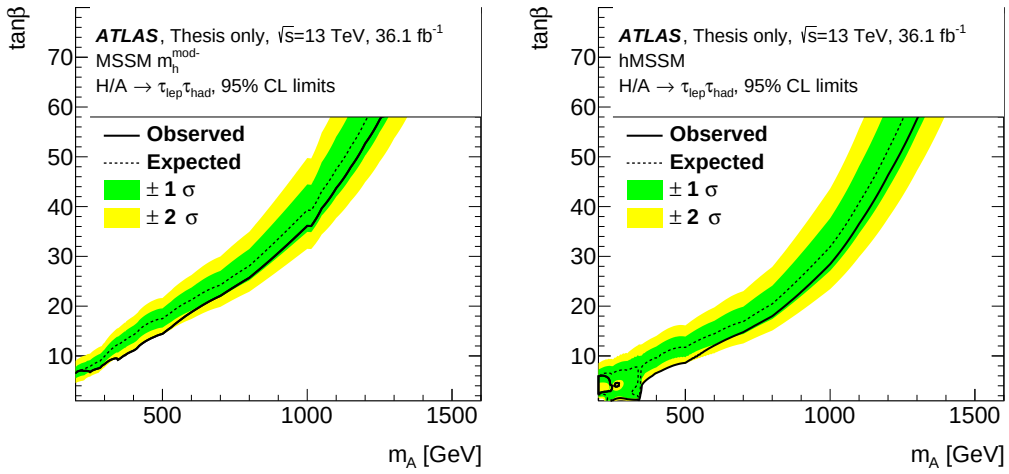

Figure 4.26: 95% confidence level exclusion limits in the $m_A - \tan\beta$ parameter space of the MSSM. The expected and observed limits are shown for the (left) $m_{\mathrm{h}}^{\mathrm{mod-}}$ and (right) hMSSM benchmark scenarios. The values of parameters above the observed line are excluded.

in the final state, and another tau decays hadronically. The di-tau mass spectrum modeled with the total transverse mass variable serves as the discriminating variable and ensures large signal to background ratio. The mass range for this search was between 200 GeV and 2250 GeV. The selected events are categorized into events containing at least one b-tagged jet and into events without a single b-tagged jet. This categorization improves signal sensitivity for the b-associated production mode. Background processes were modeled either with Monte Carlo samples or data-driven Fake Factor method. Additionally, a control region enriched in top-quark events is introduced in the final fitting procedure in order to constrain systematic uncertainties related to the top-quark modeling.

No significant excess of events was observed above the expected background from Standard Model processes. As a consequence, 95% Confidence Level upper limits on the cross section times branching ratio were obtained for the two production modes of the Higgs bosons. Cross section times branching ratio above 0.8 pb at a Higgs boson mass of 200 GeV and above 0.03 pb at a mass of 2250 GeV are excluded in the gluon-gluon fusion production mode. In the b-associated production mode, the excluded cross section times branching ratio are above 1.3 pb at a mass of 200 GeV and above 0.02 pb at a mass of 2250 GeV.

The obtained cross section limits were interpreted in $m_{\mathrm{h}}^{\mathrm{mod-}}$ and hMSSM

benchmark scenarios of the MSSM, and 95% Confidence Level exclusion limits in the two-dimensional $m_A - \tan\beta$ parameters space were extracted. In the $m_{\mathrm{h}}^{\mathrm{mod}-}$ benchmark scenario the $\tan\beta$ parameter value above 6 is excluded at $m_A = 200\,\mathrm{GeV}$ and above 35 at $m_A = 1000\,\mathrm{GeV}$. In the hMSSM benchmark scenario the $\tan\beta$ parameter value above 1 is excluded at $m_A = 200\,\mathrm{GeV}$ except for a small region around $\tan\beta = 3$. At $m_A = 1000\,\mathrm{GeV}$, $\tan\beta$ above 28 is excluded. The exclusion limits are less stringent in the $m_{\mathrm{h}}^{\mathrm{mod}-}$ benchmark scenario due to the presence of low mass neutralinos which open up a decay mode for the Higgs bosons at low values of $\tan\beta$.

Appendix A

Lepton Fake Factors

The remaining plots of the lepton fake factors not shown in the main text are presented here.

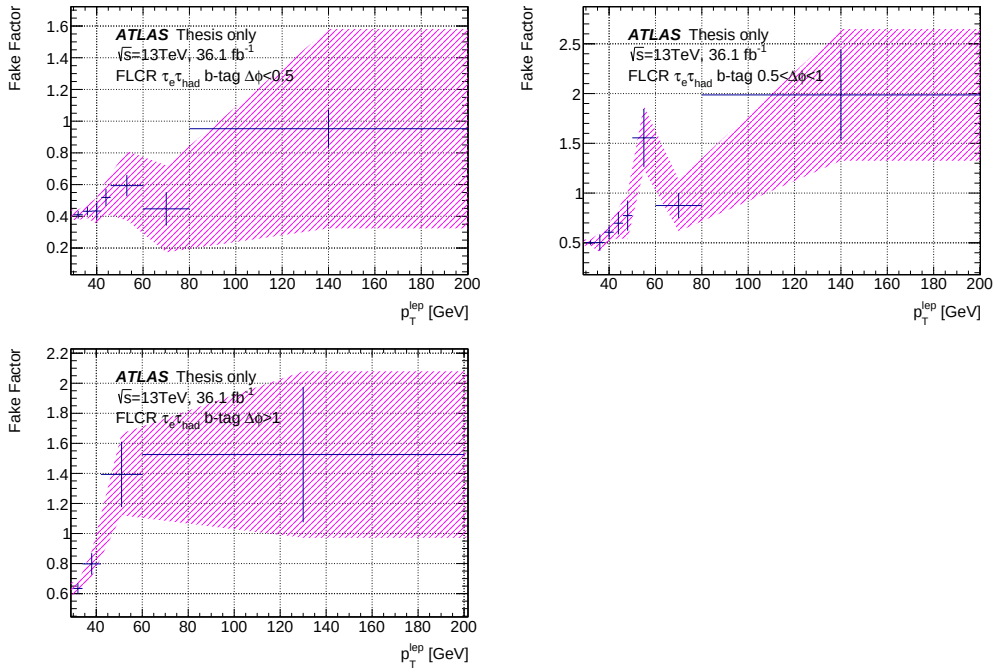

Figure A.1: $Jet \rightarrow e$ fake factors in the b-tag category, parameterized in electron momentum and $\Delta\phi^{\tau_e, E_T^{miss}}$. The error bars indicate statistical uncertainty and the error bands indicate total uncertainty.

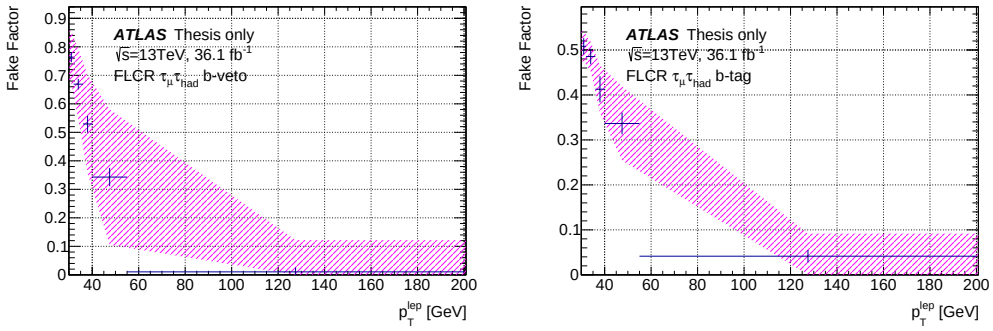

Figure A.2: $Jet \rightarrow \mu$ fake factors in the (left) b-veto and (right) b-tag categories, parameterized in muon momentum. The error bars indicate statistical uncertainty and the error bands indicate total uncertainty.

Appendix B

Nuisance Parameters

This section presents a summary of information related to nuisance parameters that were relevant in the analysis. Only those nuisance parameter that survived pruning are discussed here. Fig. B.1, the pull plot, shows how much the best fit value of a nuisance parameter is different from the central value. Sorting of the parameters is in descending order such that the largest pull is on the left side of the plot; this ordering has no relevance to the analysis. The meaning of nuisance parameters is explained below.

- `TTBAR_ShowerUE`: parton shower model uncertainty in the $t\bar{t}$ background;
- `TTBAR_Radiation`: initial- and final-state radiation uncertainty in the $t\bar{t}$ background;
- `JET_JER_SINGLE_NP`: jet energy resolution uncertainty;
- `JET_GroupedNP_`i: component i of the grouped uncertainties related to jets;
- `jet_jvtineff`: uncertainty of the JVT in-efficiency;
- `TAUS_TRUEHADTAU_SME_TES_MODEL`: tau energy scale uncertainty arising from the tau simulation;
- `TAUS_TRUEHADTAU_SME_TES_INSITU`: tau energy scale uncertainty arising from the in-situ measurements;
- `TAUS_TRUEHADTAU_SME_TES_DETECTOR`: tau energy scale uncertainty arising from the detector modeling;

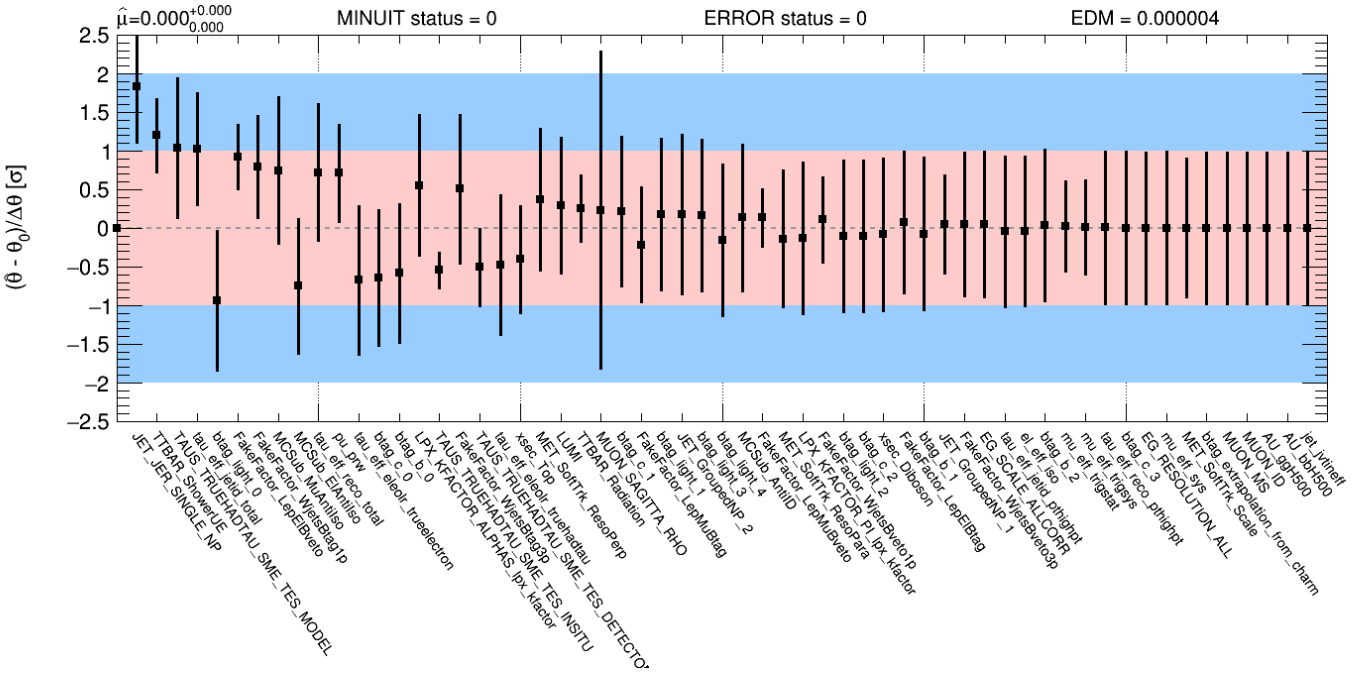

Figure B.1: Relative difference between the best fit value and the central value of a nuisance parameter.

- `tau_eff_jetid_total`: tau identification uncertainty;
- `tau_eff_jetid_pthighpt`: tau identification uncertainty for high energy tau candidates;
- `tau_eff_reco_total`: tau reconstruction uncertainty;
- `tau_eff_reco_pthighpt`: tau reconstruction uncertainty for high energy tau candidates;
- `tau_eff_eleolr_trueelectron`: electron veto uncertainty arising from a real electron;
- `tau_eff_eleolr_truehadtau`: electron veto uncertainty arising from a real hadronic tau;
- `EG_SCALE_ALLCORR`: electron energy scale uncertainty;
- `EG_RESOLUTION_ALL`: electron energy resolution uncertainty;
- `el_eff_iso`: electron isolation uncertainty;

- `mu_eff_trigstat`: statistical component of the uncertainty of the muon trigger efficiency;
- `mu_eff_trigsys`: systematic component of the uncertainty of the muon trigger efficiency;
- `mu_eff_sys`: muon reconstruction uncertainty;
- `MUON_MS`: variations in the smearing of the ID tracks of muons;
- `MUON_ID`: variations in the smearing of the MS tracks of muons;
- `MUON_SAGITTA_RHO`: variations in the scale of the muon momentum (charge dependent);
- `MET_SoftTrk_ResoPerp`: $E_{\mathrm{T}}^{\mathrm{miss}}$ resolution uncertainty arising from the soft-term component and perpendicular projection;
- `MET_SoftTrk_ResoPara`: $E_{\mathrm{T}}^{\mathrm{miss}}$ resolution uncertainty arising from the soft-term component and parallel projection;
- `MET_SoftTrk_Scale`: $E_{\mathrm{T}}^{\mathrm{miss}}$ scale uncertainty arising from the soft-term component;
- `btag_light_`i: component i of the b-tagging uncertainty for light-quark initiated jets;
- `btag_c_`i: component i of the b-tagging uncertainty for c-quark initiated jets;
- `btag_b_`i: component i of the b-tagging uncertainty for b-quark initiated jets;
- `btag_extrapolation_from_charm`: b-tagging uncertainty derived from a sample enriched in c-quark initiated jets.
- `pu_prw`: pile-up re-weighting uncertainty;
- `LPX_KFACTOR_ALPHAS_lpx_kfactor`: Z/γ^{*}+$jets$ background cross-section uncertainty arising from α_s;
- `LPX_KFACTOR_PI_lpx_kfactor`: Z/γ^{*}+$jets$ background cross-section uncertainty arising from photon-induced corrections;
- `xsec_Top`: Top-quark background cross-section uncertainty;

- `xsec_Diboson`: Diboson background cross-section uncertainty;
- `LUMI`: uncertainty of the total integrated luminosity;
- `FakeFactor_LepElBveto`: $jet \rightarrow lepton$ fake factor uncertainty in the electron channel b-veto category;
- `FakeFactor_LepMuBveto`: $jet \rightarrow lepton$ fake factor uncertainty in the muon channel b-veto category
- `FakeFactor_LepElBtag`: $jet \rightarrow lepton$ fake factor uncertainty in the electron channel b-tag category
- `FakeFactor_LepMuBtag`: $jet \rightarrow lepton$ fake factor uncertainty in the muon channel b-tag category
- `FakeFactor_WjetsBveto1p`: $jet \rightarrow \tau_{\text{had}}$ fake factor uncertainty for 1-prong τ_{had} candidates in b-veto categories;
- `FakeFactor_WjetsBtag1p`: $jet \rightarrow \tau_{\text{had}}$ fake factor uncertainty for 1-prong τ_{had} candidates in b-tag categories;
- `FakeFactor_WjetsBtag3p`: $jet \rightarrow \tau_{\text{had}}$ fake factor uncertainty for 3-prong τ_{had} candidates in b-tag categories;
- `MCSub_MuAntiIso`: background uncertainty in the muon channel anti-iso region used for QCD multi-jet background estimation;
- `MCSub_ElAntiIso`: background uncertainty in the electron channel anti-iso region used for QCD multi-jet background estimation;
- `MCSub_AntiID`: background uncertainty in the anti-id region used for W/Top fakes background estimation;
- `AU_ggH500`: acceptance uncertainty of the gluon-gluon fusion signal yield (one parameter for each mass point; does not affect the conditional $\mu = 0$ fit);
- `AU_bbH500`: acceptance uncertainty of the b-associated production signal yield (one parameter for each mass point; does not affect the conditional $\mu = 0$ fit).

Bibliography

[1] ATLAS Collaboration. "Search for Minimal Supersymmetric Standard Model Higgs bosons H/A and for a Z' boson in the $\tau\tau$ final state produced in pp collisions at $\sqrt{s} = 13$ TeV with the ATLAS Detector". In: *Eur.Phys.J.* C76 (2016), p. 585. DOI: 10.1140/EPJC/S10052-016-4400-6.

[2] The ATLAS Collaboration. "Search for additional heavy neutral Higgs and gauge bosons in the ditau final state produced in 36 fb^{-1} of pp collisions at $\sqrt{s} = 13$ TeV with the ATLAS detector". In: *JHEP* 1801 (2017), p. 55. DOI: 10.1007/JHEP01(2018)055. arXiv: 1709.07242.

[3] Sheldon L. Glashow. "Partial-symmetries of weak interactions". In: *Nuclear Physics* 22.4 (1961), pp. 579–588. ISSN: 0029-5582. DOI: 10.1016/0029-5582(61)90469-2.

[4] Steven Weinberg. "A Model of Leptons". In: *Physical Review Letters* 19.21 (1967), pp. 1264–1266. ISSN: 0031-9007. DOI: 10.1103/PhysRevLett.19.1264.

[5] A Salam. "Elementary Particle Physics: Relativistic Groups and Analyticity". In: *Eighth Nobel Symposium*. Ed. by N Svartholm. Almquvist and Wiksell, 1968, p. 367.

[6] P.W. Higgs. "Broken symmetries, massless particles and gauge fields". In: *Physics Letters* 12.2 (1964), pp. 132–133. ISSN: 0031-9163. DOI: 10.1016/0031-9163(64)91136-9.

[7] F. Englert and R. Brout. "Broken Symmetry and the Mass of Gauge Vector Mesons". In: *Physical Review Letters* 13.9 (1964), pp. 321–323. ISSN: 0031-9007. DOI: 10.1103/PhysRevLett.13.321.

[8] Tatsumi Aoyama et al. "Tenth-Order Electron Anomalous Magnetic Moment — Contribution of Diagrams without Closed Lepton Loops". In: *Phys. Rev.* D91.3 (2015), p. 33006. DOI: 10.1103/PhysRevD.91.033006. arXiv: 1412.8284 [hep-ph].

[9] D Hanneke, S Fogwell Hoogerheide, and G Gabrielse. "Cavity control of a single-electron quantum cyclotron: Measuring the electron magnetic moment". In: *Phys. Rev. A* 83.5 (2011), p. 52122. DOI: 10.1103/PhysRevA.83.052122.

[10] *Standard Model Particles*. https://en.wikipedia.org/wiki/Standard_Model. (Visited on 01/01/2019).

[11] M. Tanabashi et al. "Review of Particle Physics". In: *Phys. Rev. D* 98.3 (2018), p. 30001. DOI: 10.1103/PhysRevD.98.030001.

[12] LHCb Collaboration. "Observation of $J/\psi p$ resonances consistent with pentaquark states in $\Lambda_b^0 \to J/\psi K^- p$ decays". In: *Physical Review Letters* 115.7 (2015), p. 072001. ISSN: 0031-9007. DOI: 10.1103/PhysRevLett.115.072001. arXiv: 1507.03414.

[13] G Cotugno et al. "Charmed Baryonium". In: *Physical Review Letters* 104.13 (2009), p. 132005. ISSN: 0031-9007. DOI: 10.1103/PhysRevLett.104.132005. arXiv: 0911.2178.

[14] LHCb Collaboration. "Observation of the resonant character of the $Z(4430)^-$ state". In: *Physical Review Letters* 112.22 (2014), p. 222002. ISSN: 0031-9007. DOI: 10.1103/PhysRevLett.112.222002. arXiv: 1404.1903.

[15] M. L. Perl et al. "Evidence for Anomalous Lepton Production in e^+ - e^- Annihilation". In: *Physical Review Letters* 35.22 (1975), pp. 1489–1492. ISSN: 0031-9007. DOI: 10.1103/PhysRevLett.35.1489.

[16] ATLAS Collaboration. "Observation of a new particle in the search for the Standard Model Higgs boson with the ATLAS detector at the LHC". In: *Phys.Lett.* B716 (2012), pp. 1–29. DOI: 10.1016/J.PHYSLETB.2012.08.020.

[17] CMS Collaboration. "Observation of a new boson at a mass of 125 GeV with the CMS experiment at the LHC". In: *Phys.Lett.* B716 (2012), pp. 30–61. DOI: 10.1016/J.PHYSLETB.2012.08.021.

[18] I. J. R. Aitchison and A. J. G. Hey. *Gauge theories in particle physics: A practical introduction. Vol. 2: Non-Abelian gauge theories: QCD and the electroweak theory*. Bristol, UK: CRC Press, 2012. ISBN: 9781466513075.

[19] Nicola Cabibbo. "Unitary Symmetry and Leptonic Decays". In: *Phys. Rev. Lett.* 10 (1963), pp. 531–533. DOI: 10.1103/PhysRevLett.10.531.

[20] Makoto Kobayashi and Toshihide Maskawa. "CP Violation in the Renormalizable Theory of Weak Interaction". In: *Prog. Theor. Phys.* 49 (1973), pp. 652–657. DOI: 10.1143/PTP.49.652.

[21] J. H. Christenson et al. "Evidence for the 2π Decay of the K_2^0 Meson". In: *Physical Review Letters* 13.4 (1964), pp. 138–140. ISSN: 0031-9007. DOI: 10.1103/PhysRevLett.13.138.

[22] LHCb Collaboration. "Observation of *CP* violation in charm decays". In: (2019). arXiv: 1903.08726.

[23] LHCb Collaboration. "First observation of CP violation in the decays of Bs mesons". In: *Physical Review Letters* 110.22 (2013), p. 221601. ISSN: 0031-9007. DOI: 10.1103/PhysRevLett.110.221601. arXiv: 1304.6173.

[24] Andrei D Sakharov. "Violation of CP invariance, C asymmetry, and baryon asymmetry of the universe". In: *Soviet Physics Uspekhi* 34.5 (1991), pp. 392–393. ISSN: 0038-5670. DOI: 10.1070/PU1991v034n05ABEH002497.

[25] B Pontecorvo. "Inverse beta processes and nonconservation of lepton charge". In: *Sov. Phys. JETP* 7 (1958), pp. 172–173.

[26] Ziro Maki, Masami Nakagawa, and Shoichi Sakata. "Remarks on the unified model of elementary particles". In: *Prog. Theor. Phys.* 28 (1962), pp. 870–880. DOI: 10.1143/PTP.28.870.

[27] Ivan Esteban et al. "Global analysis of three-flavour neutrino oscillations: synergies and tensions in the determination of θ_{23}, δ_{CP}, and the mass ordering". In: *Journal of High Energy Physics* 2019.1 (2018), p. 106. ISSN: 1029-8479. DOI: 10.1007/JHEP01(2019)106. arXiv: 1811.05487.

[28] G Altarelli and G Parisi. "Asymptotic freedom in parton language". In: *Nuclear Physics B* 126.2 (1977), pp. 298–318. ISSN: 0550-3213. DOI: 10.1016/0550-3213(77)90384-4.

[29] *Martin-Stirling-Thorne-Watt Parton Distribution Functions*. http://mstwpdf.hepforge.org. (Visited on 01/01/2019).

[30] *W.J. Stirling, private communication*. URL: http://www.hep.ph.ic.ac.uk/~wstirlin/plots/plots.html (visited on 01/01/2019).

[31] Stephen P Martin. “A Supersymmetry primer”. In: (1997), pp. 1–98. arXiv: hep-ph/9709356 [hep-ph].

[32] Planck Collaboration. “Planck 2018 results. VI. Cosmological parameters”. In: (2018). arXiv: 1807.06209.

[33] The LHCb Collaboration. “Measurement of the ratio of branching fractions $\mathcal{B}(\bar{B}^0 \to D^{*+}\tau^-\bar{\nu}_\tau)/\mathcal{B}(\bar{B}^0 \to D^{*+}\mu^-\bar{\nu}_\mu)$”. In: *Physical Review Letters* 115.15 (2015), p. 159901. DOI: 10.1103/PhysRevLett.115.159901.

[34] Nima Arkani–Hamed, Savas Dimopoulos, and Gia Dvali. “The hierarchy problem and new dimensions at a millimeter”. In: *Physics Letters B* 429.3-4 (1998), pp. 263–272. ISSN: 03702693. DOI: 10.1016/S0370-2693(98)00466-3.

[35] ATLAS Collaboration. “Search for new phenomena in high-mass final states with a photon and a jet from pp collisions at $\sqrt{s} = 13$ TeV with the ATLAS detector”. In: *Eur.Phys.J.* C78 (2017), p. 102. DOI: 10.1140/EPJC/S10052-018-5553-2.

[36] I. J. R. Aitchison. *Supersymmetry in particle physics : an elementary introduction*. Cambridge : Cambridge University Press, 2007.

[37] H.P. Nilles. “Supersymmetry, supergravity and particle physics”. In: *Physics Reports* 110.1-2 (1984), pp. 1–162. ISSN: 0370-1573. DOI: 10.1016/0370-1573(84)90008-5.

[38] L. Girardello and M.T. Grisaru. “Soft breaking of supersymmetry”. In: *Nuclear Physics B* 194.1 (1982), pp. 65–76. ISSN: 0550-3213. DOI: 10.1016/0550-3213(82)90512-0.

[39] M Carena et al. “MSSM Higgs Boson Searches at the LHC: Benchmark Scenarios after the Discovery of a Higgs-like Particle”. In: *Eur. Phys. J.* C73.9 (2013), p. 2552. DOI: 10.1140/epjc/s10052-013-2552-1. arXiv: 1302.7033 [hep-ph].

[40] ATLAS Collaboration. *Combined measurements of Higgs boson production and decay using up to 80 fb^{-1} of proton–proton collision data at $\sqrt{s} = 13$ TeV collected with the ATLAS experiment*. Tech. rep. ATLAS-COM-CONF-2018-029. Geneva: CERN, 2018. URL: https://cds.cern.ch/record/2625365.

[41] ATLAS Collaboration. "Search for supersymmetry in events with b-tagged jets and missing transverse momentum in pp collisions at $\sqrt{s} = 13$ TeV with the ATLAS detector". In: *JHEP* 1711 (2017), p. 195. DOI: 10.1007/JHEP11(2017)195. arXiv: 1708.09266.

[42] ATLAS Collaboration. "Search for top squarks decaying to tau sleptons in pp collisions at $\sqrt{s} = 13$ TeV with the ATLAS detector". In: *Phys.Rev.* D98 (2018), p. 032008. DOI: 10.1103/PHYSREVD.98.032008.

[43] A Djouadi et al. "The post-Higgs MSSM scenario: Habemus MSSM?" In: *Eur. Phys. J.* C73 (2013), p. 2650. DOI: 10.1140/epjc/s10052-013-2650-0. arXiv: 1307.5205 [hep-ph].

[44] *Summary plots from the ATLAS Higgs physics group*. URL: https://atlas.web.cern.ch/Atlas/GROUPS/PHYSICS/CombinedSummaryPlots/HIGGS/ (visited on 01/01/2019).

[45] Frank Krauss and Davide Napoletano. "Towards a fully massive five-flavor scheme". In: *Physical Review D* 98.9 (2018), p. 096002. ISSN: 2470-0010. DOI: 10.1103/PhysRevD.98.096002. arXiv: 1712.06832.

[46] ATLAS Collaboration. "Search for charged Higgs bosons decaying via $H^{\pm} \to \tau^{\pm}\nu_{\tau}$ in the τ+jets and τ+lepton final states with 36 fb^{-1} of pp collision data recorded at $\sqrt{s} = 13$ TeV with the ATLAS experiment". In: *JHEP* 1809 (2018), p. 139. DOI: 10.1007/JHEP09(2018)139. arXiv: 1807.07915.

[47] ATLAS Collaboration. "Search for charged Higgs bosons decaying into top and bottom quarks at $\sqrt{s} = 13$ TeV with the ATLAS detector". In: *JHEP* 1811 (2018), p. 085. DOI: 10.1007/JHEP11(2018)085. arXiv: 1808.03599.

[48] The ATLAS Collaboration. "Search for heavy ZZ resonances in the $\ell^+\ell^-\ell^+\ell^-$ and $\ell^+\ell^-\nu\bar{\nu}$ final states using proton proton collisions at $\sqrt{s} = 13$ TeV with the ATLAS detector". In: (2017). DOI: 10.1140/epjc/s10052-018-5686-3. arXiv: 1712.06386.

[49] ATLAS Collaboration. "Search for heavy resonances decaying into WW in the $e\nu\mu\nu$ final state in pp collisions at $\sqrt{s} = 13$ TeV with the ATLAS detector". In: *Eur.Phys.J.* C78 (2017), p. 24. DOI: 10.1140/EPJC/S10052-017-5491-4.

[50] ATLAS Collaboration. "Search for resonant and non-resonant Higgs boson pair production in the $b\bar{b}\tau^+\tau^-$ decay channel in pp collisions at $\sqrt{s} = 13$ TeV with the ATLAS detector". In: (2018). DOI: 10.1103/PhysRevLett.121.191801. arXiv: 1808.00336.

[51] ATLAS Collaboration. "Search for heavy resonances decaying into a W or Z boson and a Higgs boson in final states with leptons and b-jets in 36 fb^{-1} of $\sqrt{s} = 13$ TeV pp collisions with the ATLAS detector". In: *JHEP* 1803 (2017), p. 174. DOI: 10.1007/JHEP11(2018)051.

[52] CMS Collaboration. "Searches for a heavy scalar boson H decaying to a pair of 125 GeV Higgs bosons hh or for a heavy pseudoscalar boson A decaying to Zh, in the final states with h to tau tau". In: *Physics Letters B* 755 (2015), pp. 217–244. ISSN: 03702693. DOI: 10.1016/j.physletb.2016.01.056. arXiv: 1510.01181.

[53] CMS Collaboration. "Search for a pseudoscalar boson decaying into a Z boson and the 125 GeV Higgs boson in llbb final states". In: *Physics Letters B* 748 (2015), pp. 221–243. ISSN: 03702693. DOI: 10.1016/j.physletb.2015.07.010. arXiv: 1504.04710.

[54] CMS Collaboration. "Search for additional neutral MSSM Higgs bosons in the $\tau\tau$ final state in proton-proton collisions at $\sqrt{s} = 13$ TeV". In: *Journal of High Energy Physics* 2018.9 (2018), p. 7. ISSN: 1029-8479. DOI: 10.1007/JHEP09(2018)007. arXiv: 1803.06553.

[55] CMS Collaboration. "Search for beyond the standard model Higgs bosons decaying into a $b\bar{b}$ pair in pp collisions at $\sqrt{s} = 13$ TeV". In: *Journal of High Energy Physics* 2018.8 (2018), p. 113. ISSN: 1029-8479. DOI: 10.1007/JHEP08(2018)113. arXiv: 1805.12191.

[56] CMS Collaboration. "Search for neutral MSSM Higgs bosons decaying to mu+ mu- in pp collisions at sqrt(s) = 7 and 8 TeV". In: *Physics Letters B* 752 (2015), pp. 221–246. ISSN: 03702693. DOI: 10.1016/j.physletb.2015.11.042. arXiv: 1508.01437.

[57] CMS Collaboration. "Search for a charged Higgs boson in pp collisions at sqrt(s) = 8 TeV". In: *Journal of High Energy Physics* 2015.11 (2015), p. 18. ISSN: 1029-8479. DOI: 10.1007/JHEP11(2015)018. arXiv: 1508.07774.

[58] CMS Collaboration. "Search for charged Higgs bosons produced in vector boson fusion processes and decaying into a pair of W and Z bosons using proton-proton collisions at sqrt(s) = 13 TeV". In: *Physical Review Letters* 119.14 (2017), p. 141802. ISSN: 0031-9007. DOI: 10.1103/PhysRevLett.119.141802. arXiv: 1705.02942.

[59] The ATLAS Collaboration. "The ATLAS Experiment at the CERN Large Hadron Collider". In: *Journal of Instrumentation* 3.08 (2008), S08003–S08003. ISSN: 1748-0221. DOI: 10.1088/1748-0221/3/08/S08003.

[60] *CERN Document Server*. URL: https://cds.cern.ch/collection/ATLAS (visited on 11/01/2018).

[61] *ECFA-CERN Workshop on Large Hadron Collider in the LEP tunnel*. CERN. Geneva: CERN, 1984. URL: http://cds.cern.ch/record/154938.

[62] *Superconducting Super Collider*. URL: https://en.wikipedia.org/wiki/Superconducting_Super_Collider (visited on 01/01/2019).

[63] *Tevatron*. URL: https://en.wikipedia.org/wiki/Tevatron (visited on 01/01/2019).

[64] *Large Electron-Positron Collider*. URL: https://en.wikipedia.org/wiki/Large_Electron-Positron_Collider (visited on 01/01/2019).

[65] Lyndon Evans and Philip Bryant. "LHC Machine". In: *Journal of Instrumentation* 3.08 (2008), S08001–S08001. ISSN: 1748-0221. DOI: 10.1088/1748-0221/3/08/S08001.

[66] *Illustration of the LHC Accelerator Complex*. URL: https://commons.wikimedia.org/wiki/File:Cern-accelerator-complex.svg (visited on 01/01/2019).

[67] CMS Collaboration. "The CMS experiment at the CERN LHC". In: *Journal of Instrumentation* 3.08 (2008), S08004–S08004. ISSN: 1748-0221. DOI: 10.1088/1748-0221/3/08/S08004.

[68] LHCb Collaboration. "The LHCb Detector at the LHC". In: *Journal of Instrumentation* 3.08 (2008), S08005–S08005. ISSN: 1748-0221. DOI: 10.1088/1748-0221/3/08/S08005.

[69] ALICE Collaboration. "The ALICE experiment at the CERN LHC". In: *Journal of Instrumentation* 3.08 (2008), S08002–S08002. ISSN: 1748-0221. DOI: 10.1088/1748-0221/3/08/S08002.

[70] *Worldwide LHC Computing Grid*. URL: https://home.cern/science/computing/grid (visited on 01/01/2019).

[71] ATLAS Collaboration. "The ATLAS Inner Detector commissioning and calibration". In: *Eur.Phys.J.* C70 (2010), pp. 787–821. DOI: 10.1140/EPJC/S10052-010-1366-7.

[72] M Capeans et al. *ATLAS Insertable B-Layer Technical Design Report*. Tech. rep. CERN-LHCC-2010-013. ATLAS-TDR-19. 2010. URL: http://cds.cern.ch/record/1291633.

[73] ATLAS Collaboration. "Readiness of the ATLAS Liquid Argon Calorimeter for LHC Collisions". In: *Eur.Phys.J.* C70 (2010), pp. 723–753. DOI: 10.1140/EPJC/S10052-010-1354-Y.

[74] ATLAS Collaboration. "Readiness of the ATLAS Tile Calorimeter for LHC collisions". In: *Eur.Phys.J.* C70 (2010), pp. 1193–1236. DOI: 10.1140/EPJC/S10052-010-1508-Y.

[75] The ATLAS Collaboration. "Commissioning of the ATLAS Muon Spectrometer with Cosmic Rays". In: *The European Physical Journal C* 70.3 (2010), pp. 875–916. ISSN: 1434-6044. DOI: 10.1140/epjc/s10052-010-1415-2. arXiv: 1006.4384.

[76] ATLAS Collaboration. "Performance of the ATLAS Trigger System in 2015". In: *Eur.Phys.J.* C77 (2016), p. 317. DOI: 10.1140/EPJC/S10052-017-4852-3.

[77] Andrew Aukerman and Tae Min Hong. "Commissioning and validation of the ATLAS Level-1 topological trigger". In: (2018), TUPHA070. DOI: 10.18429/JACOW-ICALEPCS2017-TUPHA070.

[78] Milene Calvetti and Nicolo Vladi Biesuz. "Integration and Commissioning of the ATLAS Fast TracKer system". In: *Proceedings of Sixth Annual Conference on Large Hadron Collider Physics — PoS(LHCP2018)*. Vol. LHCP2018. Sissa Medialab, 2018, p. 028. DOI: 10.22323/1.321.0028.

[79] The ATLAS Collaboration. "Performance of the ATLAS Trigger System in 2010". In: *Eur.Phys.J.* C72 (2012), p. 1849. DOI: 10.1140/EPJC/S10052-011-1849-1.

[80] ATLAS Collaboration. "Luminosity determination in pp collisions at $\sqrt{s} =$ 8 TeV using the ATLAS detector at the LHC". In: (2016). DOI: 10.1140/epjc/s10052-016-4466-1. arXiv: 1608.03953.

[81] ATLAS Collaboration. "Measurement of the Inelastic Proton-Proton Cross Section at $\sqrt{s} = 13$ TeV with the ATLAS Detector at the LHC". In: *Phys.Rev.Lett.* 117 (2016), p. 182002. DOI: 10.1103/PHYSREVLETT.117.182002.

[82] ATLAS Collaboration. *Measurement of the Higgs boson production cross section at 7, 8 and 13 TeV center-of-mass energies in the $H \to \gamma\gamma$ channel with the ATLAS detector*. Tech. rep. ATLAS-CONF-2015-060. Geneva: CERN, 2015. URL: https://cds.cern.ch/record/2114826.

[83] *Luminosity Public Results Run 2*. URL: https://twiki.cern.ch/twiki/bin/view/AtlasPublic/LuminosityPublicResultsRun2 (visited on 01/01/2019).

[84] ATLAS Collaboration. *Electron efficiency measurements with the ATLAS detector using the 2015 LHC proton-proton collision data*. Tech. rep. Geneva: CERN, 2016. URL: https://cds.cern.ch/record/2157687/.

[85] ATLAS Collaboration. *Improved electron reconstruction in ATLAS using the Gaussian Sum Filter-based model for bremsstrahlung*. Tech. rep. ATLAS-CONF-2012-047. Geneva: CERN, 2012. URL: http://cds.cern.ch/record/1449796.

[86] ATLAS Collaboration. *Electron and photon energy calibration with the ATLAS detector using data collected in 2015 at $\sqrt{s} = 13$ TeV*. Tech. rep. ATL-PHYS-PUB-2016-015. Geneva: CERN, 2016. URL: https://cds.cern.ch/record/2203514.

[87] ATLAS Collaboration. "Muon reconstruction performance of the ATLAS detector in proton–proton collision data at $\sqrt{s}$ =13 TeV". In: *Eur.Phys.J.* C76 (2016), p. 292. DOI: 10.1140/EPJC/S10052-016-4120-Y.

[88] ATLAS Collaboration. *Search for dijet resonances in events with an isolated lepton using $\sqrt{s} = 13\,\text{TeV}$ proton–proton collision data collected by the ATLAS detector*. Tech. rep. ATLAS-CONF-2018-015. Geneva: CERN, 2018. URL: http://cds.cern.ch/record/2621126.

[89] ATLAS Collaboration. "Topological cell clustering in the ATLAS calorimeters and its performance in LHC Run 1". In: *Eur.Phys.J.* C77 (2016), p. 490. DOI: 10.1140/EPJC/S10052-017-5004-5.

[90] Matteo Cacciari, Gavin P. Salam, and Gregory Soyez. "The anti-k_t jet clustering algorithm". In: *Journal of High Energy Physics* 2008.04 (2008), pp. 063–063. ISSN: 1029-8479. DOI: 10.1088/1126-6708/2008/04/063. arXiv: 0802.1189.

[91] Matteo Cacciari, Gavin P. Salam, and Gregory Soyez. "FastJet user manual". In: *The European Physical Journal C* 72.3 (2012), p. 1896. ISSN: 1434-6044. DOI: 10.1140/epjc/s10052-012-1896-2.

[92] ATLAS Collaboration. "Jet energy scale measurements and their systematic uncertainties in proton-proton collisions at $\sqrt{s} = 13$ TeV with the ATLAS detector". In: *Phys.Rev.* D96 (2017), p. 072002. DOI: 10.1103/PHYSREVD.96.072002.

[93] ATLAS Collaboration. "Performance of pile-up mitigation techniques for jets in pp collisions at $\sqrt{s} = 8$ TeV using the ATLAS detector". In: *Eur.Phys.J.* C76 (2015), p. 581. DOI: 10.1140/EPJC/S10052-016-4395-Z.

[94] ATLAS Collaboration. "Measurements of b-jet tagging efficiency with the ATLAS detector using $t\bar{t}$ events at $\sqrt{s} = 13$ TeV". In: *JHEP* 1808 (2018), p. 089. DOI: 10.1007/JHEP08(2018)089. arXiv: 1805.01845.

[95] ATLAS Collaboration. "Performance of missing transverse momentum reconstruction with the ATLAS detector using proton-proton collisions at $\sqrt{s} = 13\,\text{TeV}$". In: *Eur.Phys.J.* C78 (2018), p. 903. DOI: 10.1140/EPJC/S10052-018-6288-9.

[96] The ATLAS Collaboration. *Reconstruction, Energy Calibration, and Identification of Hadronically Decaying Tau Leptons in the ATLAS Experiment for Run-2 of the LHC*. Tech. rep. ATL-PHYS-PUB-2015-045. Geneva: CERN, 2015. URL: https://cds.cern.ch/record/2064383.

[97] ATLAS Collaboration. "Reconstruction of hadronic decay products of tau leptons with the ATLAS experiment". In: *Eur. Phys. J.* C76.5 (2016), p. 295. DOI: 10.1140/epjc/s10052-016-4110-0. arXiv: 1512.05955 [hep-ex].

[98] ATLAS Collaboration. *Measurement of the tau lepton reconstruction and identification performance in the ATLAS experiment using pp collisions at* $\sqrt{s} = 13\,\text{TeV}$. Tech. rep. ATLAS-CONF-2017-029. Geneva: CERN, 2017. URL: https://cds.cern.ch/record/2261772.

[99] ATLAS Collaboration. *Selection of jets produced in 13TeV proton-proton collisions with the ATLAS detector*. Tech. rep. ATLAS-CONF-2015-029. Geneva: CERN, 2015. URL: https://cds.cern.ch/record/2037702.

[100] R.K. Ellis et al. "Higgs decay to $\tau^+\tau^-$; A possible signature of intermediate mass Higgs bosons at high energy hadron colliders". In: *Nuclear Physics B* 297.2 (1988), pp. 221–243. ISSN: 0550-3213. DOI: 10.1016/0550-3213(88)90019-3.

[101] A. Elagin et al. "A New Mass Reconstruction Technique for Resonances Decaying to di-tau". In: *Nuclear Instruments and Methods in Physics Research Section A: Accelerators, Spectrometers, Detectors and Associated Equipment* 654.1 (2010), pp. 481–489. ISSN: 01689002. DOI: 10.1016/j.nima.2011.07.009. arXiv: 1012.4686.

[102] The ATLAS Collaboration. *Cross-section measurements of the Higgs boson decaying to a pair of tau leptons in proton–proton collisions at* $\sqrt{s} = 13$ *TeV with the ATLAS detector*. Tech. rep. ATLAS-CONF-2018-021. Geneva: CERN, 2018. URL: http://cds.cern.ch/record/2621794.

[103] The ATLAS Collaboration. "Test of CP invariance in vector-boson fusion production of the Higgs boson using the Optimal Observable method in the ditau decay channel with the ATLAS detector". In: *The European Physical Journal C* 76.12 (2016), p. 658. ISSN: 1434-6052. DOI: 10.1140/epjc/s10052-016-4499-5.

[104] Paolo Nason. "A New method for combining NLO QCD with shower Monte Carlo algorithms". In: *JHEP* 11 (2004), p. 40. DOI: 10.1088/1126-6708/2004/11/040. arXiv: 0409146 [hep-ph].

[105] John M. Campbell et al. "W and Z bosons in association with two jets using the POWHEG method". In: *Journal of High Energy Physics* 2013.8 (2013), p. 5. ISSN: 1029-8479. DOI: 10.1007/JHEP08(2013)005.

[106] Hung-Liang Lai et al. "New parton distributions for collider physics". In: *Physical Review D* 82.7 (2010), p. 074024. ISSN: 1550-7998. DOI: 10.1103/PhysRevD.82.074024.

[107] Torbjörn Sjöstrand, Stephen Mrenna, and Peter Skands. "PYTHIA 6.4 physics and manual". In: *Journal of High Energy Physics* 2006.05 (2006), pp. 026–026. ISSN: 1029-8479. DOI: 10.1088/1126-6708/2006/05/026.

[108] Torbjörn Sjöstrand, Stephen Mrenna, and Peter Skands. "A Brief Introduction to PYTHIA 8.1". In: *Computer Physics Communications* 178.11 (2007), pp. 852–867. ISSN: 00104655. DOI: 10.1016/j.cpc.2008.01.036. arXiv: 0710.3820.

[109] The ATLAS Collaboration. "Measurement of the Z/γ^* boson transverse momentum distribution in pp collisions at $\sqrt{s} = 7$ TeV with the ATLAS detector". In: *JHEP* 1409 (2014), p. 145. DOI: 10.1007/JHEP09(2014)145.

[110] Jonathan Pumplin et al. "New Generation of Parton Distributions with Uncertainties from Global QCD Analysis". In: *Journal of High Energy Physics* 2002.07 (2002), pp. 012–012. ISSN: 1029-8479. DOI: 10.1088/1126-6708/2002/07/012.

[111] N. Davidson, T. Przedzinski, and Z. Was. "PHOTOS interface in C++". In: *Computer Physics Communications* 199 (2016), pp. 86–101. ISSN: 00104655. DOI: 10.1016/j.cpc.2015.09.013.

[112] J. Butterworth et al. "Les Houches 2013: Physics at TeV Colliders: Standard Model Working Group Report". In: (2014). arXiv: 1405.1067.

[113] Charalampos Anastasiou et al. "High-precision QCD at hadron colliders: Electroweak gauge boson rapidity distributions at next-to-next-to leading order". In: *Physical Review D* 69.9 (2004), p. 094008. ISSN: 1550-7998. DOI: 10.1103/PhysRevD.69.094008.

[114] Jun Gao et al. "The CT10 NNLO Global Analysis of QCD". In: *Physical Review D* 89.3 (2013), p. 033009. ISSN: 1550-7998. DOI: 10.1103/PhysRevD.89.033009. arXiv: 1302.6246.

[115] Sergey G. Bondarenko and Andrey A. Sapronov. "NLO EW and QCD proton-proton cross section calculations with mcsanc-v1.01". In: *Computer Physics Communications* 184.10 (2013), pp. 2343–2350. ISSN: 00104655. DOI: 10.1016/j.cpc.2013.05.010. arXiv: 1301.3687.

[116] Simone Alioli, Sven-Olaf Moch, and Peter Uwer. "Hadronic top-quark pair-production with one jet and parton showering". In: *Journal of High Energy Physics* 2012.1 (2011), p. 137. ISSN: 1029-8479. DOI: 10.1007/JHEP01(2012)137. arXiv: 1110.5251.

[117] Simone Alioli et al. "NLO single-top production matched with shower in POWHEG: s- and t-channel contributions". In: *JHEP* 09 (2009), p. 111. DOI: 10.1007/JHEP02(2010)011. arXiv: 0907.4076 [hep-ph].

[118] Emanuele Re. "Single-top Wt-channel production matched with parton showers using the POWHEG method". In: *Eur. Phys. J.* C71 (2011), p. 1547. DOI: 10.1140/epjc/s10052-011-1547-z. arXiv: 1009.2450 [hep-ph].

[119] Pierre Artoisenet et al. "Automatic spin-entangled decays of heavy resonances in Monte Carlo simulations". In: *Journal of High Energy Physics* 2013.3 (2013), p. 15. ISSN: 1029-8479. DOI: 10.1007/JHEP03(2013)015.

[120] Peter Zeiler Skands. "Tuning Monte Carlo Generators: The Perugia Tunes". In: *Physical Review D* 82.7 (2010), p. 074018. ISSN: 1550-7998. DOI: 10.1103/PhysRevD.82.074018. arXiv: 1005.3457.

[121] Michal Czakon and Alexander Mitov. "Top++: a program for the calculation of the top-pair cross-section at hadron colliders". In: *Computer Physics Communications* 185.11 (2011), pp. 2930–2938. ISSN: 00104655. DOI: 10.1016/j.cpc.2014.06.021. arXiv: 1112.5675.

[122] Nikolaos Kidonakis. "Two-loop soft anomalous dimensions for single top quark associated production with a W- or H-". In: *Physical Review D* 82.5 (2010), p. 054018. ISSN: 1550-7998. DOI: 10.1103/PhysRevD.82.054018. arXiv: 1005.4451.

[123] P. Kant et al. "HATHOR for single top-quark production: Updated predictions and uncertainty estimates for single top-quark production in hadronic collisions". In: *Computer Physics Communications* 191 (2014), pp. 74–89. ISSN: 00104655. DOI: 10.1016/j.cpc.2015.02.001. arXiv: 1406.4403.

[124] T. Gleisberg et al. "Event generation with SHERPA 1.1". In: *Journal of High Energy Physics* 2009.02 (2008), pp. 007–007. ISSN: 1029-8479. DOI: 10.1088/1126-6708/2009/02/007. arXiv: 0811.4622.

[125] Tanju Gleisberg and Stefan Hoeche. "Comix, a new matrix element generator". In: *Journal of High Energy Physics* 2008.12 (2008), pp. 039–039. ISSN: 1029-8479. DOI: 10.1088/1126-6708/2008/12/039. arXiv: 0808.3674.

[126] Fabio Cascioli, Philipp Maierhöfer, and Stefano Pozzorini. "Scattering Amplitudes with Open Loops". In: *Physical Review Letters* 108.11 (2011), p. 111601. ISSN: 0031-9007. DOI: 10.1103/PhysRevLett.108.111601. arXiv: 1111.5206.

[127] Steffen Schumann and Frank Krauss. "A parton shower algorithm based on Catani-Seymour dipole factorisation". In: *Journal of High Energy Physics* 2008.03 (2007), pp. 038–038. ISSN: 1029-8479. DOI: 10.1088/1126-6708/2008/03/038. arXiv: 0709.1027.

[128] Stefan Hoeche et al. "QCD matrix elements + parton showers: The NLO case". In: *Journal of High Energy Physics* 2013.4 (2012), p. 27. ISSN: 1029-8479. DOI: 10.1007/JHEP04(2013)027. arXiv: 1207.5030.

[129] Richard D. The NNPDF Collaboration et al. "Parton distributions for the LHC Run II". In: *Journal of High Energy Physics* 2015.4 (2014), p. 40. ISSN: 1029-8479. DOI: 10.1007/JHEP04(2015)040. arXiv: 1410.8849.

[130] Ryan Gavin et al. "FEWZ 2.0: A code for hadronic Z production at next-to-next-to-leading order". In: *Computer Physics Communications* 182.11 (2010), pp. 2388–2403. ISSN: 00104655. DOI: 10.1016/j.cpc.2011.06.008. arXiv: 1011.3540.

[131] David J. Lange. "The EvtGen particle decay simulation package". In: *Nuclear Instruments and Methods in Physics Research Section A: Accelerators, Spectrometers, Detectors and Associated Equipment* 462.1-2 (2001), pp. 152–155. ISSN: 0168-9002. DOI: 10.1016/S0168-9002(01)00089-4.

[132] ATLAS Collaboration. *Summary of ATLAS Pythia 8 tunes*. Tech. rep. ATL-PHYS-PUB-2012-003. Geneva: CERN, 2012. URL: https://cds.cern.ch/record/1474107.

[133] A. D. Martin et al. "Parton distributions for the LHC". In: *The European Physical Journal C* 63.2 (2009), pp. 189–285. ISSN: 1434-6044. DOI: 10.1140/epjc/s10052-009-1072-5. arXiv: 0901.0002.

[134] S. et al. Agostinelli. "Geant4—a simulation toolkit". In: *Nuclear Instruments and Methods in Physics Research Section A: Accelerators, Spectrometers, Detectors and Associated Equipment* 506.3 (2003), pp. 250–303. ISSN: 0168-9002. DOI: 10.1016/S0168-9002(03)01368-8.

[135] ATLAS Collaboration. "The ATLAS Simulation Infrastructure". In: *The European Physical Journal C* 70.3 (2010), pp. 823–874. ISSN: 1434-6044. DOI: 10.1140/epjc/s10052-010-1429-9. arXiv: 1005.4568.

[136] E Bagnaschi et al. "Higgs production via gluon fusion in the POWHEG approach in the SM and in the MSSM". In: *JHEP* 02 (2012), p. 88. DOI: 10.1007/JHEP02(2012)088. arXiv: 1111.2854 [hep-ph].

[137] J Alwall et al. “The automated computation of tree-level and next-to-leading order differential cross sections, and their matching to parton shower simulations”. In: *JHEP* 07 (2014), p. 79. DOI: 10.1007/JHEP07(2014)079. arXiv: 1405.0301 [hep-ph].

[138] M Wiesemann et al. “Higgs production in association with bottom quarks”. In: *JHEP* 02 (2015), p. 132. DOI: 10.1007/JHEP02(2015)132. arXiv: 1409.5301 [hep-ph].

[139] Sayipjamal Dulat et al. “New parton distribution functions from a global analysis of quantum chromodynamics”. In: *Physical Review D* 93.3 (2016), p. 033006. ISSN: 2470-0010. DOI: 10.1103/PhysRevD.93.033006.

[140] Torbjörn Sjöstrand et al. “An introduction to PYTHIA 8.2”. In: *Computer Physics Communications* 191 (2015), pp. 159–177. ISSN: 00104655. DOI: 10.1016/j.cpc.2015.01.024.

[141] The ATLAS Collaboration. *ATLAS Run 1 Pythia8 tunes*. Tech. rep. ATL-PHYS-PUB-2014-021. Geneva: CERN, 2014. URL: https://cds.cern.ch/record/1966419.

[142] Richard D. Ball et al. “Parton distributions with LHC data”. In: *Nuclear Physics B* 867.2 (2013), pp. 244–289. ISSN: 05503213. DOI: 10.1016/j.nuclphysb.2012.10.003.

[143] LHC Higgs Cross Section Working Group. “Handbook of LHC Higgs Cross Sections: 4. Deciphering the Nature of the Higgs Sector”. In: (2016). DOI: 10.23731/CYRM-2017-002.

[144] Robert V. Harlander, Stefan Liebler, and Hendrik Mantler. “SusHi: A program for the calculation of Higgs production in gluon fusion and bottom-quark annihilation in the Standard Model and the MSSM”. In: *Computer Physics Communications* 184.6 (2013), pp. 1605–1617. ISSN: 00104655. DOI: 10.1016/j.cpc.2013.02.006.

[145] Robert V Harlander and Matthias Steinhauser. “Supersymmetric Higgs production in gluon fusion at next-to-leading order”. In: *Journal of High Energy Physics* 2004.09 (2004), pp. 066–066. ISSN: 1029-8479. DOI: 10.1088/1126-6708/2004/09/066.

[146] G. Degrassi, S. Di Vita, and P. Slavich. "On the NLO QCD corrections to the production of the heaviest neutral Higgs scalar in the MSSM". In: *The European Physical Journal C* 72.6 (2012), p. 2032. ISSN: 1434-6044. DOI: 10.1140/epjc/s10052-012-2032-z.

[147] Robert V. Harlander and William B. Kilgore. "Next-to-Next-to-Leading Order Higgs Production at Hadron Colliders". In: *Physical Review Letters* 88.20 (2002), p. 201801. ISSN: 0031-9007. DOI: 10.1103/PhysRevLett.88.201801.

[148] Charalampos Anastasiou and Kirill Melnikov. "Pseudoscalar Higgs boson production at hadron colliders in next-to-next-to-leading order QCD". In: *Physical Review D* 67.3 (2003), p. 037501. ISSN: 0556-2821. DOI: 10.1103/PhysRevD.67.037501.

[149] U. Aglietti et al. "Two-loop light fermion contribution to Higgs production and decays". In: *Physics Letters B* 595.1-4 (2004), pp. 432–441. ISSN: 03702693. DOI: 10.1016/j.physletb.2004.06.063.

[150] Robert V. Harlander and William B. Kilgore. "Higgs boson production in bottom quark fusion at next-to-next-to-leading order". In: *Physical Review D* 68.1 (2003), p. 013001. ISSN: 0556-2821. DOI: 10.1103/PhysRevD.68.013001.

[151] Stefan Dittmaier, Michael Krämer, and Michael Spira. "Higgs radiation off bottom quarks at the Fermilab Tevatron and the CERN LHC". In: *Physical Review D* 70.7 (2004), p. 074010. ISSN: 1550-7998. DOI: 10.1103/PhysRevD.70.074010.

[152] S. Dawson et al. "Exclusive Higgs boson production with bottom quarks at hadron colliders". In: *Physical Review D* 69.7 (2004), p. 074027. ISSN: 1550-7998. DOI: 10.1103/PhysRevD.69.074027.

[153] Robert Harlander, Michael Krämer, and Markus Schumacher. "Bottom-quark associated Higgs-boson production: reconciling the four- and five-flavour scheme approach". In: (2011). arXiv: 1112.3478.

[154] S Heinemeyer, W Hollik, and G Weiglein. "FeynHiggs: a program for the calculation of the masses of the neutral CP-even Higgs bosons in the MSSM". In: *Comput. Phys. Commun.* 124 (2000), pp. 76–89. DOI: 10.1016/S0010-4655(99)00364-1. arXiv: 9812320 [hep-ph].

[155] A Djouadi, J Kalinowski, and M Spira. "HDECAY: A Program for Higgs boson decays in the standard model and its supersymmetric extension". In: *Comput.Phys.Commun.* 108 (1998), pp. 56–74. DOI: 10.1016/S0010-4655(97)00123-9. arXiv: hep-ph/9704448 [hep-ph].

[156] A Djouadi, M M Muhlleitner, and M Spira. "Decays of supersymmetric particles: The Program SUSY-HIT (SUspect-SdecaY-Hdecay-InTerface)". In: *Acta Phys. Polon.* B38 (2007), pp. 635–644. arXiv: hep-ph/0609292 [hep-ph].

[157] A. Bredenstein et al. "Precise predictions for the Higgs-boson decay $H \to WW/ZZ \to$4 leptons". In: *Physical Review D* 74.1 (2006), p. 013004. ISSN: 1550-7998. DOI: 10.1103/PhysRevD.74.013004.

[158] Axel Bredenstein et al. "Radiative corrections to the semileptonic and hadronic Higgs-boson decays $H \to WW/ZZ \to$4 fermions". In: *Journal of High Energy Physics* 2007.02 (2007), pp. 080–080. ISSN: 1029-8479. DOI: 10.1088/1126-6708/2007/02/080.

[159] Glen Cowan et al. "Asymptotic formulae for likelihood-based tests of new physics". In: *The European Physical Journal C* 71.2 (2010), pp. 1–19. ISSN: 1434-6044. DOI: 10.1140/epjc/s10052-011-1554-0. arXiv: 1007.1727.

[160] M. Bahr et al. "Herwig++ Physics and Manual". In: *The European Physical Journal C* 58.4 (2008), pp. 639–707. ISSN: 1434-6044. DOI: 10.1140/epjc/s10052-008-0798-9. arXiv: 0803.0883.

[161] ATLAS Collaboration. "Search for high-mass new phenomena in the dilepton final state using proton-proton collisions at $\sqrt{s} = 13$ TeV with the ATLAS detector". In: *Phys.Lett.* B761 (2016), pp. 372–392. DOI: 10.1016/J.PHYSLETB.2016.08.055.

[162] Kyle Cranmer et al. *HistFactory: A tool for creating statistical models for use with RooFit and RooStats*. Tech. rep. CERN-OPEN-2012-016. New York: New York U., 2012. URL: https://cds.cern.ch/record/1456844.

[163] A L Read. "Presentation of search results: the CL s technique". In: *Journal of Physics G: Nuclear and Particle Physics* 28.10 (2002), pp. 2693–2704. ISSN: 0954-3899. DOI: 10.1088/0954-3899/28/10/313.